SHAPE MEMORY BEHAVIOR OF ULTRAFINE GRAINED NiTi

AND TiNiPd SHAPE MEMORY ALLOYS

A Dissertation

by

BENAT KOCKAR

Submitted to the Office of Graduate Studies of
Texas A&M University
in partial fulfillment of the requirements for the degree of

DOCTOR OF PHILOSOPHY

December 2007

Major Subject: Mechanical Engineering

SHAPE MEMORY BEHAVIOR OF ULTRAFINE GRAINED NiTi

AND TiNiPd SHAPE MEMORY ALLOYS

A Dissertation

by

BENAT KOCKAR

Submitted to the Office of Graduate Studies of
Texas A&M University
in partial fulfillment of the requirements for the degree of

DOCTOR OF PHILOSOPHY

Approved by:

Chair of Committee,	Ibrahim Karaman
Committee Members,	Dimitris C. Lagoudas
	K. Ted Hartwig
	Richard Griffin
Head of Department,	Dennis L. O'Neal

December 2007

Major Subject: Mechanical Engineering

ABSTRACT

Shape Memory Behavior of Ultrafine Grained NiTi and TiNiPd
Shape Memory Alloys.
(December 2007)
Benat Kockar, B.S., Middle East Technical University;
M.S., Middle East Technical University
Chair of Advisory Committee: Dr. Ibrahim Karaman

The cyclic instability in shape memory characteristics of NiTi-based shape memory alloys (SMAs), such as transformation temperatures, transformation and irrecoverable strains and transformation hysteresis upon thermal and mechanical cycling limits their applications requiring high number of cycles. The main reasons for these instabilities are lattice incompatibility between transforming phases and relatively low lattice resistance against dislocation motion. The objective of this study is to increase the slip resistance and thus, to minimize the plastic accommodation upon phase transformation in NiTi and TiNiPd SMAs. The effects of grain refinement down to submicron to nanorange through Equal Channel Angular Extrusion (ECAE) on the cyclic stability were investigated as potential remedies. The influence of ECAE parameters, such as processing temperature and strain path on the microstructural refinement was explored as well as the corresponding evolution in the stress differential between the yield strength of martensite and the critical stress to induce martensite and SMA characteristics of $Ni_{49.7}Ti_{50.3}$, $Ti_{50}Ni_{30}Pd_{20}$, and $Ti_{50.3}Ni_{33.7}Pd_{16}$ SMAs.

Severe plastic deformation via ECAE at temperatures from 300°C up to 450°C refined the grains from 50μm down to a range between 0.03μm and 0.3μm in $Ni_{49.7}Ti_{50.3}$ and 0.5μm and 1μm in TiNiPd alloys. Regardless of the material, the lower the ECAE temperature and the higher the ECAE strain path, the better the cyclic stability. ECAE led to an increase in the stress differential between the yield strength of martensite and critical stress to induce martensite due to observed microstructural refinement and this

increase is responsible for the improvement in the cyclic stability of the aforementioned SMA characteristics in all investigated materials. Addition of Pd to the NiTi alloy reduced the thermal hysteresis from 36°C down to 11°C, and enhanced the cyclic stability of the SMA characteristics. In additions to positive influence of ECAE on cyclic stability, it also led to an increase in the fracture stress levels of the TiNiPd alloys due to the fragmentation or dissolution of the precipitates responsible for the premature failures. ECAE caused a slight reduction in the work output; however it was possible to obtain large stable work outputs under higher stress levels than unprocessed materials.

TO

MY MOTHER-NIHAL BILCEN, MY AUNT-MUHSINE GENC

AND

MY SON-BARKAN E. KOCKAR

ACKNOWLEDGEMENTS

and making me hang in there in my hard times during my studies. My close friends, Diane Pruiett, Dr. Burcu Baris Keskin, Ezgi Can Eren and Arzu Karaer are also thanked for making my stay at Texas A&M University a memorable one and for being a second family in College Station.

I would thank my husband, Dr. Mustafa Kerem Kockar, for his never-ending patience during my stay at Texas A&M University and living apart from him for more than 3 years. It has been a very difficult experience for both of us and for our marriage. I would also thank to my brother Baran Bilcen, his wife Sumru Bilcen and their lovely daughter-my beautiful niece Azra Bilcen for always encouraging me to finish my Ph.D in long distance phone talks. My brother's never-ending drive and ability to always be the best at what he does has never ceased to amaze me.

Last but not least, I am gratefully thankful to my mother and my aunt, Nihal Bilcen and Muhsine Genc, for the unconditional support that they have always given to me. Their strong motivations are the reason for my successes in every part of my life. They always showed the right directions in my life and were able to provide me with the vision that college was important to me- without them I would have never started. Finally, I would like to dedicate this work to my mother, my aunt and my dear son Barkan Efe Kockar. He was sent to me to lighten my life and world. My son will always be my motivation in my dreams that I will continue to follow.

TABLE OF CONTENTS

CHAPTER

LIST OF FIGURES

LIST OF TABLES

CHAPTER I

INTRODUCTION

1.1 Motivation

NiTi alloys which undergo thermoelastic martensitic phase transformation are the most popular shape memory alloys (SMAs) owing to their ability to recover their initial shape after deformation and due to high actuation work outputs per unit volume [1, 2]. In addition to these superior shape memory properties, NiTi alloys are exceptional due to their biocompatibility and good corrosion resistance [3]. Many practical applications of these alloys require a large number of thermo-mechanical cycles, as well as a stable and reliable shape memory effect. However, there are problems frequently reported in the literature associated with cyclic stability of the shape memory effect in NiTi alloys. For instance, Miyazaki et al. [4, 5] and Lexcellent et al. [6] have reported that pseudoelastic hysteresis loops drift down with cycles and settle to a stable loop [7]. In addition, poor cyclic stability during isobaric thermal cycling experiments has been observed [8-10]. It is reported that the martensite start temperature (M_s) decreases and the irrecoverable (plastic) strain levels increase with increasing number of thermal cycles [8-11]. Sehitoglu et al. [12] demonstrated large variations in the temperature hysteresis with external stress under thermal cycling conditions. The main reason for the cyclic instability of the parameters important for shape memory response is the accommodation of the incompatibility between austenite and martensite phases with dislocation formation, in addition to transformation twinning and elastic accommodation, which leads to plastic strain formation, martensite stabilization and variation in transformation temperatures, thermal and stress hysteresis upon thermo-mechanical cycling. Miyazaki et al. [5] showed that during thermo-mechanical cycling, the austenite/martensite interface travels forward and backward, during which deformation induced defects such

---

This dissertation follows the style and format of Acta Materialia.

as dislocations form and these dislocations hinder the austenite/martensite interface movement. The accumulation of microscopic residual stresses and retained martensites eventually influences the macroscopic shape memory behavior of NiTi alloys.

A possible way to tackle the cyclic instability problem is to increase the critical shear stress (CSS) for slip and thus to minimize the plastic accommodation and martensite stabilization upon phase transformation through small precipitation, grain refinement, specific texture formation and strain hardening via introducing dislocation substructures [13]. Hornbogen et al. [14] proposed that the cyclic stability can be improved by increasing the stress differential between the critical stress for stress-induced martensitic transformation and the yield stress of the stress induced martensite. All the aforementioned studies showed that the cyclic response of these alloys depends on the thermo-mechanical history such as ausforming, aging, cold deformation and annealing treatments [5, 15].

There have been many works performed on producing coherent Ti_3Ni_4 precipitates in Ni-rich NiTi alloys which generally improves the cyclic stability of NiTi as compared to other heat treatments such as solutionizing or overaging [15, 16]. However, on the Ni-rich side of TiNi alloys, the transformation temperatures decrease to subzero levels with the increase in Ni-content. Formation of Ti_3Ni_4 precipitates somewhat increases the transformation temperatures due to depletion of Ni in the matrix, yet, the transformation temperatures of the aged Ni-rich TiNi are still below room temperature and depend on the amount and size of the precipitates. Superelasticity is available in the aged Ni-rich alloys in a narrow temperature range and the shape memory effect is observed with some permanent strain [15].

Single crystal studies on TiNi alloys showed that the transformation behavior highly depends on crystallographic orientation. For instance, the [111] orientation shows poor cyclic degradation resistance and rapid increase in permanent strain with cycles [15]. In addition, the [111] orientation demonstrates a large stress hysteresis in pseudoleastic cyclic experiments [15]. On the other hand, in NiTi, the slip systems were reported to be {100}<001> and {110}<001>, therefore, NiTi single crystals with the

loading axis near the [001] pole have superior fatigue response as compared to other orientations because they demonstrate less irreversible slip [17]. The disadvantages of single crystals are high cost, difficulty of mass production and fabricating different forms such as wires and plates. In the light of these studies on the orientation dependence of shape memory properties in NiTi alloys, crystallographic texture is one of the important parameters that determines the shape memory response of polycrystalline NiTi alloys.

Conventional deformation techniques such as cold rolling, drawing and extrusion can impart large strains to materials. However, one or more dimensions of the material are reduced. It is reported that cold deformation without annealing usually suppresses phase transformation to very low temperatures [18]. Therefore, annealing below the recrystallization temperature is needed to increase the transformation temperatures and rearrange the tangled dislocations to observe a smooth martensitic transformation upon heating and cooling. Cold drawn polycrystalline NiTi alloys have a strong texture of [111] type at which the cyclic degradation is mostly expected [19]. Miyazaki et al. [18] has found that annealing cold worked NiTi alloy at 673K establishes cyclic stability; however, it is reported that plastic strain accumulation with cyclic deformation is still an important issue in cold worked NiTi alloys under high stress levels [9].

Recently, the effect of ausforming on the martensitic transformation of equiatomic NiTi alloys was investigated extensively [15, 20]. Ausforming is a technique in which the dislocations are introduced into austenite phase. Severe plastic deformation (SPD) via ausforming might be advantageous in achieving the stable cyclic stability. Dislocation density increases and grain size decreases down to nano range using SPD techniques such as high pressure torsion (HPT) and equal channel angular extrusion (ECAE). HPT leads to amorphization and nanograin formation after subsequent annealing. The sample size that can be obtained from HPT is very small such that extensive investigation on the sample is not possible. In addition, the strain is not uniform throughout the sample in HPT. On the other hand, ECAE permits the application of large uniform strain without reduction in the cross-section of the work

piece [21]. ECAE offers several advantages over other competing processes such as HPT and conventional area-reduction extrusion, including larger sample sizes, and some control on grain morphology and crystallographic texture [22]. Therefore, ECAE is selected as the SPD process of choice in this study.

Most SMAs are intermetallics and suffer from low ductility due to the lack of sufficient slip systems [23]. Although NiTi alloys exhibit relatively better ductility than many intermetallic alloys due to mechanical twinning as an additional deformation mechanism both in martensite and austenite, SPD via ECAE of NiTi based SMAs is challenging because they have high flow strength in austenite. The ECAE tool to be used during processing should be able to handle high stress levels, and the friction between the work piece and the walls should be as low as possible.

Only a limited number of studies have been undertaken on the severe plastically deformed NiTi alloys because of the difficulty in processing. Waitz et al. [24-26] focused on the stabilization of austenite with the decrease in grain size to nano range after HPT. He also investigated twinning mechanisms in martensite as a function of grain size [24-26]. Valiev and his colleagues [27-29] demonstrated the effect of SPD via HPT and ECAE on the microstructural evolution and conventional mechanical properties such as strength and ductility but did not report any extensive shape memory properties such as transformation and irrecoverable strains and thermal cyclic stability after SPD processes. Therefore, in this study, the affect of ECAE parameters, such as processing temperature, strain magnitude and strain path, on the microstructural refinement and dislocation substructure formation were investigated, as well as the corresponding evolution in the shape memory, of monotonic and thermo-mechanical response for near equiatomic NiTi SMAs.

For the applications beyond 100°C, there is a strong need to develop new alloys other than NiTi. The addition of ternary elements such as Au, Pd, Pt, Hf and Zr was shown to increase the transformation temperatures above 100°C [30, 31]. High-temperature SMA compositions in the NiTiPd and NiTiPt systems have attracted great interest for use in compact solid-state actuators for the aerospace, automotive, and power

generation industries [32]. Zr and Hf could be more favorable because of their relatively low cost, however, thermal and stress hysteresis of these alloys is large [13, 33]. Moreover, transformation-induced plasticity and creep have limited the level and stability of the shape memory effect and superelasticity in these ternary alloys more than that in binary NiTi [13]. On the other hand, NiTiPd and NiTiPt SMAs have very small thermal hysteresis and high transformation temperatures depending on their compositions [32, 34].

Martensitic transformation in NiTiPd and NiTiPt SMAs was first reported by Donkersloot and Van Vucht [35]. The addititon of more than 10at.% Pd or Pt to the NiTi system with substitution Ni increases the transformation temperature to above 100°C [36]. The disadvantage of these ternary alloys is their brittleness due to intrinsic low ductility and oxygen stabilized precipitates. Additionally, Cai et.al [37] reported that the shape memory behavior of TiNiPd alloys is fairly good at room temperature however becoming poor with increasing temperature due to the decrease in the critical shear stress for slip. To date, much of the published work is on the shape memory effect of these alloys under stress free conditions [38-40]. Golberg et al. [41] studied the effect of cold rolling and post annealing on the shape memory behavior of $Ti_{50}Ni_{30}Pd_{20}$ alloy. They were able to achieve 100% recovery up to a given strain of 5.3% in tensile experiments at 443K in cold rolled and annealed $Ti_{50}Ni_{30}Pd_{20}$ alloy. However, they did not study the thermal cyclic behavior of the alloy after cold deformation. Noebe and his co-workers have recently investigated the shape memory characteristics of hot extruded TiNiPd alloys with different compositions [32, 34]. They have reported the results of actuator-type constant-load thermal cycling tests (load-biased tests). The results showed that permanent deformation occurs at every stress level and increases with the stress level [32, 34]. They also investigated the work output of the TiNiPd alloys which is another important parameter in actuation type applications. It was found that the work capability of the TiNiPd alloys diminishes due to the permanent deformations occuring during thermal cycling [34].

To date, there is no published study on the severe plastic deformation of TiNiPd

alloys. It is expected that grain refinement and the introduction of dislocations using SPD via ECAE should improve the shape memory properties, work capability and thermal cyclic stability of the TiNiPd alloys. For instance, ECAE might lead to a decrease in the permanent deformations determined at even low stress levels in the aforementioned studies upon grain refinement and dislocation substructure formation. $Ti_{50}Ni_{30}Pd_{20}$ and $Ti_{50.3}Ni_{33.7}Pd_{16}$ are chosen due to their transformation temperatures. The temperature range for the target application which is the actuator part in reconfigurable airplane rotor blades is 100-150°C.

1.2 Objectives

In the light of this motivation, the present study focused on the ECAE of equiatomic NiTi, and $Ti_{50}Ni_{30}Pd_{20}$ and $Ti_{50.3}Ni_{33.7}Pd_{16}$ high temperature shape memory alloys. The equiatomic NiTi alloy was chosen due to its high transformation temperature as compared to other NiTi compositions [42]. In addition, there is no expectation to have second phase precipitation in this composition which should allow investigating only the SPD effect on microstucture, conventional mechanical properties and shape memory behavior of the alloy. The initial part of the study on the equiatomic NiTi alloy also provides a base line for the investigation of TiNiPd high temperature shape memory alloys. For instance, the lowest possible ECAE temperature that TiNiPd alloys can be deformed, or types of experiments to evaluate the shape memory response of TiNiPd alloys, are important beginning steps to start an investigation.

The overall objectives of this research with specific details are to:

1.   Determine the uniform formability limits (i.e. temperature and strain rate) of the equiatomic NiTi, $Ti_{50}Ni_{30}Pd_{20}$ and $Ti_{50.3}Ni_{33.7}Pd_{16}$ alloys. The purity level of the materials is an important factor which dictates the ease of the deformation processing and the lowest possible ECAE temperature.

2.   Identify better ECAE routes and ECAE temperatures for obtaining the most microstructural refinement in the presence of recovery-recrystallization tendencies.

3.   Identify the affects of ECAE on the microstructural evolution of the alloys such as on possible twinning modes in refined grains, dislocation substructures, precipitate size and morphology.

4.   Characterize the mechanical properties such as critical stress to induce martensite and yield strength of stress induced martensite of the unprocessed and ECAE processed materials. The purpose of this characterization is to identify the increase in critical shear stress for slip due to microstructural evolution such as grain refinement, dislocation density increase and the change in precipitate size and morphology upon ECAE.

5.   Determine the affect of the microstructural evolution on certain shape memory characteristics including transformation temperature, transformation and irrecoverable strain levels, and thermal hysteresis.

6.   Identify the mechanisms responsible for brittleness of TiNiPd ternary alloys.

7.   Characterize the influences of microstructural refinement on thermal cyclic stability of the alloys. The purpose of this investigation is to determine the transformation temperature and thermal hysteresis stability and transformation and irrecoverable strain evolution with the number of thermal cycles under constant stress levels.

8.   Develop a thermodynamical framework to understand irreversible and elastic energy contributions which trigger the phase transformation in the unprocessed and ECAE processed equiatomic NiTi alloys. The purpose of this thermodynamical approach is to understand why the irreversible and elastic energy change with microstructural refinement/evolution and the effect of this change on the shape memory characteristics.

To accomplish these objectives, a well planned/executed experimental study was undertaken to demonstrate that ECAE processing can be a viable method to improve the shape memory response of equiatomic NiTi and TiNiPd alloys.

CHAPTER II

THEORETICAL BACKGROUND

2.1 Martensitic Transformations

Since shape memory effect is related to thermoelastic martensitic transformations (MT), the basic information about MT is introduced in this section in a simplified manner before going into details about shape memory effect. The martensitic transformation is a diffusionless, military type phase transformation in solids, in which atoms move by a shear-like mechanism [1]. The transformation is schematically described in Figure 2.1. Parent phase or austenite which is the high temperature phase is usually cubic and martensite which is the low temperature phase has a lower symmetry crystal structure. When the temperature is lowered below martensite start (M_s) temperature, MT starts by a shear like mechanism. When temperature is raised martensite becomes unstable, reverse transformation begins, and martensite transforms back to parent phase with the same orientation if the transformation is crystallographically reversible.
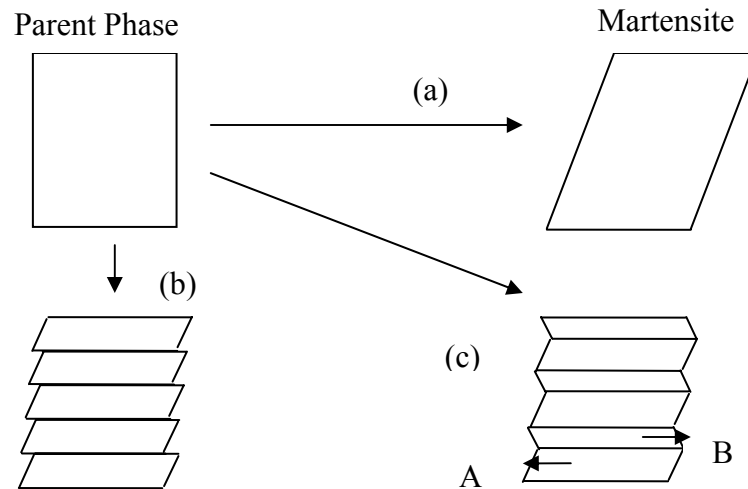
Figure 2.1 a) Shape change upon phase transformation b) represents the accommodation of external strain by slip, c) represents the accommodation of external strain by twin [44].

MT is associated with a shape change as shown in Figure 2.1.a; hence, a large strain occurs around the martensite phase within the parent phase. There are two ways to decrease the large strain around martensite; either by introducing slip as in Figure 2.1.b or by introducing twinning as in Figure 2.1.c. These are called lattice invariant shears because neither slip nor twinning changes the structure of martensite. The introduction of slip or twinning in martensite depends on the alloy system, however, in shape memory alloys the strain relieve mechanism is usually twinning. The martensites in region A and in region B in figure 2.1.c have the same structure; however, their orientations are twin related. These are called correspondence variants. Since martensite phase has lower symmetry than parent phase many variants can be formed from the same parent phase.

Martensitic transformations are not associated with the compositional change, thus the free energy curves of parent and martensite phases can be represented as in Figure 2.2. T_0, G^m and G^p are defined as the thermodynamic equilibrium temperature between two phases, Gibbs free energy of martensite and Gibbs free energy of parent

phase, respectively. $\Delta G^{p\rightarrow m} = G^m - G^p$ represents the driving force for the nucleation of martensite. The Gibbs free energy change of a system upon martensite transformation can be written as [43]:

$$\Delta G = \Delta G_c + \Delta G_{nc} = \Delta G_c + \Delta G_{irr} + \Delta G_e \tag{2.1.1}$$

ΔG_c is the chemical free energy difference between parent phase and martensite, ΔG_{irr} is the irreversible energy term which is associated with the frictional energy required to propagate the transforming interface between parent phase and martensite, and ΔG_e is the elastic energy around the martensite. ΔG_{nc} is the non-chemical energy term which is equal to the sum of elastic energy and irreversible energy terms.

Temperatures where parent phase starts and stops to transform martensite are martensite start (M_s) and martensite finish (M_f) temperatures, respectively, and temperatures where martensite starts and stops to transform back to parent phase is austenite start (A_s) and austenite finish (A_f) temperatures, respectively.
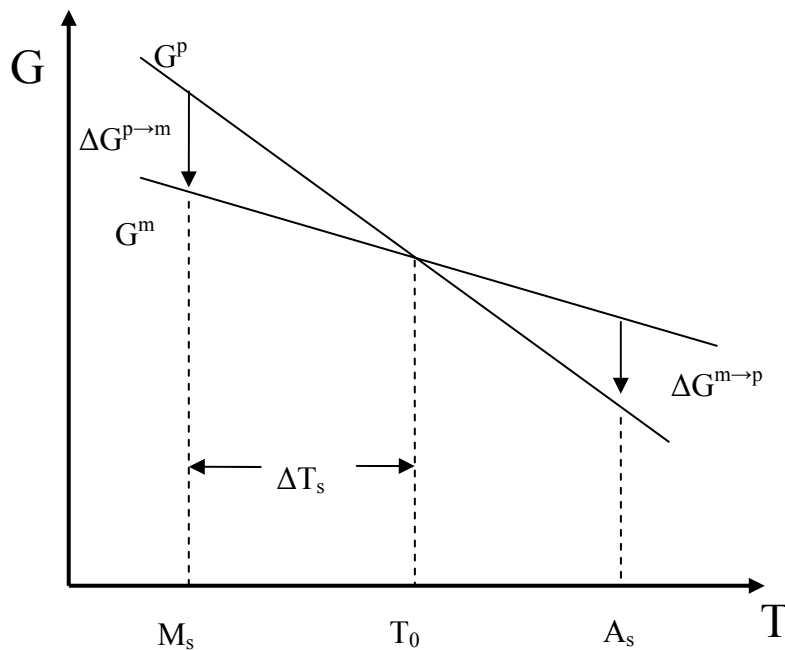
Figure 2.2 Schematic representation of free energy curves of parent and martensite phases, and their relationship to the M_s and A_s [44].

In most martensitic transformations, the non chemical free energy term is non-zero, hence, supercooling of ΔT_s is needed for the nucleation of martensite and superheating is necessary for the back transformation. Because of the elastic energy storage around martensite further undercooling is necessary to overcome the resistance to the growth of martensite.

Martensitic transformations can be classified in two categories, thermoelastic and non-thermoelastic. If the non-chemical energy term is small which means the interface between martensite and austenite is mobile, energy dissipation is low and transformation is crystallographically reversible, then martensite is thermoelastic. On the other hand, if the non-chemical energy term is large which means the interface between martensite and austenite is immobile and energy dissipation is large the reverse transformation occurs by the renucleation of austenite, and then martensite is non-thermoelastic [45]. The difference between thermoelastic and non-thermoelastic martensite is presented in Figure 2.3 in terms of their thermal hysteresis. Shape memory alloys show characteristics of thermoelastic martensitic transformations. The notion "thermoelastic transformations" in SMAs were first introduced by Kurdjumov and Khandros who observed the behavior in Cu-Al-Ni alloys [46]. In Figure 2.3, Au-Cd alloy represents the thermoelastic shape memory alloy.
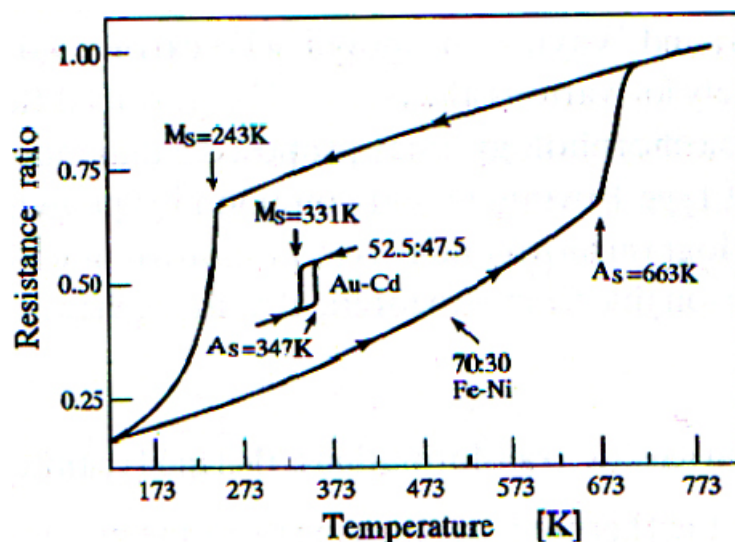
Figure 2.3 Electrical resistivity vs temperature curves for thermoelastic and non-thermoelastic martensite [1].

2.2 Shape Memory Effect

The shape memory effect (SME) is a property which covers two basic requirements; thermoelastic martensitic transformation and twinning as a deformation mode. The defomation processes that are mainly responsible for shape memory effect are deformation of martensite or stress induced martensitic transformation. As discussed in section 2.1, the deformation of martensite should occur by twinning to realize the shape memory effect, because slip is an irreversible process. The martensitic transformation occurs in self accommodating manner to keep the same shape upon cooling (upon transformation) and to minimize the energy change. Further deformation proceeds with twin boundary motion which is the reorientation process of one martensite variant to another. Saburi et al. [47] demonstrated that the most favorable correspondence variant grows at the expense of the others and gives the largest strain under the applied stress. Martensite transform back to austenite upon heating above A_f. When the temperature is below M_f the specimen is in complete martensitic state, thus the deformation is the deformation of martensite, however if the temperature is above M_f a part or whole of the deformation is by stress-induced martensitic transformation. The

superelasticity or transformation pseudoelasticity concept arises from the stress induced martensitic transformations. Superelasticity occurs by the stress induced transformation upon loading and transforms back to austenite upon unloading. The condition of observing superelasticity and shape memory effect in the same specimen depends on the test temperature. The required conditions for each mechanism are demonstrated in Figure 2.4.

The line with positive slope in Figure 2.4 represents the critical stress to induce martensitic transformation and the lines with negative slopes represent the critical stress for slip. The hatched region is the region that if the stress is applied above A_f, the stress induced martensite transformation occurs at a stress above the critical stress for inducing martensite. Upon unloading the martensite transforms back to austenite since martensite is unstable above A_f in the absence of stress. If the stress is applied at temperatures below A_s, martensite stays deformed after unloading and the strain can be recovered only by heating the specimen above A_f. Therefore, in the region between A_s and A_f, both superelasticity and shape memory effect coexist. Deformation at temperatures above M_d do not lead to stress induced transformation since the main mechanism taking place is deformation by slip. Figure 2.5 demonstrates schematic stress-strain response of a shape memory alloy. There are three possible deformation mechanisms which are explained below and represented in Figure 2.5.

1st Case: If the material is in the austenitic phase, in Stage I, elastic deformation of austenite occurs, in Stage II, stress induced martensite forms and in Stage III, slip deformation occurs.

2nd Case: If the material is in the martensitic phase, in Stage I, elastic deformation of martensite occurs, in Stage II, detwinning of martensite proceeds with the growing of some favored variants at the expense of others, in Stage III, slip deformation of martensite occurs.

3rd Case: If the initial material is a mixture of austenite and martensite phases mixture of the 1st and 2nd mechanisms take place.

Upon unloading, the martensite phase unloads elastically in all mechanisms and

pseudoelastic strain would follow the elastic strain (transformation from martensite to austenite) in Case I and III. Further strain can be recovered by heating above A_f, and this behavior is called shape memory effect. The remaining strain is the irrecoverable strain.
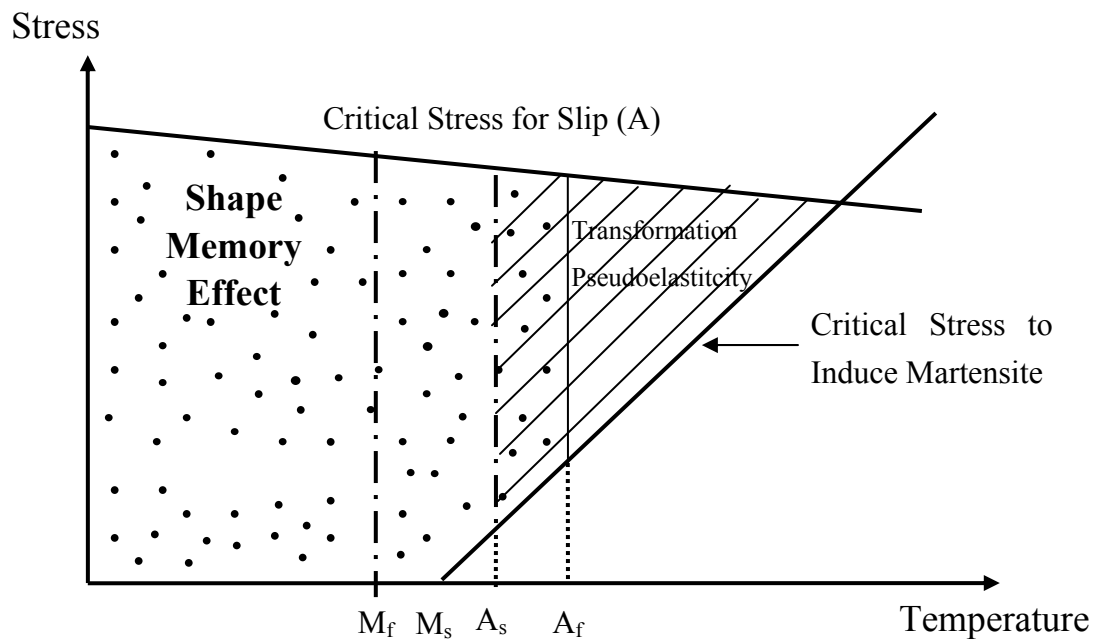
Figure 2.4 Schematic representation for the thermo-mechanical conditions of shape memory effect and superelasticity [44].
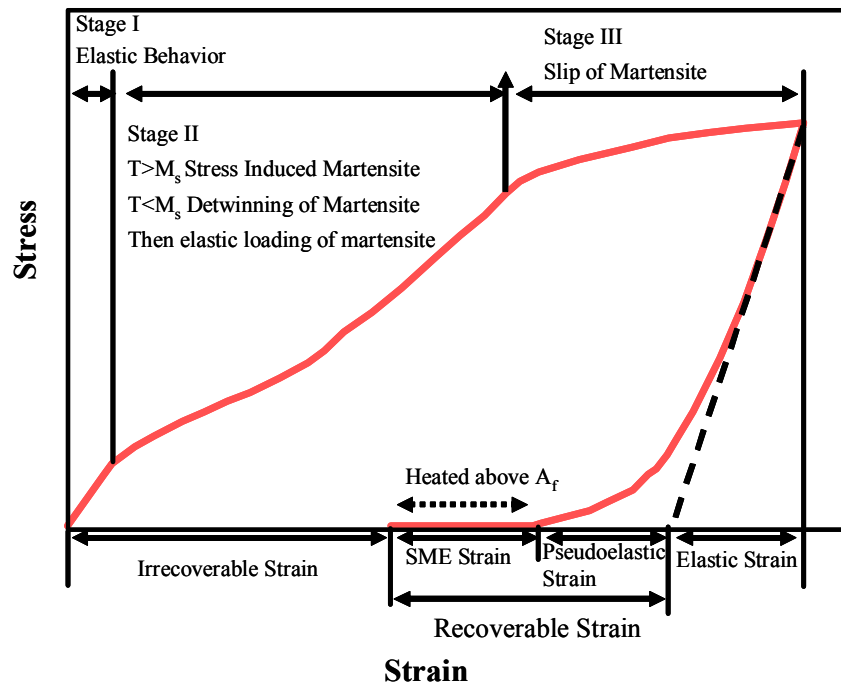
Figure 2.5 Schematic stress-strain behavior of shape memory alloys [48].

In shape memory effect, the remembered shape is the shape of parent phase. Remembering the shape of both parent and martensite phases under certain conditions is known as two-way shape memory effect (TWSME). TWSME occurs if internal stress fields due to microstructure bias certain martensite variants to lower the energy of the system and leads to external shape change. The first report of two-way shape memory effect on TiNi alloys was published by Wang and Buehler [49]**.** The required conditions necessary for TWSME are; 1) introduction of plastic deformation [50, 51], 2) constraint aging [52]**,** 3) thermal cycling [53], and 4) martensite aging due to symmetry-conforming short range order [54]**.** Certain stress sources are created during these processes such as dislocation configurations and precipitates which produce internal stress fields to choose specific martensite variants to lower the energy of the system and create the certain shape of martensite.

2.3 Conventional Shape Memory Alloys

Shape memory alloys (SMAs) which demonstrate thermoelastic martensitic phase transformations have revolutionized the development and use of active materials in the last 40 years by providing large reversible shape changes and very high actuation forces. The unique shape memory behavior was publicized in 1963 [55] when the equiatomic NiTi binary alloy, the most well-known SMA, was shown to exhibit shape memory effect at the U.S. Naval Ordinance Laboratory, that brought the true scientific and technological value of these alloys into realization. After 1960s, especially in late 70s and early 80s when extensive research on Cu and NiTi based alloys started in the U.S. and Japan, processing-microstructure-functional property relationships in these unique alloys were revealed and several commercial applications have been attained since then. After all these work and development, shape memory alloys are now being used as functional materials for pipe couplings, electrical connectors, various actuators and sensors, biomedical devices, springs, and glass frames.

Conventional SMAs display superelasticity and shape memory effect behaviors usually at temperatures near or below ambient temperature. Among many SMAs, NiTi and Cu-based alloys are the most utilized ones due to their excellent mechanical and functional properties. Phase transformation temperatures of available binary NiTi and ternary Cu-based alloys (CuZnAl, CuNiAl, CuNiBe, etc.) are usually below 100 °C [56] and 200 °C [57], respectively.

2.3.1 Cu-based Shape Memory Alloys

Among Cu-based SMAs, Cu-Zn based have actually been used and Cu-Al based SMAs have shown promise. Many Cu-based SMAs posses martensitic transformation from body centered cubic ordered parent phase to a mixture of monoclinic β' and orthorhombic γ' martensitic phases [58]. The martensitic transformation start temperature of Cu-40at%Zn alloy is far below room temperature [59]. Thus, to increase the M_s temperature and to stabilize the parent phase, ternary elements such as Al, Ga, Si and Sn are added. CuZnAl ternary alloys exhibit the most excellent properties as

compared to other Cu-based SMAs due to their higher ductility and resistance to grain boundary fracture properties. M_s temperature of Cu-Al alloy is a little above room temperature when the Al content is 14wt%. The alloys with Al content higher that 14wt% are susceptible to precipitation of a second phase γ_2 which does not undergo phase transformation. When Ni is added as a ternary element, precipitation of γ_2 is suppressed. However, as the Ni content increases the alloy becomes brittle [60]. Excellent SME is observed in CuAlNi alloys with Al content close to 14wt% and with 4.5wt%Ni content.

The mechanical properties of Cu-based shape memory alloys highly depend on the resistance to grain boundary fracture since it occurs very easily. For instance, the fracture stress of single crystal CuAlNi alloys is about 600MPa while that in the polycrytals is 280MPa [61]. Therefore, above A_f, no superelasticity is observed in polycrystalline CuAlNi alloys since grain boundary fracture occurs before the martensite is stress induced, however, they exhibit superelasticity as large as 18% in the single crystalline state [62]. The intergranular cracking occurs not because of the impurities at the grain boundaries such as Bi, Sb, S, P, O and Pb which are known to cause intergranular embrittlement of Cu [60], but instead, takes place due to elastic and plastic incompatibilities between grains, a consequence of high elastic anisotropy [63].

The detailed studies on CuAlNi alloys have shown that the formation of stress induce martensite along grain boundaries upon quenching is the main reason for intergranular cracking. If the stress due to the displacement associated with the formation of stress induced martensite is not accommodated by a deformation mode, to maintain compatibility at a grain boundary, the displacement causes a crack of a width which depends on the orientation mismatch between two adjacent grains [64]. Small grain size, small orientation dependence of transformation strain and ease of plastic deformation might be the conditions to reduce the crack size. CuZnAl alloys are rather ductile in polycrystalline state due small orientation dependence of transformation strain, thus, they exhibit pseudoelasticity (superelasticity) at stresses as high as 300MPa [1].

2.3.2 TiNi Shape Memory Alloys

As opposed to Cu-based SMAs TiNi alloys show good ductility eventhough they are intermetallic compounds. Such unique feature is the result of their low elastic anisotropy. In addition to their high ductility, they have superior corrosion resistance and ability to recover their initial shape after deformation [1, 2]**.**

Many researches studied the phase diagram of NiTI systems since thermal treatments are important to improve the shape memory properties NiTi alloys. Laves and Laves et al. [65] first reported the single phase TiNi at near equiatomic composition. Poole and Hume-Rothery confirmed the decomposition of TiNi into Ti_2Ni and $TiNi_3$ which was first determined by Duwez and Taylor [66, 67]. It was found that TiNi phase extends to lower temperatures, however, the solubility range decreases with lowering temperature on Ni-rich side [66, 68]**.** Purdy et al. [68] first determined that the martensitic transformation proceeds with a diffusionless process at low temperatures although they did not use the term "martensitic transformation". After the discovery of martensitic transformation in TiNi alloys in 1963, Wasilewski et al. [69] determined a new phase, Ti_2Ni_3, and noticed that there is a vertical boundary on the Ti-rich side and solubility range of TiNi phase is very narrow at 500°C and below.

Up to this point, although some of the basics of the phase diagram were established, there were some difficulties in understanding all the phase transformations and the presence of some of the phases like Ti_2Ni_3. Nishida and his co-workers [70] studied extensively the transformations at high temperatures in the Ti-52at%Ni alloy. They found that at lower aging temperatures and shorter aging times Ti_3Ni_4 phase appears, at higher aging temperatures and longer aging times $TiNi_3$ phase forms and at intermediate aging temperatures and times Ti_2Ni_3 phase nucleates. The phase diagram of Ti-Ni alloys by Massalski [71] can be found in Figure 2.6.

The solubility limit on the Ti-rich side of the binary TiNi alloy is almost vertical and precipitation of Ti_2Ni phase preferentially appears at grain boundaries in bulk NiTi alloys. These precipitates decrease the fracture strength and degrade the shape memory behavior of the NiTi alloys. The possible solution to this problem is producing the Ti-

rich NiTi alloy in thin film forms and heat treating the thin films at high temperatures like 700°C for 1 hour or longer times like 10 hours at 500°C for the equilibrium distribution of Ti$_2$Ni precipitates in the grains [72]. Since the amorphous thin film supersaturates Ti atoms at high temperatures or during longer heating times excess Ti can precipitate upon crystallization [73].
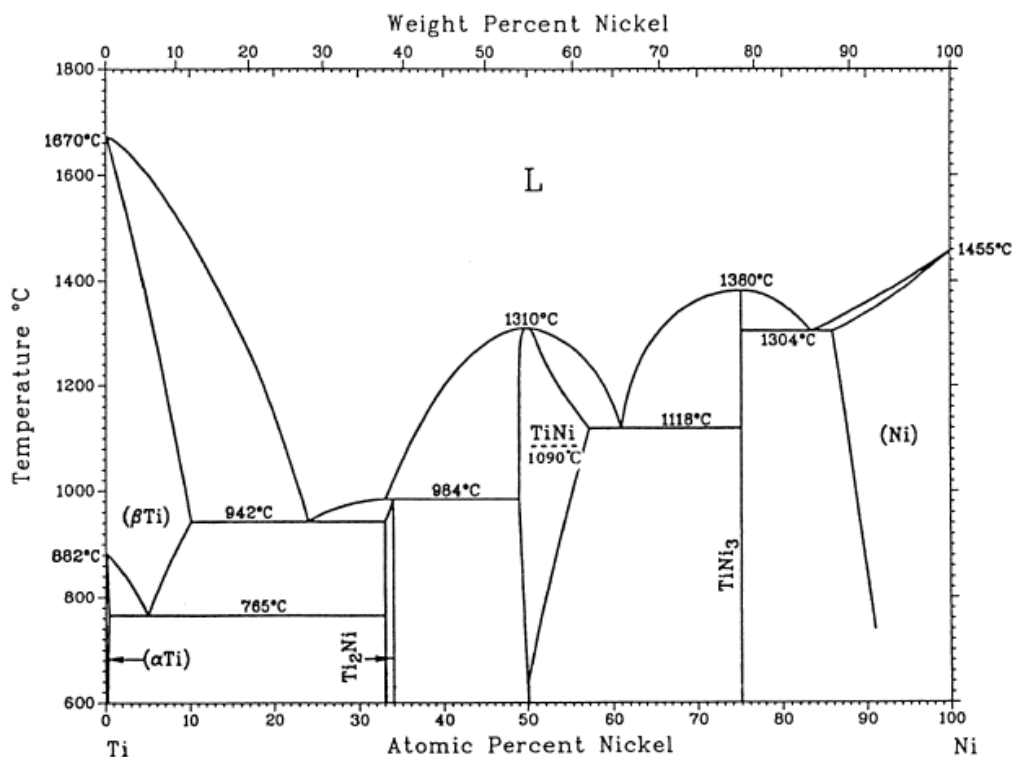
Figure 2.6 Phase diagram of binary NiTi [71].

Fully annealed near-equiatomic NiTi alloys transform from B2 to monoclinic B19' phase martensitically upon cooling. If near equiatomic TiNi alloys is thermally cycled or thermo-mechanically treated, the martensitic transformation occurs in two steps, i.e., B2 to R-phase and then to monoclinic B19' phase [74]. B2 to R transition is also martensitic. The R-phase was first reported as tetragonal phase, however, rhombohedral distortion was recognized later [75, 76]. Ni-rich TiNi alloys which are aged at an appropriate temperature and ternary TiNiFe and TiNiAl also show two-step

phase transition [77-79].

2.3.2.1 Self Accommodation and Twinning in NiTi Alloys

In NiTi SMAs, martensite variants form self accommodated structure to minimize the energy of the system. Between B19' martensite and B2 parent phase, there are 12 lattice correspondences resulting in 24 martensite variants. Self accommodation NiTi alloys can be characterized by triangular morphology which is presented in Figure 2.7 [80]. When TiNi alloys are cooled down below M_s temperature, the martensite can transform to 24 possible internally twinned variants to form self accommodating structure. The interphase between each two of three variants is a twin plane. There are 16 subgroups forming the triangular self accommodating morphology around each of the $[001]_{B2}$ poles, indicating 48 possible combination of variants can form such triangles [80].

(a)   (b)
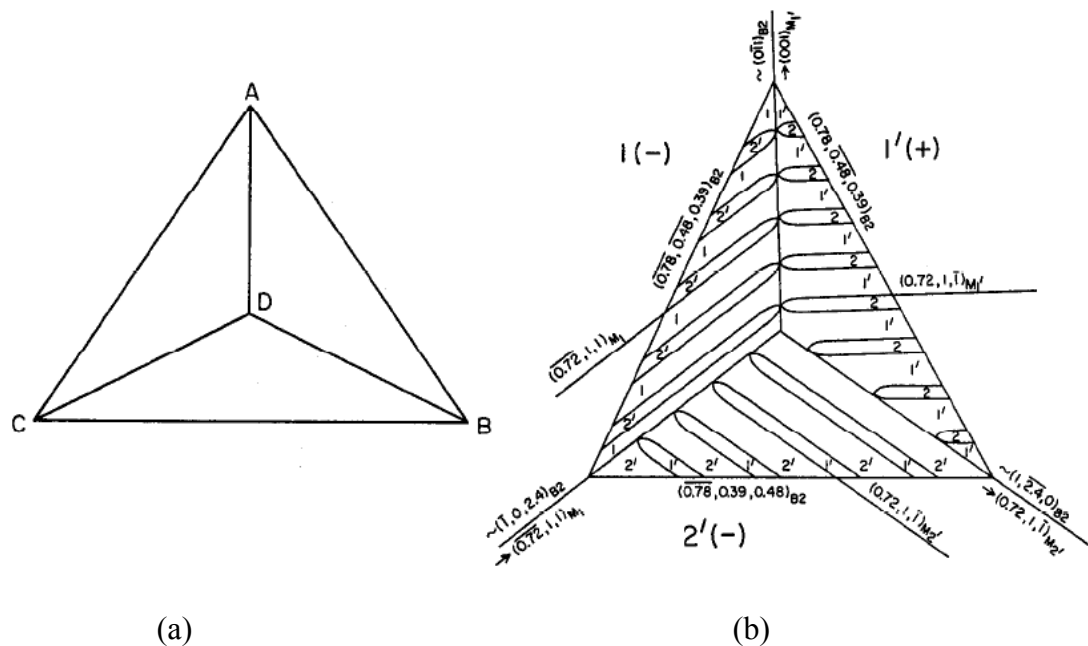
Figure 2.7 a) Schematic representation of triangular morphology and b) crystallographic relationships between the variants in the triangular morphology [80].

In all self accommodating structures martensite variants have twin relations with each other and when an external force is applied the most favorable variant grows at the expense of others, resulting in net shape change. As discussed in section 2.1 the lattice invariant shear in SMAs is twinning which is schematically shown in Figure 2.8. K_1 is invariant plane and K_2 is the other undistorted plane. The plane which is normal to K_1 and parallel to η_1 shear direction is the shear plane. η_2 is the intersection of K_2 and the other shear plane. If K_1 and η_2 are rational and K_2 and η_1 are irrational the type of twinning is called type I twinning, if it is the opposite then the twinning is called type II twinning. If all of them are irrational, compound twinning takes place [1].
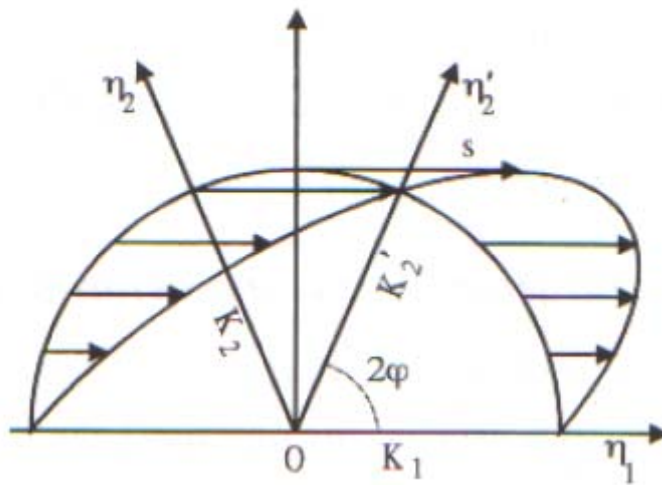
Figure 2.8 The deformation of a sphere into an ellipsoid and the definition of K_1, η_1, K_2 and η_2 [1].

2.3.2.2 The Effect of Thermo-Mechanical Treatments on NiTi Alloys

All the aforementioned studies showed that the shape memory behaviors of NiTi alloys depend on the thermo-mechanical history such as aging, cold deformation and

severe plastic deformation [5]. In this section, the effect of the thermo-mechanical treatments (TTs) on shape memory characteristics of NiTi alloys such as transformation temperatures, transformation and irrecoverable strains will be revealed. In addition, the effect of the thermo-mechanical treatments on the microstructural evolution such as twinning mode evolution and grain size refinement will be summarized.

2.3.2.2.1 The Effect of Thermo-Mechanical Treatments on Transformation Temperatures

The transformation temperatures of the NiTi alloys are highly dependant on the composition of the alloy and the thermo-mechanical treatments. For instance, on the Ni-rich side of TiNi alloys, the transformation temperatures decrease to subzero levels with the increase in Ni-content. Aging treatments cause the formation of Ti_3Ni_4 precipitates which increase the transformation temperatures due to depletion of Ni in the matrix. The transformation temperatures of the aged Ni-rich TiNi are still below room temperature and depend on the amount and size of the precipitates while Ti-rich NiTi alloys are less sensitive to the aging treatments, because the formation of Ti_2Ni precipitates keeps the Ni-content of the matrix to be of equilibrium. Figure 2.9 shows the aging time effect on the M_s temperatures of one Ni-rich and one Ti-rich NiTi alloys [84]. M_s temperatures are not affected from heat treatments in near equiatomic NiTi alloys since precipitates do not form upon aging [77].

The transformation treatments of NiTi alloys are also affected from the cold deformation or severe plastic deformation. It is known that cold deformation suppresses the transformation temperatures to very low temperatures such that no transformations were detected down to -60°C in Ni-rich NiTi alloys and equiatomic NiTi alloys [9, 82]. The transformation temperatures of cold deformed NiTi alloys can be increased by subsequent annealing at intermediate temperature like 350°C. M_s temperature of the cold deformed Ti-50.9at%Ni alloy at 350°C was determined as slightly above room temperature [82]. The increase in M_s temperature in Ni-rich NiTi alloys can be attributed to rearranging and annihilating the tangled dislocations and the formation of Ti_3Ni_4

precipitates. The increase in transformation temperatures was also observed in cold deformed and annealed equiatomic NiTi alloys [9].
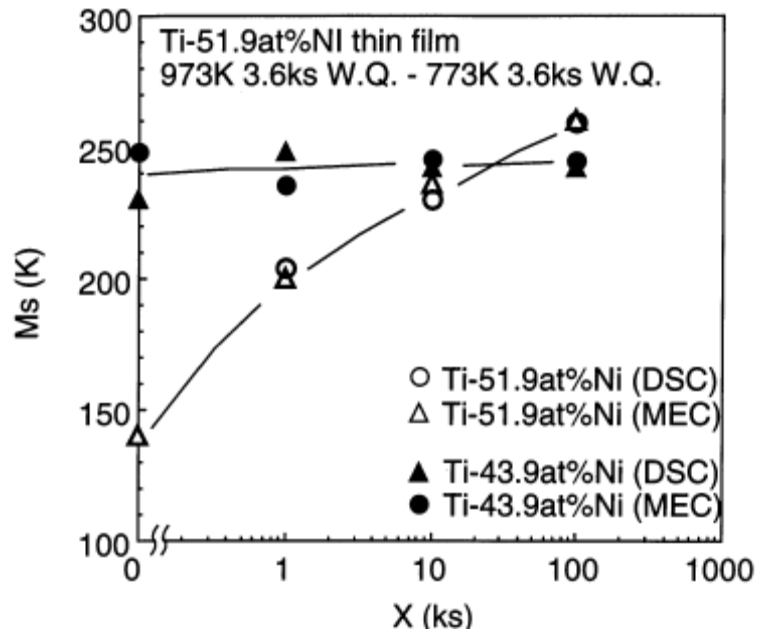
Figure 2.9 Effect of aging time on M_s temperature of Ni-rich and Ti-rich NiTi SMAs [81].

The transformation temperatures of equiatomic NiTi alloys are also affected from thermal cycling while they are not affected from thermal cycling in Ni-rich NiTi alloys. This implies that the precipitates in Ni-rich NiTi alloys suppress the cyclic effect. On the other hand, the transformation temperatures of equiatomic NiTi alloys decreases with the number of cycles which can be attributed the dislocation formation. The dislocations which are formed during thermal cycles suppress the martensitic transformation.

Severe plastic deformation also affects the transformation temperatures of NiTi alloys. It was found that M_s temperature of the equiatomic NiTi alloy which is deformed at 300°C only for 1 pass decreased down to 72°C while M_s of the solutionized equiatomic NiTi alloy is around 80°C. The R-phase start temperature (R_s) of Ti-50.8at%Ni alloy which is ECAE processed at room temperature is detected as 40°C only

after annealing at 350°Cfor 30mins while martensite transformation is still not clear [20]. The affect of severe plastic deformation can be attributed to the formation of dislocations.

2.3.2.2.2 The Effect of Thermo-Mechanical Treatments on Twinning Mode and Grain Size in NiTi Alloys

The mechanisms to accommodate the shape change which occurs through the deformation of NiTi alloys differ according to the deformation mode and amount. The most common twinning system in solutionized NiTi is <011> type II twinning which was first found by Knowles and Smith [83, 84]. Zheng et al. [84] studied the studied the effect of amount of cold rolling on the twinning modes in Ti-49.8 %at Ni alloy and revealed that up to 12% area reduction (AR), coalescence of martensite variants is the mechanism for accommodation of the shape change. The dominant twinning mode is still type II twinning but some type I twinning is also observed. The intervariant boundaries became curved, distorted and blurred eventually. After 16% AR, the deformation took place mainly inside the variants; formation and rearrangement of structural bands and formation of new twins would occur. Type I and compound twinnings operate and consume type II twinning. Otsuka et al. [85] determined $\{1\bar{1}\bar{1}\}_m$ type I twins. Gupta and Johnson found $(001)_m$ compound twins and $\{011\}_m$ type I twins [86]. Onda et al. [87] determined the conjugate pair of $(001)_m$ compound twin which is $(100)_m$ and Nishida et al. [88] found $\{20\bar{1}\}_m$ twins although they cannot be lattice invariant shear. Waitz et al. [24-26] studied the effect of severe plastic deformation via high pressure torsion on the twinning modes of NiTi alloy and showed that martensitic transformation causes a unique "herring-bone" morphology of the martensite composed of fine lamellae containing nanotwins. Strain energy calculations and high resolution transmission electron microscope analysis lead to the conclusion that compensation of the transformation strains occurs by the $(001)_m$ nanotwins [26]. $(001)_m$ and $(001)_m$ compound twinnings can be considered as the deformation twinning in martensite since

one of the slip systems of NiTi is [100](001) and it is proposed that <100> compound twin is created by the slip of a/2 on the (001) plane because of the presence of a partial pseudo-mirror [89, 90]. Kockar et al. [9] found deformation twins in the austenite in heavily deformed equiatomic NiTi alloys and revealed the formation of highly refined twins which have $(13\bar{1})$ twinning plane and high dislocation density in the equiatomic NiTi samples which were ECAE processed at 300°C. Severe plastic deformation leads to the formation of compound twins in martensite and deformation twins in austenite.

Waitz et al. [25] studied the effect of severe plastic deformation using high pressure torsion on the grain size and the corresponding transformation behavior of Ni-50.3at%Ti alloys. The range of the grain size is from 5 to 350nm in the HPT processed and then annealed samples. It was found that the martensitic transformation is suppressed in the grains smaller than 60nm and the R-phase transformation only causes small transformation strains in the grains between 15 and 60nm. Large transformation strains which occur in B2 parent phase to B19' martensite transformations are reduced with the formation of very fine (001) compound twins [25]. It was also proposed that the grain size refinement changes the transformation sequence from B2→R phase→B19' to minimize the overall energy which opposed the transformation. Martensitic phase transformation of nanostructures NiTi alloys, high density of grain boundaries acts as transformation barrier and causes austenite stability in the grains and change the transformation path [24-26].

The grain size refinement also affects the other shape memory properties of NiTi alloys such as transformation temperatures and superelasticity. There are two approaches to the effect of grain size on the M_s temperature. One of them is the decrease in grain size increases M_s which is attributed to the homogeneous nucleation of martensite phase caused by internal stress arising from high anisotropy of nanoscale grain size [91]. The other approach is the decrease in grain size decreases the M_s temperature due to the increase in density of grain boundaries which act as transformation barriers and cause austenite stabilization.

Grain size refinement has influence on the pseudoelastic behavior of NiTi alloys. It was reported that small grain size is effective to improve pseudoelasticity since grain boundaries would support the back stress needed for back transformation and act as nucleation sites for martensite. Saburi et al. [92] demonstrated that Ti-50.5at%Ni alloy with 50μm grain size shows complete pseudoleasticity, however the alloy with 1mm grain size shows 85% recovery when the samples are tested at 40°C.

2.3.2.2.3 The Effect of Thermo-Mechanical Treatments on Texture

Single crystals and cold rolled polycrystals studies showed that mechanical response and transformation behavior of NiTi alloys are highly orientation dependent [93]. For instance, tensile stress-strain curves of a cold rolled NiTi sheet show a flat stress-plateu during tension along the rolling direction while along the transverse direction the material strain hardens quickly [93]. This is attributed to the deformation behavior of the three types of twins which are (001), $(1\overline{1}1)$ type I and $<011>$ type II twins differs along rolling and transverse directions. Gall et al. [19] showed that [111] orientation showed poor cyclic degradation resistance and rapid increase in the permanent strain with cycles [15] and revealed that cold rolled Ni-rich NiTi polycystals has a strong texture of $<111>\{110\}$ type [19]. It was also found that the critical resolved shear stress depends (CRSS) on orientation in aged NiTi single crystals which demonstrate tension-compression asymmetry. These deviations are attributed to the strong local stress fields surrounding the coherent Ti_3Ni_4 precipitates which alter the orientation relationship of CRSS [19].

[001] orientation in single crystalline NiTi alloys show the superior fatique response as compared to the other orientations, because in NiTi alloys, the slip systems were reported to be {100}<001> and {110}<001> [17].

In the literature, there is a lack of knowledge on the texture evolution of polycrystal NiTi alloys with severe plastic deformation. The texture evolution with ECAE studies focus on generally one element materials like Cu, Ti and W. These studies showed that texture highly depends on the processing routes and number of passes in

ECAE. The definitions of the routes will be given in section 2.5. It is found that after the first pass of ECAE the typical shear-type texture $\{111\} < 110 >$ is dominated, however after three passes, $\{001\} < 110 >$ texture type can be seen [94]. Since the preferred austenite texture formation near [001] pole in NiTi alloys can suppress the dislocation formation, NiTi alloys are generally ECAE processed for more than three passes to achieve 001 texture. However, texture formation also depends on the ECAE temperature and at relatively higher processing temperatures strong texture is not expected [9].

2.3.2.2.4 The Effect of Thermo-Mechanical Treatments on Thermal Cyclic Response of NiTi Alloys

NiTi SMAs as actuation devices produce large forces/stresses up to 500MPa over 4-8% strains; however their thermo-mechanical responses may vary significantly due to change in chemical compositions, material processing and thermo-mechanical cycling. There are vast amount of work on the stress-induced martensitic transformations in NiTi at temperatures above A_s revealing the effects of stress and strain level, cycle, prestraining and strain rate on the transformation characteristics. For instance, thermo-mechanical cycling leads to evolution of plastic strain which imparts internal stresses such that martensite stabilization occurs during transformation back to austenite. Miyazaki et al. [18] studied large plastic deformations above A_s in $Ni_{50.6}Ti$ alloy. It was found that if the material was deformed to the range of 4-7% level the strain is not recovered completely, since the deformation is accompanied both by twinning and dislocations. Miller et al [8] studied the effect of cold working and annealing temperature on the transformation and plastic strain of equiatomic NiTi alloy under applied stress. They found that the increase in the level of cold working raises stress level for the onset of plastic deformation and decreases the additional development of plastic strain with cycling. The maximum transformation strain levels of the alloy cold worked 20%, 30% and 40% and annealed at different temperatures for various time ranges do not change much and are 5-5.5%. The sample 10% cold worked shows maximum level of 6.1% transformation strain.

Several studies have been conducted on SPD of NiTi SMAs by Valiev and his colleagues [27, 29] and Karaman et al [20]. The former group studied the mechanical properties of HPT and ECAE processed NiTi alloys. They reported that NiTi alloy processed by HPT and subsequent annealing leads to an increase in the strength at failure up to 2650MPa with an elongation to failure of 5% [28]. However, they only investigated the microstructural evolution and mechanical properties of the alloys. The later group studied the effect of ECAE on shape memory properties transformation and irrecoverable strain levels of NiTi alloys [9, 20]. They reported that thermal cyclic stability is improved in the ECAE processed samples which is attributed to the refined microstucture and nanometer range deformation twins [9]. They revealed that under 200MPa, the irrecoverable strain level of equiatomic NiTi alloy, ECAE processed at 300°C, decreased down to 0.2% from 0.8% which is irrecoverable strain level of the 30% cold drawn and subsequently annealed equiatomic NiTi alloy.

2.4 High Temperature Shape Memory Alloys (HTSMAs)

The existing HTSMAs can be classified in three regimes in terms of their transformation temperature ranges: 100°C to 400 °C, 400°C to 700°C, and 700°C and over. Such classification is a result of different issues and operative microstructural mechanisms associated with each temperature range and available alloy systems. Some of the known HTSMAs are NiTi with Pd, Pt, Zr, and Hf additions, Ti-Pd, Ti-Pt, Ni-Al, Ni-Mn, TaRu, NbRu, TiIrPt and ZrCu-based binary and ternary systems. In addition, there are few new alloy systems with transformation temperatures lower than 100°C but demonstrating superelasticity at high temperatures. These high temperature superelastic alloys are CoNiGa, CoNiAl, NiFeGa.

NiTi alloys with Pd, Pt Zr and Hf and Zr-based intermetallics are the most common HTSMAs in the first temperature regime. Firstov and his coworkers studied the Zr-based quasibinary intermetallics [95, 96]. They reported that these alloys suffer from transformation-induced plasticity and are significantly more brittle than the NiTi based ternary alloys. Thin films, on the other hand, have demonstrated improved high

temperature shape recovery as compared to their bulk counterparts [96]. The shape memory behavior and further information about NiTi alloys with Pd, Pt, Zr and Hf will be summarized in subsection 2.4.1.

The challenge on the high temperature superelastic alloy systems such as CoNiGa, CoNiAl and NiFeGa is poor workability because these alloys suffer from poor ductility, thus the practical use of these new alloys depends highly on the solution to this problem [97-98]. It was reported that introduction of γ second phase improves the workability of the alloys both at high temperatures and at room temperature as well [97-98].

The number of HTSMA systems with transformation temperatures higher than 400 °C is quite limited. The martensitic transformation in binary and ternary Au-Ti and Ti-Pd alloys occurs in the second temperature regime and has been extensively studied by Donkersloot and Van Vucht [35]. They have also explored the phase transformation characteristics of equiatomic binary Ti-Pt system for which the transformation temperature is around 1000 °C, in the third temperature regime. The main issue with the alloys in the second regime is dynamic recrystallization and martensite aging effect in the course of forward and reverse phase transformation. Otsuka and his co-workers have focused on the recrystallization process in TiPd alloys which appears to be directly affecting the high temperature shape memory response and transformation stability [99, 100]. The ordinary martensite aging, recovery and recrystallization, and other diffusional processes occur at temperatures below reverse transformation start temperature (A_s), even in very short times, competes with diffusionless martensitic transformation, and cause an increase in A_s. Such degradation in transformation and cyclic degradation response prevent the long term use of these alloys.

The binary Ta-Ru and Nb-Ru intermetallics which have transformation temperatures higher than 700°C demonstrate multistage phase transformations and undergo B2 to tetragonal to monoclinic martensitic transformations [101, 102]. The equiatomic compositions result in the best shape recovery with low thermal hysteresis [101]. TaRu and NbRu exhibit low strain recovery, 2% under compression and around 5% and 4% under tension, respectively [102]. They are based on equilibrium phases and

transitions as opposed to metastable phases in conventional SMAs, thus, they don't show overaging effects caused by decomposition and precipitation at elevated temperatures.

2.4.1 NiTi HTSMAs with Pd, Pt, Zr and Hf

NiTi-based ternary alloys with the addition of one of Pd, Pt, Zr, and Hf have been the most studied HTSMAs up-to-date. Although the transformation temperatures of NiTiAu are higher than NiTiPd for a given composition, there is not much work performed on this alloy. It was found that AuTi binary alloys exhibit B2 to orthorhombic B19 martensitic transformation [35]. Wu and Wayman studied the ternary TiNiAu alloys and found that NiTi alloy with 5-10at% Au transforms from B2 to B19' monoclinic structure and NiTi with 40-50at%Au transforms form B2 to B19 orthorhombic structure. The later two alloys have transformation temperatures higher than 450°C [103, 104]. The other alloy system which has received little attention like the TiNiAu alloys is TiNiPt since they are very expensive materials. M_s temperature of TiNi alloy with 0-10at%Pt decreases slightly, however at higher levels of Pt, M_s temperature increases linearly up to 1040°C for 50at%Pt addition [35, 36]. TiNi alloys with 16at%Pt or greater, it is found that there is a one step transformation which is B2 to B19 orthorhombic martensite [36]. Zr is added to TiNi alloys at the expense of Ti which is opposite to Au and Pt additions for Ni. Mulder et al. determined that M_s temperature of NiTiZr alloys increases with a rate of 18°C/at% of rate [105]. It was also observed that the transformation temperatures decrease during thermal cycling which was attributed to the precipitation on the alloy. Basically, TiNiZr alloys are the least potential ones in high temperature shape memory alloys because they exhibit poor ductility and unstable shape memory response.

Hf is added to NiTi alloys at the expense of Ti, however, the amount of Hf addition is limited since there is no continuous solid solution between NiTi and NiHf. The transformation temperatures of the alloy do not increase much up to 10at% Hf but at concentrations higher than 10at%, transformation temperatures increase linearly up to 525°C at 30at%Hf. [106, 107]. TiNiHf alloys show B2 to B19' monoclinic martensitic

transformation as in binary NiTi, if the Hf content is less than 15at%. The alloys which contain higher than 15at%Hf show B2 to orthorhombic B19 martensitic transformation [109, 109]. The second phases suh as $(Ti,Hf)_2Ni$ and $(Ti+Hf)_4Ni_2O_x$ were identified in NiTiHf alloys [110, 33]. Although the former may be desirable for improving the shape memory properties, the latter is not desirable as it may influence the workability and shape memory properties [111]. The disadvantages of TiNiHf alloys are the large hysteresis and poor shape memory behaviour. It was reported that the hysteresis is on the order of 40-50°C and sometimes even larger. It was observed that shape recovery is 80% when the $Ni_{50}Ti_{38}Hf_{12}$ is deformed at room temperature to a strain of 2.5% which is attributed to the high stress for the reorientation of martensite and detwinning but the low critical stress for slip [33]. Meng et al. [108, 110] examined the tensile properties of $Ni_{49}Ti_{36}Hf_{15}$ at room temperature and above A_f temperature and observed significant strain hardening which means martensite reorientation is not easy. To increase the critical shear stress for slip, Karaman's group studied severe plastic deformation of NiTiHf alloys and they observed an increase in the recoverable transformation strain (recoverable strain) and a decrease in the irrecoverable strain levels under constant stress experiments [13]. They also investigated the thermal cyclic behavior of the $Ni_{49.8}Ti_{42.2}Hf_8$ alloy after severe plastic deformation via equal channel extrusion and found that cyclic stability is improved and thermal hysteresis is decreased [13].

NiTi alloys with 10at%Pd or less transform from B2 to B19' monoclinic martensite with significantly reduced transformation temperatures, for instance, M_s is -26°C in NiTi alloy with 10at%Pd. [36]. In contrast, the addition of Pd more than 10at% increases transformation temperatures and changes the martensite type to orthorhombic martensite [36]. The transformation temperatures increase with the Pd content almost linearly reaching 510-563°C for $Ti_{50}Pd_{50}$ binary alloy [35, 112].

PdTi and NiTi binary alloys form a continuous solid solution with a serious decrease in transformation temperature by the amount of Ni content in the ternary alloy [36]. The intermetallic phase $Ti_2(Ni,Pd)$ which is isostructural to the face-centered-cubic Ti_2Ni phase in binary titanium-rich NiTi alloys was found in ternary NiTiPd alloys

[113]. The other phase detected in NiTiPd alloys is titanium carbides or oxycarbides (TiC or Ti(C,O)) [34]. The size of the intermetallics is usually several microns while the sizes of carbides and oxycarbides are average of 0.5μm.

Otsuka et al. has reported that the shape memory behavior of TiNiPd alloys is fairly good at room temperature however becomes poor with increasing temperature due to the decrease in critical shear stress for slip [114]. Lindquist and Wayman reported 6% unconstrained shape recovery [36]. Khachin et al. reported 4% complete strain recovery which is introduced by applying 200MPa stress in torsion for $Ni_{13}Ti_{50}Pd_{37}$ [115]. Otsuka and his co-workers studied the shape memory effect in $Ti_{50}Pd_{50}$ alloys and reported poor shape memory behavior which can be attributed to the low critical stress for slip such that high density of slip is introduced in addition to twinning in martensite [116]. NiTi alloys with 40-50at%Pd shows 0.5% shape recovery when loaded in tension.

The first requirement for being high temperature shape memory alloys is having high transformation temperatures, however; this is not sufficient for desirable SME. As explained above NiTiPd alloys also suffer from low critical stress for slip especially at high temperatures which causes plastic deformation during phase transformation and thus, poor shape memory behavior. Thus, to improve the shape memory response of the NiTiPd alloys different approaches has been used such as alloying with a fourth element, precipitation hardening or thermo-mechanical treatments. Yang and Mikkola examined the effect of boron addition to the shape memory characteristics of $Ni_{22.3}Ti_{50.7}Pd_{27}$ alloy and found 90% shape recovery for 2-3% applied deformation under compression [38]. Boron has no real effect on the shape memory characteristics; however, they determined an increase in the ductility of the alloy at room temperature and attributed this increase to the grain refinement due to boron addition. The other method to improve the shape memory characteristics of the NiTiPd alloys is using alloy which slightly deviates from stoichiometry to generate homogeneously distributed Ti_2Ni precipitates as in $Ni_{19.4}Ti_{50.6}Pd_{30}$ alloy [39]. It was observed that 90% recovery rate when the material is deformed to total strain of 6% at 100°C which is about 10% higher than $Ti_{50}Ni_{30}Pd_{20}$ [39]. The improvement of shape recovery was attributed to the hardening effect by the

homogeneously distributed Ti_2Ni precipitates. In addition, some thermo-mechanical treatments were applied to modify the microstructure and strengthen the material by grain refinement and dislocation formation. Goldberg and his coworkers reported the improvement of shape memory properties of $Ti_{50}Ni_{30}Pd_{20}$ after cold rolling and subsequent heat treatment. They claimed superelasticity for the first time in $Ti_{50}Ni_{30}Pd_{20}$ after annealing the alloy at 673K and testing at 535K [41]. Cai et al. [114] studied the effect of thermal cycling on the shape memory properties of $Ni_{19.4}Ti_{50.6}Pd_{30}$ alloys. It was found that M_s temperature, total transformation strain and irrecoverable plastic strain increase with the number of cycles. The change in these parameters occurs quickly in the first 40 cycles and tends to stabilize after then. Thus, thermal cycling may be one of the thermo-mechanical treatments to stabilize the shape memory response of NiTiPd alloys.

The previous works on TiNiPd alloys mostly demonstrated the shape recovery of these alloys under free stress conditions, isothermal mechanical properties and the corresponding microstructural analysis. Most of the applications, however, require shape recovery under applied stress. A research group at NASA Glenn Research Center recently reported the shape recovery of several NiTiPd and NiTiPt alloys and corresponding work outputs [32, 34]. They determined the strain-temperature response of $Ni_{19.5}Ti_{50.5}Pd_{30}$ alloy under various tensile and compressive loads [32]. They observed that there is a slight difference between the tensile and compressive responses and work output first increases, reaches a maximum and then start decreasing with increasing stress level. They also observed an irrecoverable plastic deformation at each stress level [34]. They proposed that before using this alloy in cyclic actuation applications the resistance of the alloy to dislocation slip should be enhanced with promoting the twin formation and motion by the similar methods summarized above.

2.5 Principles of ECAE

In this study, ECAE is chosen as the severe plastic deformation technique to improve the mechanical, shape memory behavior and cyclic response of the equiatomic

NiTi SMAs and NiTiPd HTSMAs. The purpose of choosing ECAE instead of any other severe plastic deformation techniques was revealed in Chapter I. Thus, in this section, the principles of this deformation technique will be presented.

ECAE is a novel technique which permits the application of a large uniform strain without reduction in the cross-section of the work piece [21]. The intersecting angle of the channels is 2φ which is 90°C in our study as denoted in Figure 2.10. The billet is inserted into one of the channels and the punch presses the billet into second channel, thus the work piece passes through two intersecting channels which are 90° to each other. After the extrusion stops, the billet is withdrawn from the channel. The extrusion of a billet through these channels produces simple shear at the channel intersection plane and the billets can be deformed in the same uniform manner repeatedlyexcept the small part of the end regions.

Punch

Billet

φ

Shear Plane

Extrusion
Direction
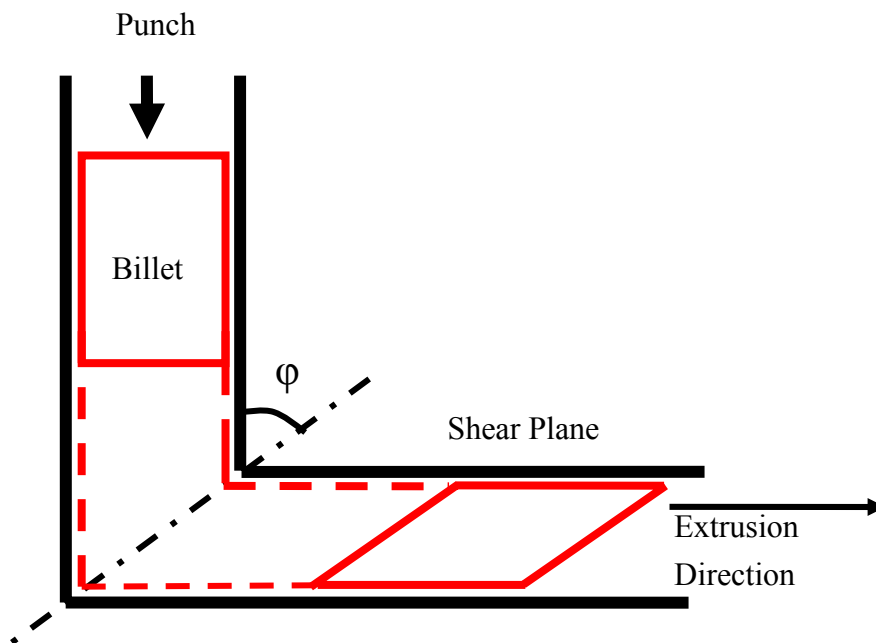
Figure 2.10 Schematic of ECAE process.

ECAE offers several advantages over the other competing processes such as HPT and conventional extrusion. Some of these are the possibility of processing much larger

sample sizes, the ability to control the grain morphology and crystallographic texture, the possibility to apply uniform strain throughout the billet [22].

Multiple passes are possible in ECAE without changing the cross-section. In addition, ECAE permits a variety of deformation configurations by changing the orientation of the billet with respect to the extrusion axis after each pass. This allows the modification of shear planes and directions to develop different structures and textures [117]. There are several possible ECAE routes. The main ECAE routes and their schematics are given in Figure 2.11.

Route A

Route B$_c$: all passes
Route B: N=2, 4, 6…

Route B: N=3, 5, 9…**Route C:** all passes
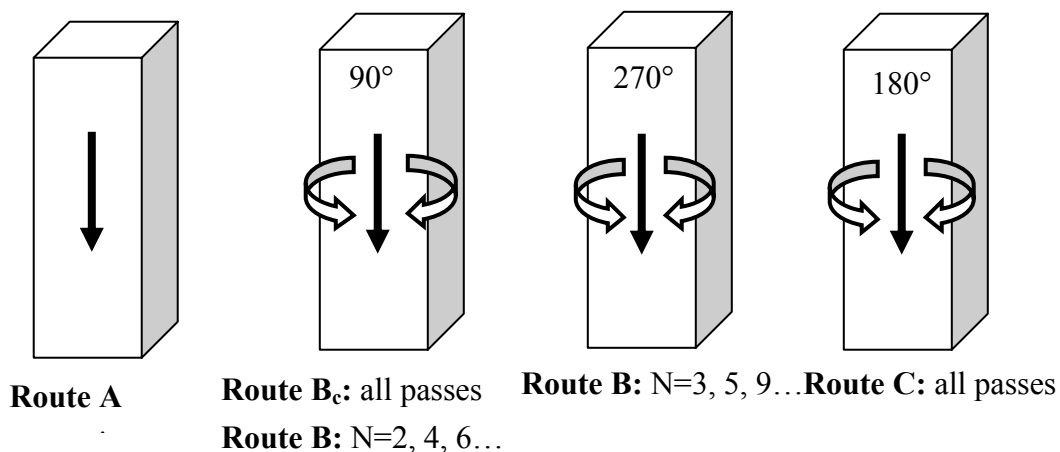
Figure 2.11 The description of the ECAE routes.

Route A: The billet rotation is the same at each pass. The distortion of the material continuously increases and the laminar grain structure is developed.

Route B: The billet is deformed alternatively by rotating about the extrusion axis counter clockwise 90°after every odd numbered passes and clockwise 90° after every even numbered passes.

Route C: The billet is rotated 180° after each pass.

Route B$_c$: The billet is rotated 90° counter clockwise at each pass. Route B$_c$ is the most effective route to obtain equiaxed grains [118].

Route E: This is a hybrid route which is the combination of two passes of Route C, rotating the billet 90°, and then two more passes following Route C. Following Route

E, the materials are highly worked with uniform refined microstructure and high density of high angle grain boundaries [119].

The microstructural evolution and grain refinement mechanism during ECAE, for a common material can be summarized as follows. In the first ECAE pass, the dislocations are introduced. After then, the dislocations start to arrange to decrease the internal energy of the system. In the following passes, subgrains are formed via dislocation arrangement inside original grains with low angle grain boundary configurations. More dislocations are introduced into the material in the subsequent passes and these dislocations are absorbed by the low angle grain boundaries, hence their misorientations increase. As a result, low angle grain boundaries evolve into high angle grain boundaries and grains are refined [120]. Among the five previously defined routes, route B_c is generally the most effective route for grain refinement because there are two sets of available shear planes which intersect and cause grain subdivision [121] and shear bands with different orientations create a uniform network in the materials [121].

CHAPTER III
EXPERIMENTAL PROCEDURE

3.1 As-Received Materials

The fabrication details and initial states of materials used in this study are summarized below. The compositions of the alloys are given in atomic percentages.

Equiatomic NiTi alloy: The $Ni_{49.7}Ti_{50.3}$ alloy was prepared using vacuum induction melting and then hot rolled at 900°C. The initial grain size and M_s temperature of the hot rolled $Ni_{49.7}Ti_{50.3}$ alloy are determined as 40μm and 79°C, respectively.

TiNiPd alloys: The $Ti_{50}Ni_{30}Pd_{20}$ alloys was prepared using vacuum induction melting and solutionized at 1000°C for 1 hour in evacuated quartz tubes to homogenize the as cast structure. Solutionizing was followed by water quenching. The initial grain size and M_s temperature of the solutionized $Ti_{50}Ni_{30}Pd_{20}$ alloy are determined as 30-40μm and 135°C.

$Ti_{50.3}Ni_{33.7}Pd_{16}$ was prepared using vacuum induction melting and hot rolled at 1700°F. M_s temperature of the hot rolled $Ti_{50.3}Ni_{33.7}Pd_{16}$ alloy is determined as 90°C

The carbon and oxygen contents of NiTi and $Ti_{50}Ni_{30}Pd_{20}$ were analyzed by standard combustion methods. For carbon content, ASTM E 350-90e1 was applied using a LECO C-200 analyzer and a calibration was performed using a NIST-traceable standard. For oxygen content, a LECO TC136/EF-100 was used according to ASTM E1409-04 standard procedure. The results are summarized in Table 3.1.

Table 3.1 Carbon and oxygen impurity levels in $Ni_{49.7}Ti_{50.3}$ and $Ti_{50}Ni_{30}Pd_{20}$.

Materials	Carbon (wt%)	Oxygen (wt%)
$Ni_{49.7}Ti_{50.3}$	0.031	0.02
$Ti_{50}Ni_{30}Pd_{20}$	0.051	0.047

3.2 ECAE Processing

ECAE of the initial materials were carried out following different processing routes, temperatures and rates using a 250 ton press as shown in Figure 3.1. Higher ECAE temperatures were necessary due to the limited ductility of the materials. However, the materials were ECAE processed at different temperatures to achieve minimum possible deformation temperatures for each material. This is because of the desire to achieve the maximum possible microstructural refinement by avoiding recovery/recrystallization.

The details of the ECAE schedules are given in Table 3.2 for NiTi and Table 3.3 for NiTiPd and the details of ECAE processes for each material are summarized in sections 3.2.a, and 3.2.b.

Figure 3.1 250 ton extrusion press at Texas A&M University.

3.2.1 ECAE Processing of NiTi

Our previous works on NiTi alloys and the initial works on NiTiPd alloys showed that non-isothermal ECAE led to shear localizations in the billets. A tool was designed which is suitable for isothermal ECAE of NiTi and NiTiPd alloys. The tool was designed for 4.84cm^2 ingots, with length up to 25.4cm. Many of the tool's components were made of Inconel 718 which is a precipitation hardenable nickel-chromium alloy. It was selected for its superior strength at temperatures in the 400 – 600ºC range. After the initial extrusions at 450°C and 425°C, the front leg was remade by H13 tool steel for the extrusion at 400°C and below because, the lower end of the front leg, which partially defines the shear zone where the material is strained, has not been dimensionally stable. In some runs the maximum load has apparently exceeded the capability of this part, and it has deformed. H-13 tool steel can maintain its strength which is higher than Inconel at 400°C and below. The sliding faces of the tool were coated for wear resistance. The tool is operated in a custom furnace that provides a buffer to allow the tool's built-in heaters to be quite effective. The furnace is loosely enclosed so that it can be purged with inert gas. Tools with different cross sections can be replaced if billets with different cross sections are needed to be ECAE processed. The replaceable inserts and the ECAE furnace are shown in Figure 3.2.

(a)   (b)
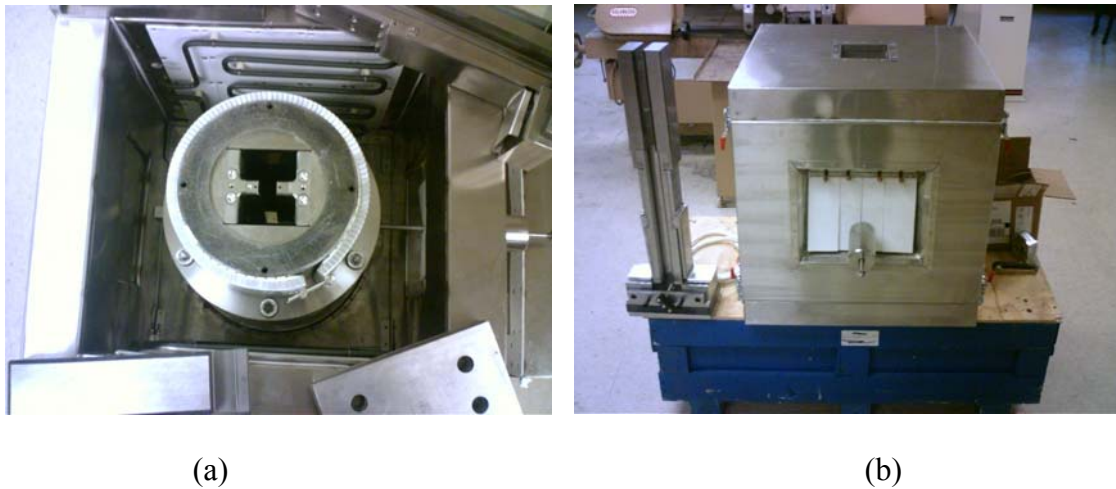
Figure 3.2 a) Replaceable inserts for ECAE processing of billets with different cross sections b) ECAE furnace for isothermal extrusions up to 600°C.

The ECAE billets were cut by electron discharge machine (EDM) from the hot rolled bar into 4.84cm^2 cross section and 10.2cm long bars. The bars were wrapped in brass foil to reduce friction. The ECAE die with a sharp 90° corner angle was preheated to extrusion temperatures. The samples were kept in the ECAE die for 30 minutes before the first pass for uniform heat conduction throughout the billets and then extruded isothermally at 300°C, 400°C, 425°C and 450°C at a rate of 0.005"/sec. The heating periods in the ECAE tool were decreased to 15 minutes before the successive passes to prevent recovery/recrystallization as much as possible and in addition, the heat conduction is easier in the billets which were ECAE processed for one pass than that of in unprocessed billets. ECAE was conducted in nitrogen atmosphere for preventing oxidation. The billets extruded at 400°C and 425°C were rotated 90° in between each pass, (route B$_c$) and the one extruded at 450°C was processed using route E having billet rotation sequence: +180°-90°-180°. The billets were water quenched after each ECAE pass to freeze the ECAE processed microstructure. The bars were straightened and thinned slightly between the passes so they could be reinserted in the tool. Route E was chosen in the initial extrusion because of its lower punch load than that of route B$_c$ and to evaluate the formability of the NiTi alloy at high temperatures before attempting

lower extrusion temperatures using route B_c. Route B_c was selected since it usually results in the most effective refinement with increasing number of passes among all known routes [118,119]. Usually four ECAE passes were used for each billet due to the fact that at least four or higher number of passes are required to obtain significant volume fraction of high angle grain boundaries in body centered cubic structures during ECAE [122]. However only one ECAE pass was used for the billet extruded at the lowest deformation temperature possible for not to cause shear localization at higher number of passes and to obtain sufficient material for further analysis.

Table 3.2 Summary of the equiatomic $Ni_{49.7}Ti_{50.3}$ ECAE processing detail.

Materials	Extrusion Route	ECAE Temperature (°C)	Ext. Rate (mm/sec)
$Ni_{49.7}Ti_{50.3}$	4E	450	0.127
$Ni_{49.7}Ti_{50.3}$	$4B_c$	425	0.127
$Ni_{49.7}Ti_{50.3}$	$4B_c$	400	0.127
$Ni_{49.7}Ti_{50.3}$	1A	300	0.127

3.2.2 ECAE Processing of TiNiPd

The initial extrusions were conducted on $Ti_{50}Ni_{30}Pd_{20}$ alloy which were provided as $2.25cm^2$ cross section were canned in two-piece Ni cans since the cross section of the ECAE die is larger than the cross section of the billets. Ni cans were machined into $4.84cm^2 \times 10.2cm$ long bars using conventional techniques. After inserting the $Ti_{50}Ni_{30}Pd_{20}$ billets into the cans, the cans were copper coated to reduce the friction between the work piece and the walls of the die. The canned billets were heated to ECAE temperature in a furnace for 1 hour before the first pass and 30 minutes before the successive passes. They were transferred to ECAE die as quick as possible to prevent the chilling effect and ECAE processed non-isothermally in the die which was preheated to 300°C. Since the initial ECAE of $Ti_{50}Ni_{30}Pd_{20}$ alloys were conducted non-isothermally

only one of them was successful. The successful ECAE on $Ti_{50}Ni_{30}Pd_{20}$ billets was the one which was conducted at 400°C using Route C for four passes. The other billets experienced shear localization during ECAE. Digital image of a $Ni_{30}Ti_{50}Pd_{20}$ billet ECAE processed 400°C is shown before and after ECAE in Figure 3.3 as an example.

Later $Ti_{50}Ni_{30}Pd_{20}$ billets were provided as $0.75in^2$ cross section rectangular bars. These billets were wrapped in stainless steel foils and lubricated using stainless steel dye to reduce friction. The billets were kept in the ECAE die, which was nitrogen purged and preheated to ECAE temperature, for 45 minutes before the first pass and 30 minutes before the successive passes. The initial billet was ECAE processed isothermally at 600°C using Route C for four passes and the later one was ECAE processed isothermally at 500°C using Route C for 2 passes. The extrusion rate of ECAE processed non-isothermally at 400°C $Ti_{50}Ni_{30}Pd_{20}$ billet is lower than that of the billets ECAE processed isothermally at 600°C and 500°C for preventing chilling effect in the ECAE die which was preheated to 300°C.

$Ti_{50.3}Ni_{33.7}Pd_{16}$ alloy was provided as rounded bars having diameters of 0.4in. Ni cans which were used in the initial $Ti_{50}Ni_{30}Pd_{20}$ extrusions were replaced with commercial purity grade 2 titanium because in some of the $Ti_{50}Ni_{30}Pd_{20}$ extrusions, Ni cans failed in the first or second passes and did not allow running further passes. The reasons of these inevitable failures could be due to the fact that Ni is softer than the $Ti_{50}Ni_{30}Pd_{20}$ alloy. Thus, the rounded bars were canned in commercial purity grade 2 titanium. The canned billets were wrapped in stainless steel foils and lubricated using stainless steel dye. The billets were kept in the ECAE die, which was preheated to ECAE temperature, under nitrogen atmosphere for 45 minutes before the first pass and 30 minutes before the successive passes. ECAEs of $Ti_{50.3}Ni_{33.7}Pd_{16}$ billets were conducted at 450°C using Route B_c for four passes, 425°C using Route B for 2 passes and 400° using Route B for 2 passes.

(a)

(b)

Figure 3.3 Digital images of a $Ni_{30}Ti_{50}Pd_{20}$ ECAE billet (a) before and (b) after 4 ECAE passes at 400°C using Route C.

Table 3.3 Summary of the NiTiPd ECAE processing detail

Materials	Extrusion Route	ECAE Temperature (°C)	Ext. Rate (in/sec)
$Ni_{30}Ti_{50}Pd_{20}$	4C	400	12.7
$Ni_{30}Ti_{50}Pd_{20}$	4C	600	0.127
$Ni_{30}Ti_{50}Pd_{20}$	2C	500	0.127
$Ni_{33.7}Ti_{50.3}Pd_{16}$	$4B_c$	450	0.127
$Ni_{33.7}Ti_{50.3}Pd_{16}$	2B	425	0.127
$Ni_{33.7}Ti_{50.3}Pd_{16}$	2B	400	0.127

3.3 Microstucture Evaluation Methods

The unprocessed materials were examined with optical microscopy (OM) to determine the grain size. Transmission electron microscope (TEM) and scanning electron microscope (SEM) have been utilized to investigate the microstructures of severe plastically deformed materials since the grain boundaries are heavily deformed and can be poorly delineated by OM due to the high dislocation density and the formation of submicron grains. It is necessary to keep track of the grain size and microstructure evolution after ECAE using transmission electron microscope (TEM). All OM samples were mechanically ground down to 1200 SiC grit paper and then polished with 3 and 0.05 microns alumina powder sequentially. They were chemically etched with HF: HNO_3: Glycerol solution with the ratio of 1:4:5 to reveal grain boundaries.

JEOL JSM-6400 SEM equipped with energy dispersive spectrometer (EDS) and Cameca SX-100 electron microprobe equipped with wavelength dispersive spectrometer (WDS) were used to examine the second phase particles in NiTiPd materials. Secondary electron and back scattered electron images were taken to represent the size of particles in the NiTiPd materials. The same OM sample preparation recipe is used to prepare samples for SEM; however, they were not etched in order to investigate only the second phase particles without mixing them with the matrix microstructure. The compositions of the precipitates were determined using wave dispersive spectrometer since WDS

analysis allows a more spectral resolution and more sensitivity than EDS analysis does. The detection limits of WDS ordinarily varies between 300 and 30 parts per million.

TEM studies were conducted using a JEOL JEM-2010 microscope operated at an accelerating voltage of 200 kV. The TEM samples were mechanically ground down to a thickness of 100μm and twin jet electro-polished with a 20vol.% Nitric Acid and 80vol.% Methanol solution at -10°C. In order to examine the parent phase, the sample was heated above austenite finish (A_f) temperature (i.e: 200°C) using an in-situ TEM heating stage. Bright Field, dark field and electron diffraction patterns were recorded.

3.4 Measurement of Phase Transformation Temperatures

The specimens were thermally cycled for 5 cycles during which transformation characteristics was monitored using a Perkin-Elmer Pyris I differential scanning calorimeter (DSC) in nitrogen atmosphere. The heating-cooling rate during the experiments was set to 10°C/min in all experiments. $Ni_{49.7}Ti_{50.3}$ samples were cycled between 20°C and 160°C, $Ni_{30}Ti_{50}Pd_{20}$ and $Ni_{33.7}Ti_{50.3}Pd_{16}$ samples were cycled between 20°C and 200°C.

3.5 Mechanical Testing

The thermo-mechanical experiments were conducted using an MTS 810 servohydraulic test frame. The heating and cooling of the samples was achieved by conduction through the grips which were heated by heating bands and cooled by liquid nitrogen flowing through copper tubing wrapped around the grips with a heating-cooling rate of 10°C/min. Temperature gradient on the sample was kept 2°C/min at maximum during the heating-cooling experiments. An extensometer for high temperature applications with a gauge length of 12.54mm was used to record the axial strains by attaching its ceramic extension rods directly to the tension samples. The digital image of the high temperature extensometer is shown in Figure 3.4. Small dog-bone shaped tension samples with a gauge section of 1.5 mm x 3 mm x 8 mm wire electro-discharge machined (wire EDM) from the billets. The thickness of the tension samples reduced

down to 1.0mm for the monotonic failure experiments for preventing the pins, which are used to attach the tension samples to the MTS test machine, from failure before the sample fails. The sample dimensions are presented in Figure 3.5. Before the experiments, the samples were ground to remove the residue layers formed during EDM. The temperature was measured using a thermocouple directly attached to the samples.
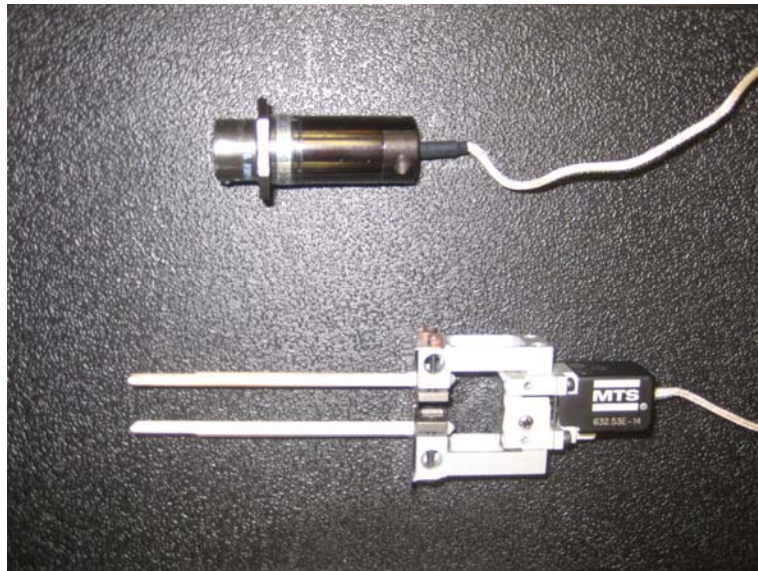
Figure 3.4 The MTS high temperature extensometer used to measure the axial strain.
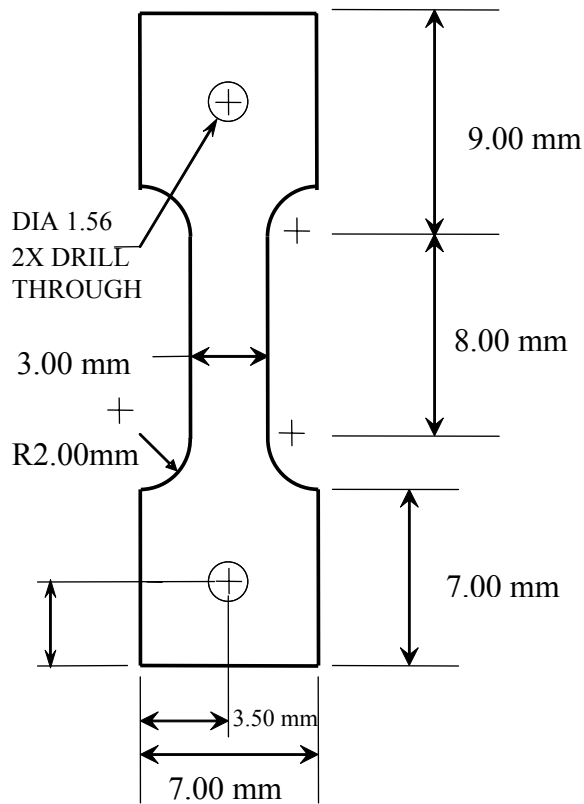
Figure 3.5 A **s**chematic showing the dimensions of the tension test samples.

Three types of experiments were conducted on hot rolled and ECAE processed samples:

1) Tensile failure experiments at $M_s+15°C$ in austenite (to assure thermodynamically equivalent conditions in all samples) in order to determine the effect of ECAE on the flow strength and ductility.

2) Isobaric cooling-heating experiments under increasing stress levels from 50 MPa to 400 MPa with a 50MPa increments to determine the shape memory characteristics such as transformation temperatures, transformation and irrecoverable strain levels as a function of stress and find out the threshold stress level for the onset of irrecoverable strain.

3) Isobaric thermal cyclic experiments up to 10 cycles under 50MPa and 150MPa to evaluate the cyclic stability of the unprocessed and ECAEd samples. 150MPa was chosen for the isobaric thermal cyclic experiments due to the fact that 150MPa is the threshold stress level for the onset of irrecoverable strain.

4) Loading-unloading experiments at constant temperatures to verify and extend the stress-temperature relationships for stress-induced martensitic transformation, martensite reorientation and plastic yield of martensite.

CHAPTER IV

THERMO-MECHANICAL, MONOTONIC AND CYCLIC RESPONSE OF AN ULTRAFINE-GRAINED NiTi SHAPE MEMORY ALLOY

4.1 Preamble

As mentioned in the motivation part of the Chapter I, many practical applications of NiTi alloys require large number of cycles, a stable and reliable shape memory effect. Understanding the thermal and mechanical cyclic behavior that involves irreversible changes is important for the design and utility of NiTi SMAs. However, there are problems frequently reported in the literature associated with cyclic stability of shape memory effect in NiTi alloys [4-6]. For instance, martensite start temperature (M_s) and the irrecoverable (plastic) strain level increase with the number of cycles [6-8]. The cyclic instability in NiTi alloys was attributed to the accommodation of the austenite to martensite phase transformation with dislocation formation in addition to transformation twinning which leads, upon thermo-mechanical cycling, to plastic strain, martensite stabilization and variation in transformation temperature, thermal and stress hysteresis.

A possible solution to the cyclic instability problem is to increase the critical shear stress (CSS) for slip and thus to minimize the dislocation formation upon phase transformation [11]. Major thermo-mechanical treatments in the literature which improve the cyclic stability of NiTi alloys are reported are cold rolling, cold rolling and annealing, thermo-mechanical cycling (training) and severe plastic deformation via HPT and ECAE. The reports on HPT and ECAE usually demonstrate the microstructural evolution and the enhancement of the mechanical properties of NiTi alloys [28]. There is a lack of information on the cyclic behavior of severe plastically deformed ECAE processed NiTi alloys.

In this chapter, the effect of ECAE on microstructural refinement and dislocation

substructure and the corresponding thermo-mechanical, monotonic and thermal cyclic response of the equiatomic NiTi alloy will be investigated. The particular shape memory characteristics such as transformation temperatures, thermal hysteresis, transformation and irrecoverable strains from thermal cyclic experiments will be revealed. Thermodynamic energy contributions to the phase transformations such as stored elastic and irreversible energy will be investigated in consideration with the evolution of microstructure and twin mode. This study constitutes the first systematic work in understanding and building a bridge between the thermodynamics and mechanics of martensitic phase transformation in the ultrafine grained NiTi alloys.

The study on $Ni_{49.7}Ti_{50.3}$ was started by ECAE processing of the alloy. The ECAE processing of the alloys is summarized briefly to refresh the detailed information given in Chapter III as following: hot rolled $Ni_{49.7}Ti_{50.3}$ alloy was ECAE processed at 450°C for four passes using Route E, 425°C for four passes using Route B_c and 400°C for four passes using Route B_c.

4.2 Differential Scanning Calorimetry (DSC) Experiments

Figure 4.1 shows the DSC response of the hot rolled and ECAE processed $Ni_{49.7}Ti_{50.3}$ alloy samples during five thermal cycles. A^* and M^* in Figure 4.1.c correspond to the peak temperatures in the DSC traces. A^* and M^* simply define the temperatures at which approximately 50% transformation occurs and the thermal hysteresis is defined as $A^* - M^*$. There is a notable improvement in the cyclic stability of the transformation temperatures after the ECAE processing as it can be seen in the Figure.

The transformation temperatures, A_s, M_s and R_s, the difference between the first and fifth cycles of A_s and M_s ($A_s^{5th} - A_s^{1st}, M_s^{5th} - M_s^{1st}$) temperatures and the thermal hysteresis in the first cycles for all samples are summarized in Table 4.1. A decrease in transformation temperatures and an increase in thermal hysteresis ($A_s^{5th} - A_s^{1st}$) after 4 pass ECAE process are observed. The decrease in M_s temperature of the sample ECAE

processed at 300°C for 1 pass is not as pronounced as in that of ECAE processed samples for 4 passes. There is no change in the thermal hysteresis of the sample ECAE processed at 300°C as compared to the thermal hysteresis of the hot rolled sample. In the hot rolled sample, the A_s temperature is 88.1°C and decreases down to 84.5°C after 5 cycles, and M_s drifts from the initial value of 79.3°C down to 69.9°C, resulting in the temperature shifts about 9.4°C after only 5 cycles. In the sample ECAE processed at 400°C, there is no shift in the M_s temperature after 5 cycles. The shift of M_s temperature of the sample ECAE processed at 300°C is 2.1°C after 5 cycles.

In equiatomic NiTi alloy the martensitic transformation can occur either directly from B2 to B19' or through the intermediate R phase, B2 →R → B19', depending on the thermo-mechanical treatment [38]. R^* in Figure 4.1 represents the peak temperature of the austenite to R-phase transformation. The intermediate R phase is observed in all four pass extruded samples which is common for deformed NiTi alloys since dislocations introduced during severe plastic deformation process create energy barrier for martensite formation, making the R-phase formation a lower energy alternative [46]. Austenite to R-phase transformation was not observed in the sample ECAE processed at 300°C which can be attributed to the lower dislocation density than that of in ECAE processed samples for four times.

The main observations from the DSC results can be summarized as: 1) The transformation temperatures decrease after ECAE process, however, the effect of ECAE is less pronounced in the sample ECAE processed at 300°C for 1 pass, 2) The thermal hysteresis increases after ECAE, however, there is no increase in thermal hysteresis of the sample ECAE processed sample at 300°C for 1 pass as compared to the thermal hysteresis of the hot rolled sample, 3) Austenite to R-phase transformation is observed in ECAE processed samples for four passes, 4) There is a considerable improvement in the stability of the transformation temperatures after ECAE.

(a)

(b)
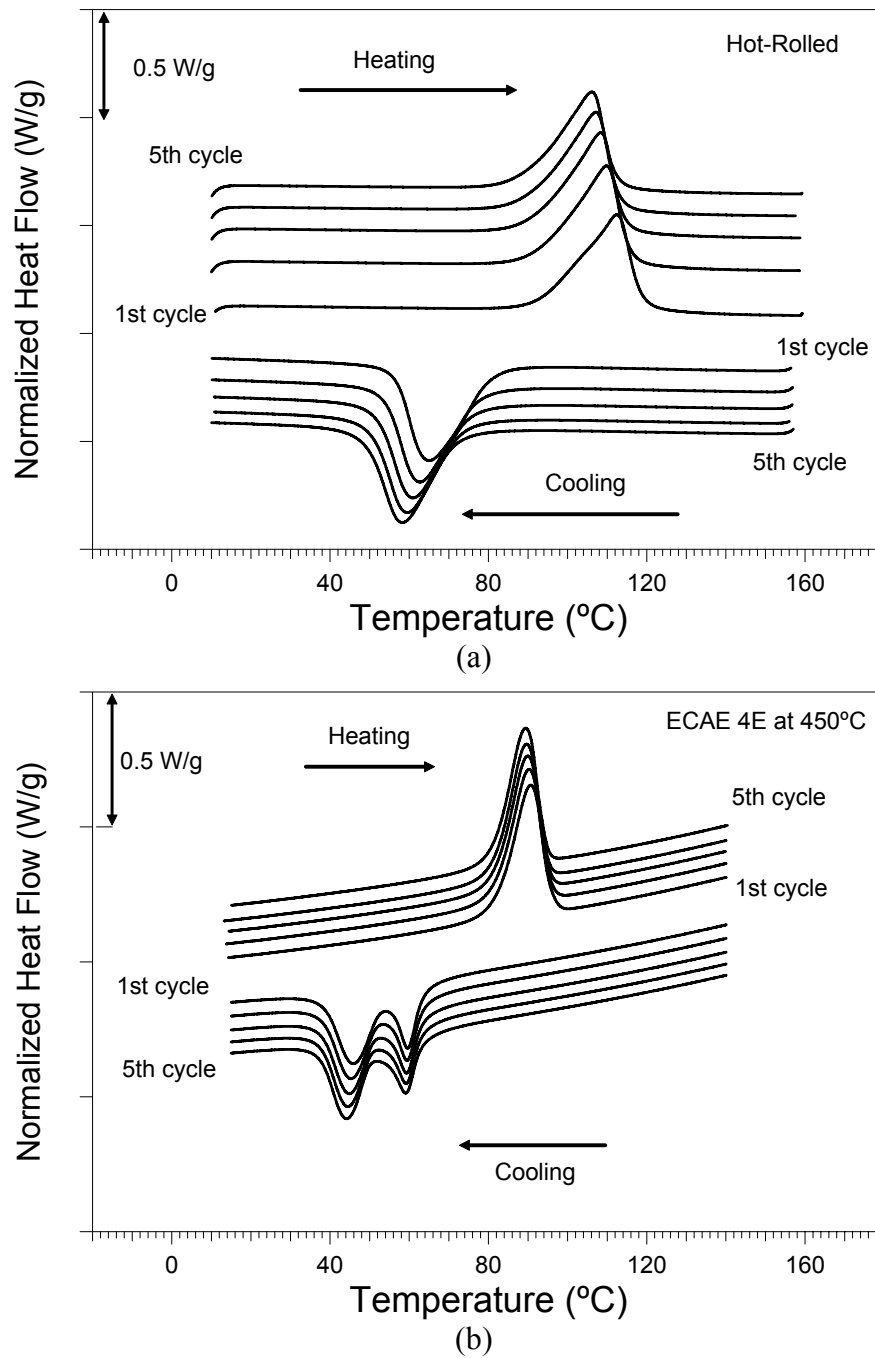
Figure 4.1 Cyclic DSC response of the hot rolled and ECAE processed $Ni_{49.7}Ti_{50.3}$ alloy samples demonstrating the improvement in the cyclic stability of the transformation temperatures upon ECAE processing (a) Hot rolled, (b) ECAE 4E at 450°C, (c) ECAE $4B_c$ at 425°C, (d) ECAE $4B_c$ at 400°C, (e) ECAE 1A at 300°C samples.
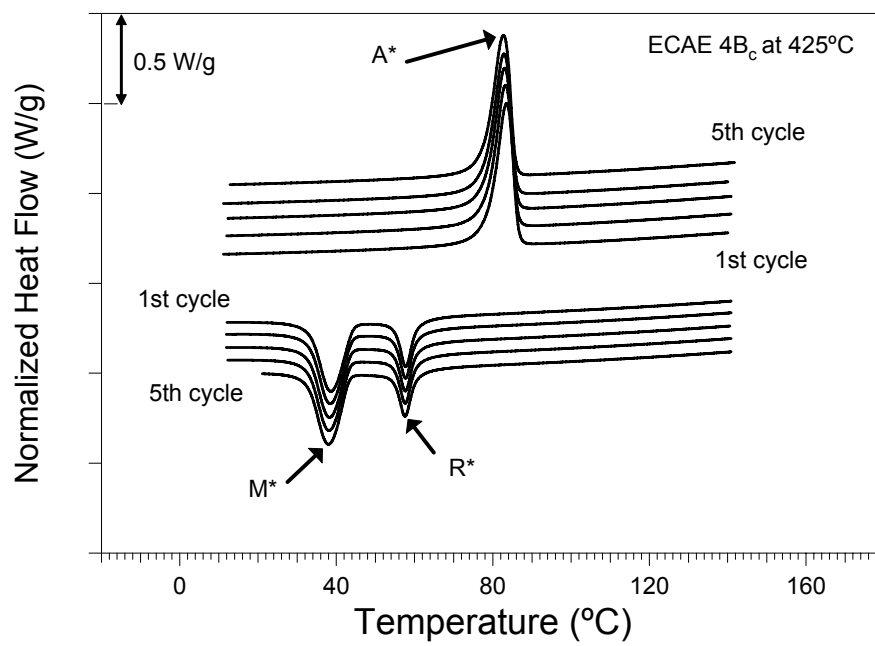
(c)
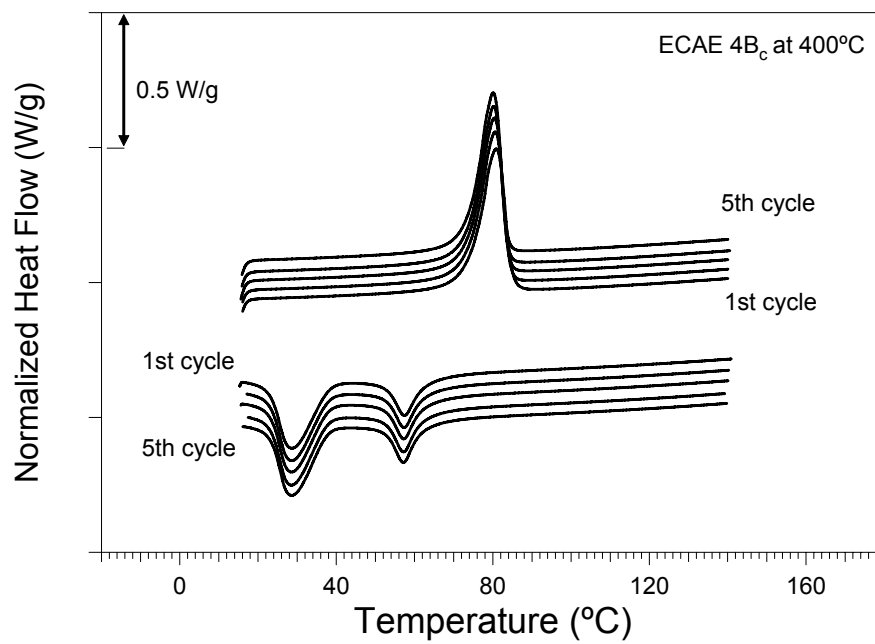
(d)

Figure 4.1 Continued

(e)
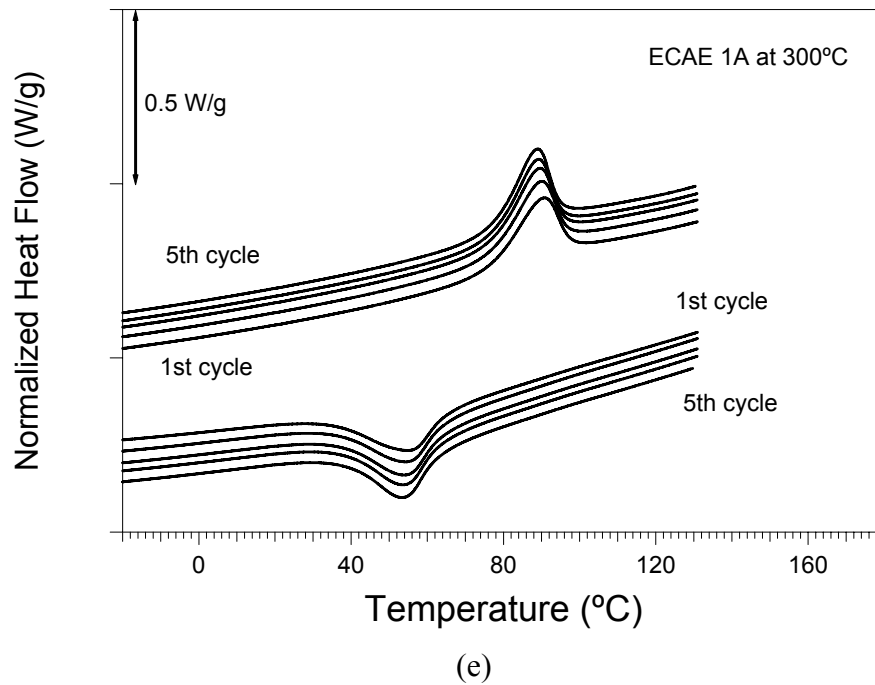
Figure 4.1 Continued

Table 4.1 Martensitic transformation temperatures and thermal hysteresis of hot rolled and ECAE processed $Ni_{49.7}Ti_{50.3}$ alloy at the first and fifth thermal cycles from DSC.

Material	A_s^{1st} (°C)	M_s^{1st} (°C)	R_s^{1st} (°C)	A_s^{5th} (°C)	M_s^{5th} (°C)	R_s^{5th} (°C)	$A_s^{5th} - A_s^{1st}$ (°C)	$M_s^{5th} - M_s^{1st}$ (°C)	$A_{1st}^* - M_{1st}^*$ (°C)
As Received	88.1	79.3	-	84.5	69.9	-	3.6	9.4	36.5
ECAE 4E at 450°C	81	52.1	64	80	49.7	63.4	1	2.4	45.5
ECAE 4B$_c$ at 425°C	78	44.6	61	77	43.9	61	1	0.7	45
ECAE 4B$_c$ at 400°C	73.7	38.6	62	73	38.6	62	0.7	0	52
ECAE 1A at 300°C	74.5	66.1	-	75.7	64	-	1.2	2.1	36

4.3 Microstructural Evolution

Before presenting the thermo-mechanical response of the hot rolled and ECAE processed $Ni_{49.7}Ti_{50.3}$ alloy, it is imperative to understand the microstructural changes induced by ECAE. Figure 4.2 shows the optical microscopy image of the hot-rolled $Ni_{49.7}Ti_{50.3}$ alloy demonstrating the average grain size of about 40μm. Figure 4.3 shows the bright field TEM images of the ECAEd samples taken above the A_f temperature, approximately at 175°C, illustrating the grain size reduction as a function of the ECAE temperature. Note that the magnifications of these images are different. It is clear in the figure that the lower the ECAE temperature is, the refiner the resulting grain size gets. The average grain size of the sample extruded at 400°C is about 0.1μm (Figure 4.3.a) while that for the sample extruded at 450°C is around 0.2~0.3μm (Figure 4.3.c). However, the grain size distribution is relatively wide especially in the samples extruded at higher temperatures. As shown in Figure 4.3, the grain size varies between 0.05 and 0.3μm.
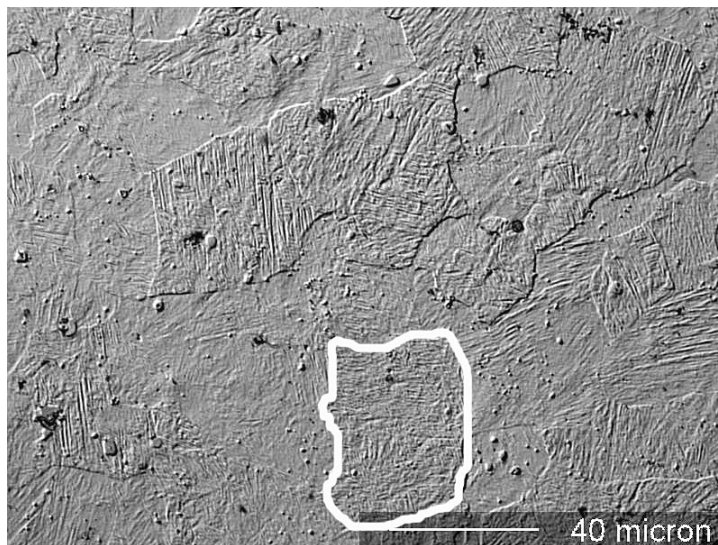
Figure 4.2 Optical micrograph of the hot-rolled $Ni_{49.7}Ti_{50.3}$ alloy demonstrating the initial grain size.

Selected area diffraction (SAD) patterns were also recorded to analyze the existing phases at different grain sizes. Figure 4.4 shows TEM bright field image taken at room temperature from ECAE processed sample at 400°C and the corresponding SAD patterns from the indicated areas which demonstrate the simultaneous presence of R and B19' martensite phases in one apparent grain. In Figure 4.4.b, weak superlattice reflections are the indications for the R-phase. It was recently reported that when the grain size of Ni-50.3at%Ti alloy is in between 0.06 to 0.15μm, the grains mainly contain R-phase and B19' martensite [25] confirming our observations. However, the aforementioned study was conducted on very small HPT processed and heat treated samples. HPT processed amorphous samples were annealed at different heat treatment temperatures to achieve various grain sizes via recrystallization, but mainly in an amorphous matrix.

0.3μm	0.4μm	0.5μm
(a)	(b)	(c)
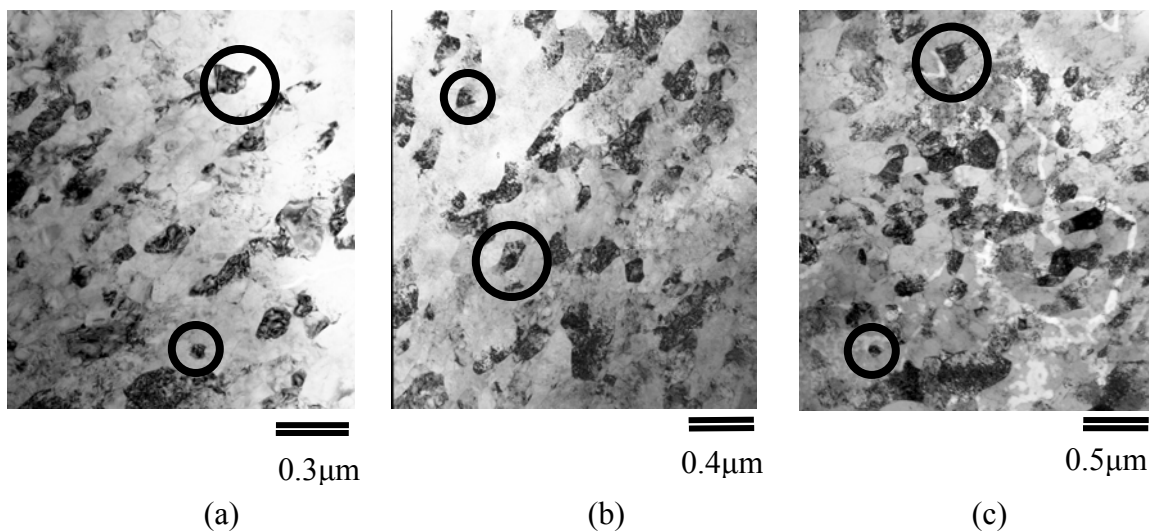
Figure 4.3 Bright field TEM images taken above A_f at 175°C showing the grain size reduction due to ECAE processing. Four ECAE passes following (a) route B_c at 400°C b) route B_c at 425°C and (c) route E at 450°C.

Figures 4.5.a and 4.5.c show TEM bright field images taken at room temperature from the ECAE $4B_c$ sample processed at 425°C and Figures 4.5.b, 4.5.d and 4.5.e are the corresponding SAD patterns from the circled areas in Figures 4.5.a and 4.5.c. Figure

4.5.b depicts the formation of $<011>$ Type II twins and the size of these twins is measured as approximately 30nm. Figures 4.5.d and 4.5.e demonstrate two different twin modes which are $(001)_m$ compound twin and $\{11\bar{1}\}$ Type I twin, respectively. Type II twins are quite common in solutionized and cold worked plus annealed NiTi alloys. Nishida et al. [123] showed that $(001)_m$ compound twinning mode is the most frequently observed one among the $\{11\bar{1}\}$ and $<011>$ twinning modes in grains smaller than 4µm. The rationale behind the observation of these twins will be discussed in detail in section 4.8.1.
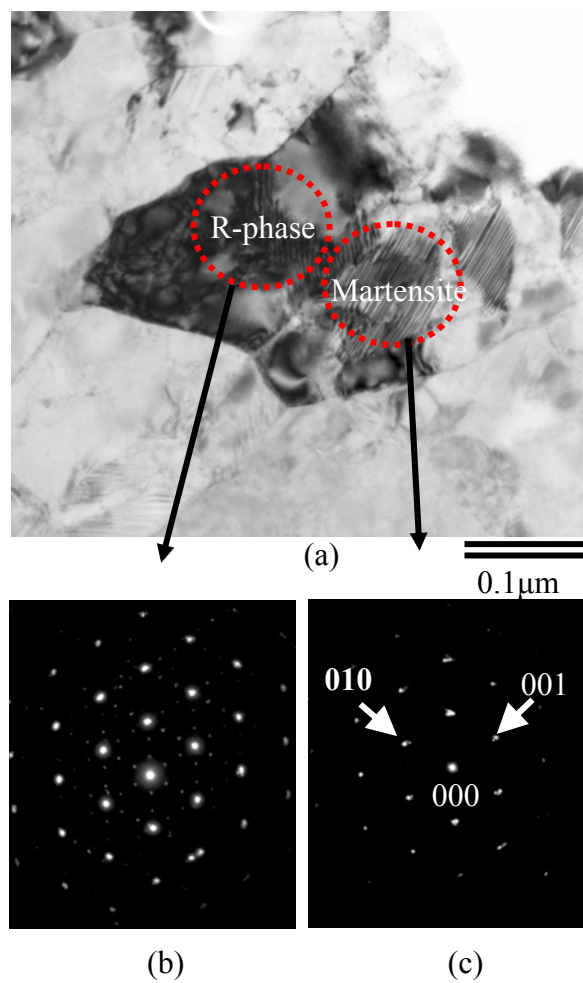
Figure 4.4 (a) Bright field (BF) TEM images taken at room temperature showing the grains containing R-phase and martensite in the ECAE 4B$_c$ sample processed at 400°C SAD patterns of the circled areas in BF showing (b) the R-phase and (c) $[100]_M$ B19' martensite.
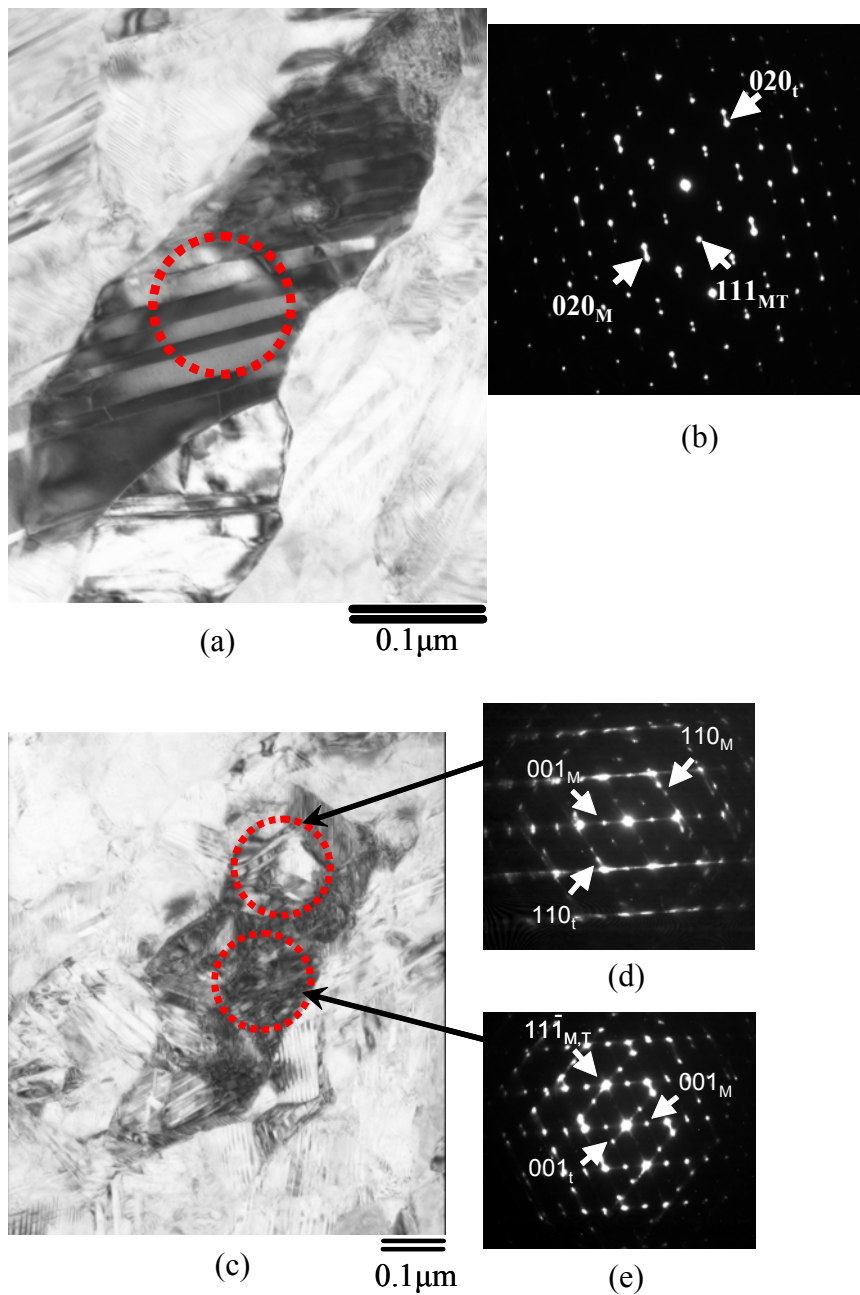
Figure 4.5 Bright field TEM images taken at room temperature from ECAE 4B$_c$ sample processed at 425°C showing (a), (c) twins in martensite, (b) SAD pattern taken from the circled area in (a) showing the $<011>$ Type II twin, and (d), (e) SAD patterns taken from the circled areas in (b) showing the (001) compound twinning and $\{11\bar{1}\}$ Type I twinning, respectively.

Figure 4.6.a shows TEM bright field image taken at 200°C from the ECAE 1A sample processed at 300°C and Figure 4.6.b demonstrates corresponding SAD pattern from the circled area in Figure 4.6.a. Figure 4.6.b depicts the formation of $(1\bar{3}1)$ deformation twins which is a common deformation twinning mode in the high temperature phase of NiTi alloys having thicknesses around 0.02μm. The grain boundaries are not well delineated since the microstructure in Figure 4.6.a demonstrates high dislocation density with high volume fraction of refined twins.

(a)

0.2μm

(b)
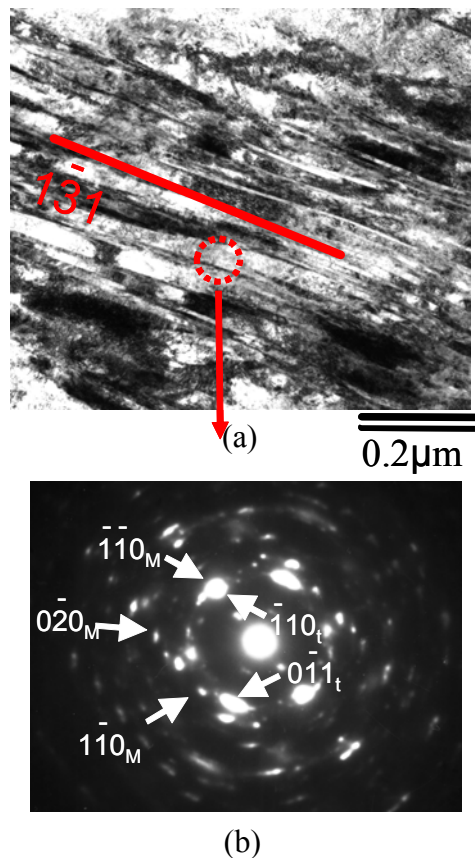
Figure 4.6 Bright field TEM images taken at 200°C from ECAE 1A sample processed at 300°C showing (a) twins in austenite and the relatively heavy dislocation density (b) SAD pattern taken from the circled area in (a) showing the $(1\bar{3}1)$ deformation twin.

Figure 4.7 represents the TEM bright field image of a unique microstructure of B19' martensite which is observed in the sample ECAE $4B_c$ processed at 425°C. The full lines represent the twinned lamellae and the dashed lines represent the junction planes between the twin variants. This unique microstructure is called as "herring bone" morphology [26]. Waitz et al. [26] showed that the $(001)_m$ compound twins observed in nanograins represent a unique "herring bone' morphology of the martensite which are not observed in coarse grained NiTi alloys. The junction planes represented as dashed lines in Figure 4.7 can be either straight or curved. These junction planes are the coherent twin boundaries which are formed to reduce the lattice misfit, thus, the lattice strain at the twin boundary decreases with the formation of these coherent twin boundaries.

0.06μm
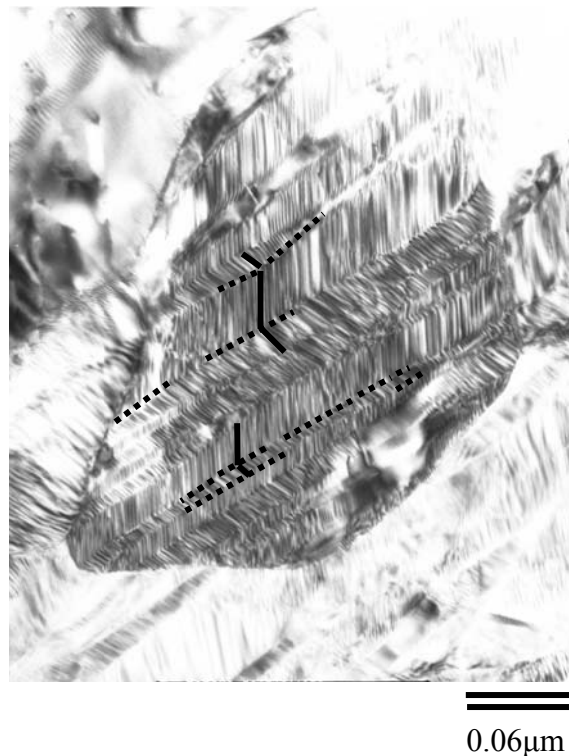
Figure 4.7 Bright field TEM image taken at room temperature from the ECAE $4B_c$ sample processed at 425°C showing "herring bone" $(001)_m$ type twins having an average size of 3nm.

4.4 Monotonic Mechanical Response under Tension

To analyze the effect of severe plastic deformation on the σ_{SIM} and σ_y^M levels, tension tests were conducted to failure on hot rolled and ECAE processed at temperatures 15°C above the M_s of each sample under 50MPa. M_s under 50MPa was chosen as the test temperature to be at the same thermodynamical conditions in all cases. The stresses shown as σ_{SIM} and σ_y^M in Figure 4.8 correspond to critical stress level to induce martensite and the yield stress of stress induced martensite, respectively. Figure 4.8 shows the schematic of a stress-strain curve which is composed of five stages of different types of deformation in a typical SMA at temperatures below M_d. M_d is the maximum temperature at which stress induced martensitic transformation is possible. These deformation stages can be summarized as: Stage 1: Elastic deformation of austenite or martensite depending on testing temperature; Stage 2: Stress-induced martensite formation or martensite reorientation and detwinning of martensite again depending on testing temperature; Stage 3: Elastic deformation of stress-induced martensite; Stage 4: Plastic deformation of stress-induced martensite; Stage 5: Fracture of martensite after necking. Stress dependence of deformation stages was explained detail in Chapter II.

Figure 4.9 illustrates the results of monotonic response of the hot rolled and ECAE processed samples under tension. The stresses, σ_{SIM} and σ_y^M, and the stress differential between them ($\Delta\sigma$) obtained from these experiments are summarized in Table 4.2. σ_{SIM} and σ_y^M stresses are found using the intersecting slopes technique and 0.2% offset value respectively as shown in Figure 4.8.

The yield stress levels of stress induced martensite notably increase with the decrease in ECAE temperature for the same number of passes of ECAE process. The critical stress levels for stress induced martensitic transformation of the samples ECAE processed for four passes were determined to be decreasing. It can be noticed that the stress differential increases in all ECAE processed samples, however, the increase in

stress differential of ECAE 1A at 300°C case is less pronounced as compared to that of the ECAE processed for four passes because σ_{SIM} increases after ECAE process at 300°C for one pass.
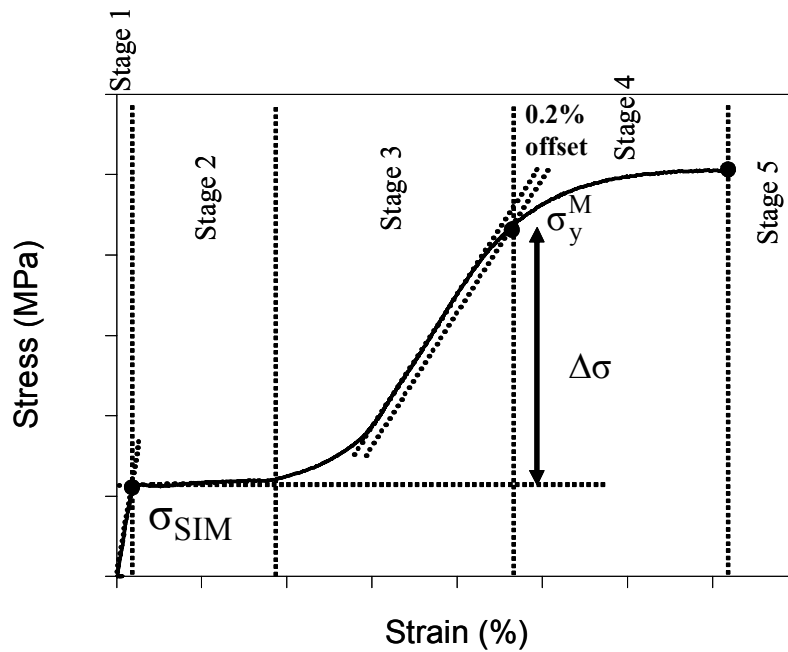
Figure 4.8 Schematic of a different deformation stage in a typical SMA at temperatures below M_d. σ_{SIM} and σ_y^M show the critical stress level to induce martensite and the yield stress of stress induced martensite, respectively.
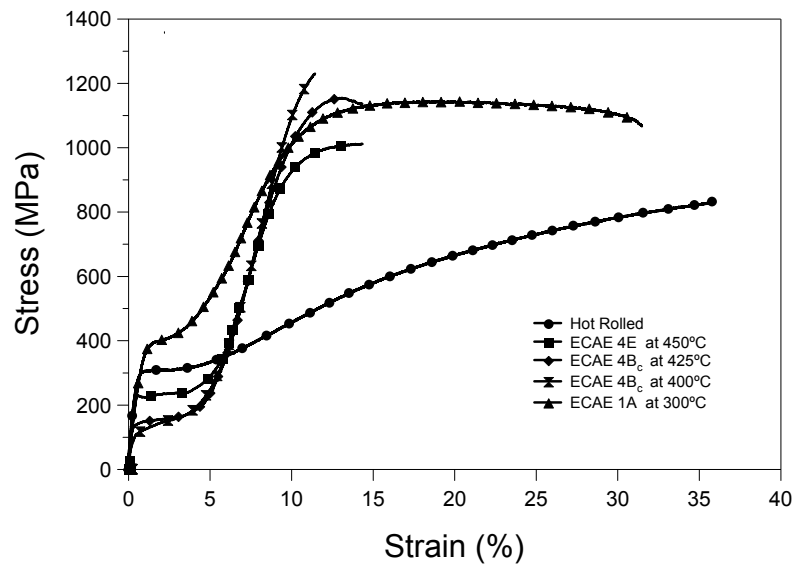
Figure 4.9 Monotonic mechanical response of the hot rolled and ECAE processed Ni$_{49.7}$Ti$_{50.3}$ samples under tension at $M_S^{\sigma=50MPa}+15°C$ to be thermodynamically same condition.

Table 4.2 σ_{SIM} and σ_y^M stresses and the stress differential determined from monotonic mechanical response experiment under tension of hot rolled and ECAE processed Ni$_{49.7}$Ti$_{50.3}$ samples.

	σ_{SIM} (MPa)	σ_y^M (MPa)	$\Delta\sigma\left(\sigma_y^M-\sigma_{SIM}\right)$ (MPa)
Hot Rolled	300	520	220
ECAE 4E at 450°C	220	790	570
ECAE 4B$_c$ at 425°C	150	840	690
ECAE 4B$_c$ at 400°C	120	1020	900
ECAE 1A at 300°C	395	950	555

4.5 Isobaric Thermal Cyclic Experiments

Isobaric thermal cyclic experiments were performed, incrementally increasing the applied stress at each thermal cycle, using the same specimen throughout the test. From these experiments, transformation strain and irrecoverable strain levels are determined at each stress level. Transformation strain is determined from the middle of the temperature range between the extrapolated thermal expansion lines of parent and martensite phases and irrecoverable strain is the strain difference between the heating curve and the cooling curve at $A_f+30°C$ as shown in Figure 4.10. Thermal Hysteresis and the transformation temperature intervals (i.e. M_s-M_f) of the hot rolled and ECAE processed samples are compared. M_s and M_f temperatures are determined from the intersection points of the extrapolated thermal conduction of martensite and the martensitic transformation curves and thermal expansion of austenite and the martensitic transformation curves, respectively. Thermal hysteresis is the temperatue range at the middle of the points between the martensitic transformation and back (austenite) transformation curves as shown in Figure 4.10.
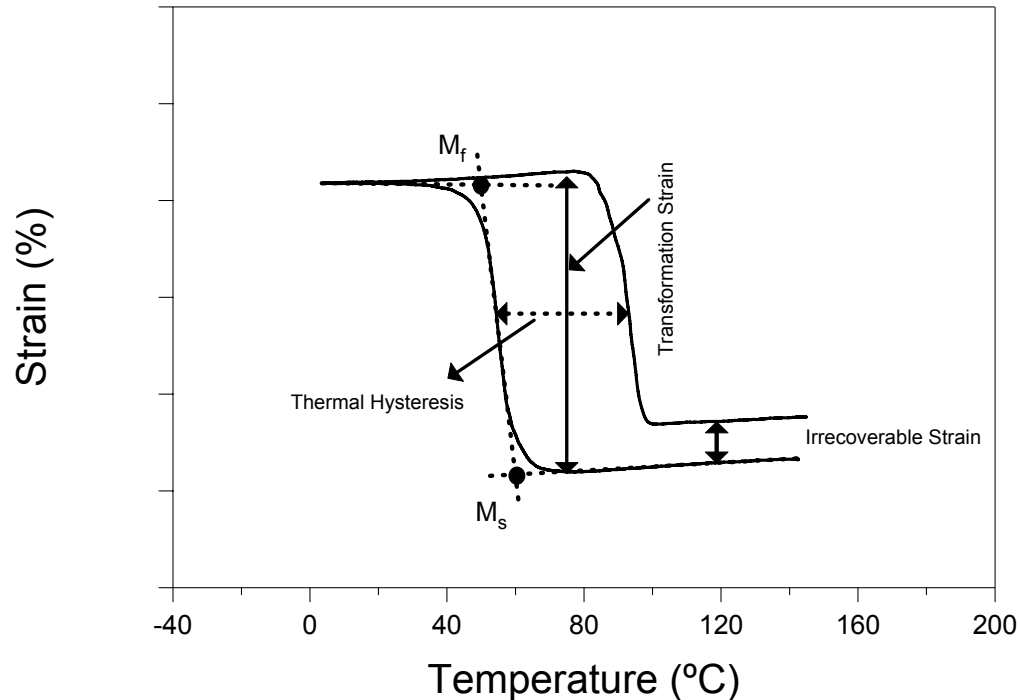
Figure 4.10 Schematic illustration of transformation and irrecoverable strain, M_s and M_f temperatures and thermal hysteresis.

Figure 4.11 shows the strain vs. temperature response of the hot rolled and ECAE processed samples during isobaric heating-cooling experiments. These experiments were conducted under increasing stress levels from 50 MPa to 400 MPa with 50MPa increments to find out the threshold stress level for the onset of irrecoverable strain. M_s temperatures of all samples increase as the applied stress increases which can be attributed to the stabilization of martensite with the increase in stress level. In addition, the transformation temperature interval (i.e. M_f-M_s) is low in the samples ECAE processed for four passes. The samples ECAE processed at 300°C and hot rolled show larger transformation temperature interval. One can observe that the thermal hystereses of ECAE processed samples for four times are larger than that of ECAE processed sample at 300°C for one pass.

Figure 4.12 represents the transformation and irrecoverable strain levels as a function of applied stress level determined from these experiments. It is clear that there

is a significant increase in the irrecoverable strain levels of the hot rolled sample with increasing stress. The ECAE processed samples, on the other hand, all show stable response and the irrecoverable strain levels are negligible up to 100MPa. One can observe a detectable irrecoverable strain only above 200MPa for the samples extruded at 400°C and 300°C. As the extrusion temperature decreases, the irrecoverable strain level also decreases for the four pass ECAE samples. The transformation strain levels of samples ECAE processed at 450°C, 425°C and 400°C increase with increasing stress up to 150MPa and then stabilize above 200MPa and are lower than the transformation strain level of the hot rolled sample. The transformation strain level of the sample ECAE processed at 300°C continues to increase with increasing stress up to 400MPa. Transformation strain levels of the ECAE processed for four passes samples increase up to maximum values of 4.5% at 200MPa and stabilize at higher stress levels, on the other hand the transformation strain level of the hot rolled sample never stabilizes and increases up to 10%. The red markers in Figure 4.12 represent the values determined from comparison experiments to confirm the repeatability of the results. It was observed that the transformation and irrecoverable strain values determined from different experiments are almost the same, except the transformation strain levels of the hot rolled sample from seperate experiments differ slightly. The reason of this difference might be due to sample inhomogeneity. Since there are large strains imparted on the ECAEd samples and the deformation is homogeneous, the similar transformation behavior is expected.

The main observations from Figures 4.11 and 4.12 can be summarized as: 1) the transformation interval (i.e. M_f-M_s) of the samples ECAE processed for four passes is lower than that of the sample ECAE processed at 300°C for one pass, 2) thermal hysteresis of the samples ECAE processed samples for four passes at each stress level is larger than that of the sample ECAE processed at 300°C for one pass, 3) irrecoverable strain levels of the ECAE processed samples are lower than that of the hot rolled sample, 4) the irrecoverable strain levels of the sample ECAE processed at 300°C for one pass at higher stress levels are lower than that of the sample ECAE processed at 400°C for four

passes, 5) the transformation strain levels of the ECAE processed samples are lower than that of the hot rolled sample, and they are more stable above 200MPa.
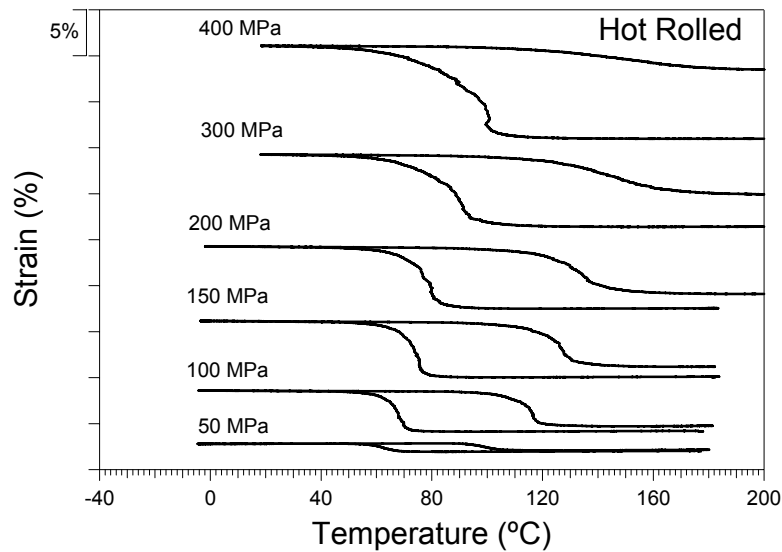
(a)
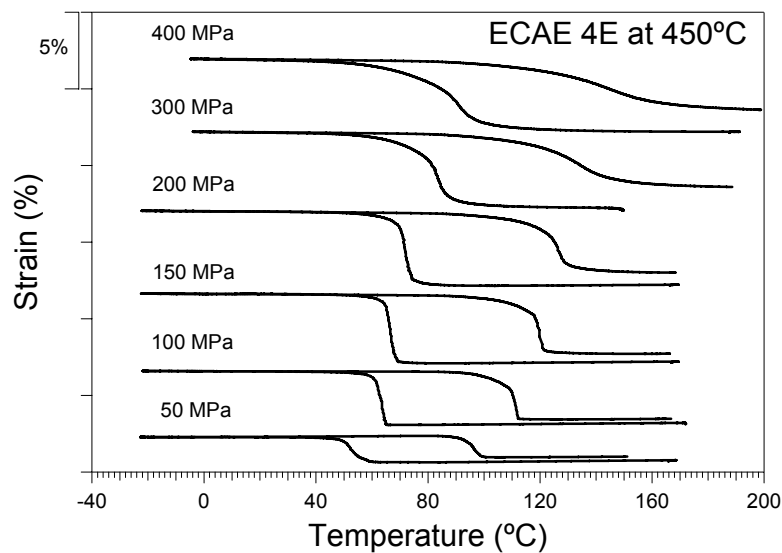
(b)

Figure 4.11 Strain vs. temperature response of the $Ni_{49.3}Ti_{50.7}$ alloy under various constant stress levels during isobaric cooling-heating experiments: (a) Hot rolled, (b) ECAE 4E at 450°C, (c) ECAE $4B_c$ at 425°C, (d) ECAE $4B_c$ at 400°C, (e) ECAE 1A at 300°C samples.
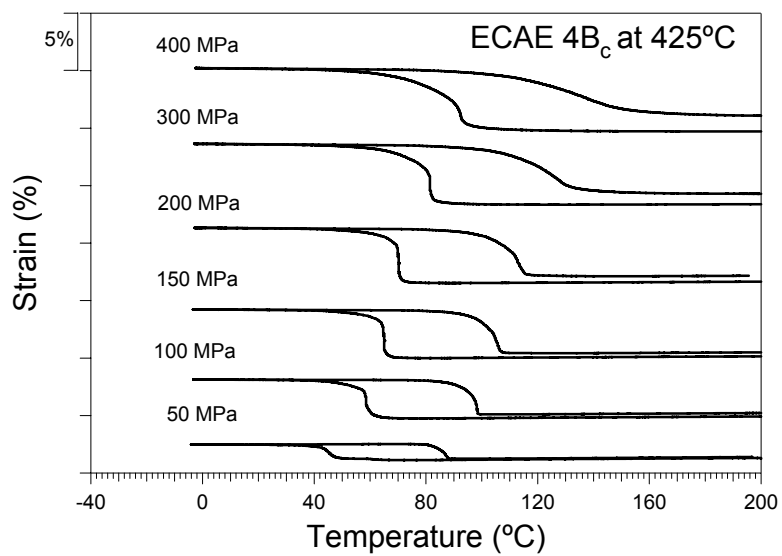
(c)
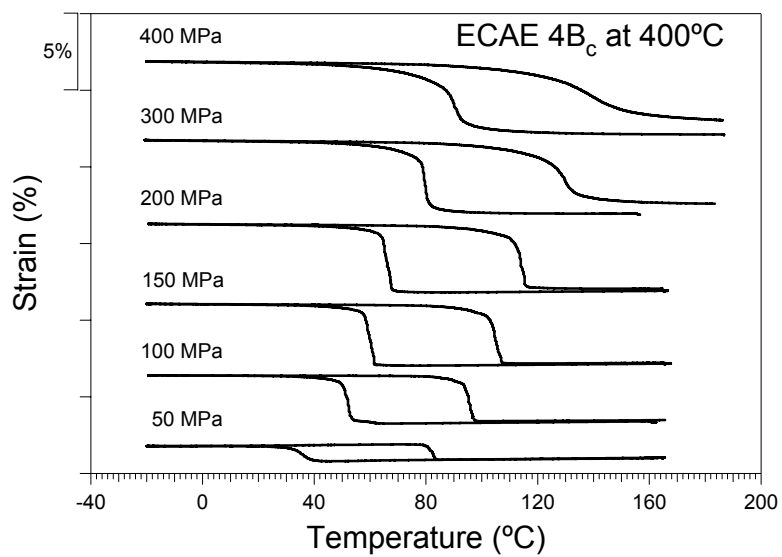
(d)

Figure 4.11 Continued

(e)
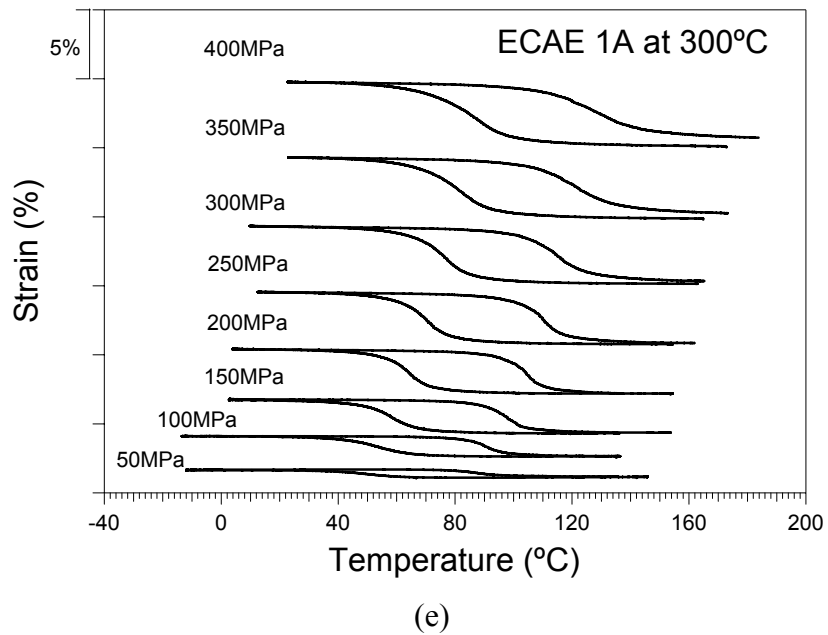
Figure 4.11 Continued
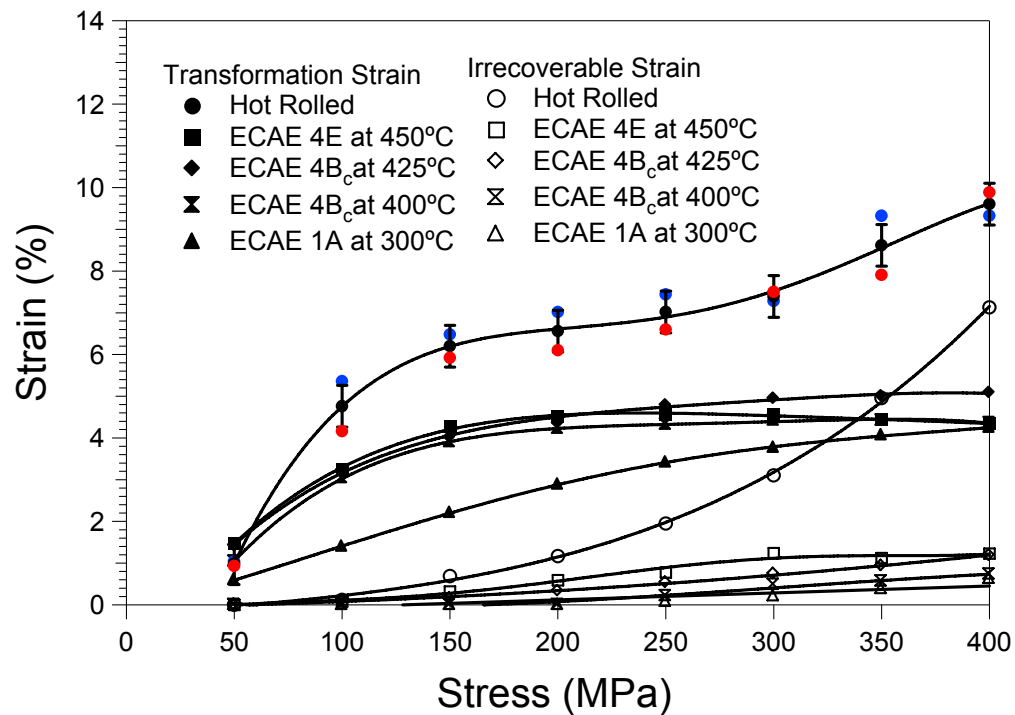
Figure 4.12 Transformation and irrecoverable strain response as a function of constant tensile stress levels in the $Ni_{49.7}Ti_{50.3}$ samples from the isobaric cooling-heating experiments under increasing applied stress levels of Figure 4.5.2.

4.6 Critical Stress vs. Critical Temperature Response for Inelastic Deformation

Thermoelastic martensitic transformation is a combination of mechanical and thermal transformation processes. Thermodynamical conditions have been established to express the effect of stress and temperature as the external driving forces on the martensitic phase transformation [129]. The relationship between stress and temperature to induce martensitic transformation has been expressed using Clausius-Clapeyron equation [124]:

$$\frac{d\sigma}{dT} = -\frac{\Delta H}{T_0 \varepsilon_{tr}}$$
(4.6.1)

ΔH is the enthalpy change of the transforming body, T_0 is the chemical equilibrium temperature of the transformation, and ε_{tr} is the transformation strain of the transformation in the direction of the stress. Basically, the Clausius-Clapeyron equation defines a linear relationship between stress and temperature required to induce martensitic transformation.

To determine the complete stress-temperature relationship for hot rolled sample and the samples ECAE processed at 400°C and 425°C for four passes at three different deformation modes which were defined in Chapter II and redefined in Figure 4.13.a, three types of tests were conducted which are:

1)   Isothermal loading-unloading experiments in martensite phase to find the critical stress for martensite reorientation. Critical stress for martensite reorientation was measured at 0.2% offset strain using the apparent elastic modulus of martensite on the stress vs. strain curves.

2)   Isobaric thermal cyclic experiments to find the critical temperature for the onset of martensitic transformation.

3)   Isothermal loading-unloading experiments in austenite phase to find plastic yield point of austenite. The critical stress for plastic deformation of austenite was measured at 0.2% offset strain from the apparent elastic modulus of austenite on the stress vs. strain curves.

Figure 4.13.a shows three separate regions of stress vs. temperature relationships

which are for martensite reorientation, stress induced martensitic transformation and plastic yielding of austenite for the hot rolled sample and the samples ECAE processed at 400°C and 425°C. Then, stress vs. temperature curves in Figure 4.13.b are constructed for martensitic reorientation and stress induced martensitic transformation and the slopes of these curves are determined for three samples. In each region, the stress vs temperature relationship is clearly different. Martensitic reorientation and plastic deformation of austenite show an expected temperature dependence with a negative slope, however, the critical stress for stress induced-martensitic transformation is highly dependant on temperature according the Clausius-Clapeyron equation with a positive slope. σ_y for austenite, i.e. Region II and Region III intercept at stress levels of 550MPa, 750MPa and 850MPa for the hot rolled sample, ECAE processed samples at 425°C and 400°C, respectively. To better observe Region II behavior and the intersection with Region I a magnified version of Figure 4.13.a is represented in Figure 4.13.b. Region I and Region II intercept at stress levels of 110MPa, 100MPa and 80MPa for the hot rolled sample, ECAE processed samples at 425°C and 400°C, respectively. The critical stresses for the stress induced martensitic transformations of samples ECAE processed at 400°C and 425°C and hot rolled samples showed a linear dependence on testing temperature with the dσ/dT values of, 9.4MPa/°C, 8.1MPa/°C and 7.5MPa/°C, respectively.

Comparing the stress vs. temperature relationship at low stress level, there is an obvious difference between ECAE processed and hot rolled sample responses in Figure 4.13.a. Extrapolating the Region II response of the hot rolled sample in Figure 4.13.b gives the temperature of 56°C at zero stress which is 16°C below the M_s temperature detected using DSC ($M_s^{\sigma=0}$). Similarly, the M_s temperatures under 50 and 100MPa determined from isobaric cooling/heating experiments are found to be the same as the $M_s^{\sigma=0}$, i.e. 72°C. On the other hand, extrapolating Region II response of the ECAE processed samples results approximately 4-5°C higher M_s temperatures than that of the M_s temperatures of ECAE processed samples measured using DSC as shown in Figure 4.13.b. The implications of this response and possible rationale for such differences will

be discussed in section 4.8 in detail considering the role of R-phase, the effect of grain size and martensite twin type and morphology.
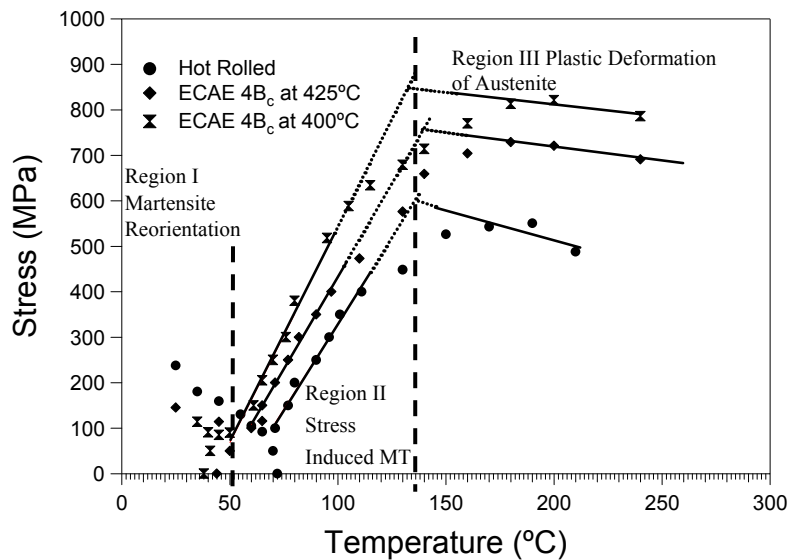
(a)
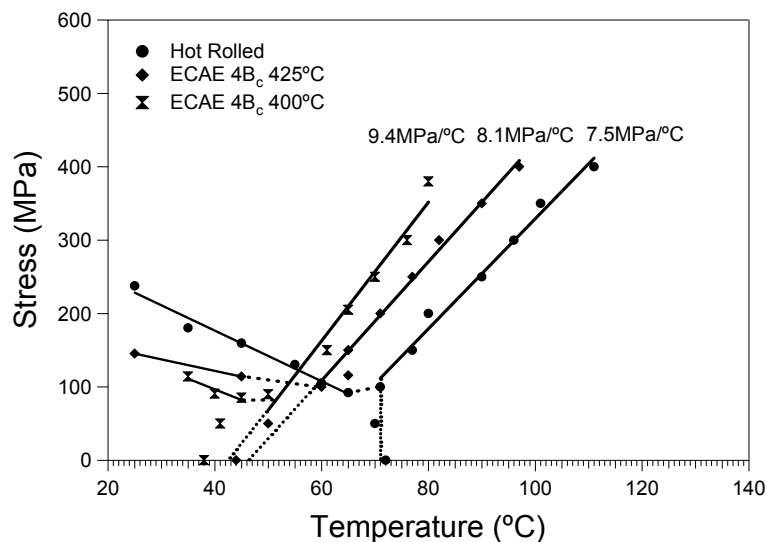
(b)

Figure 4.13 Effect of temperature on the critical stress for martensitic reorientation, stress-induced martensitic transformation and plastic yielding of austenite of ECAE processed and hot rolled samples.

4.7 Thermal Cyclic Experiments under Constant Stress

As shown in section 4.5, none of the samples demonstrated irrecoverable strain at and below 50MPa, however, the samples extruded at 400°C and 300°C show no irrecoverable strain up to 150MPa. Thus 50MPa and 150MPa were chosen as two stress levels for thermal cyclic experiments. The main purpose to conduct cyclic tests was to evaluate the transformation and the irrecoverable strain levels as a function of the number of cycles. Figures 4.14 and 4.15 represent the cyclic strain temperature response of the ECAE processed and hot rolled samples under these stress levels, respectively, for ten cycles.
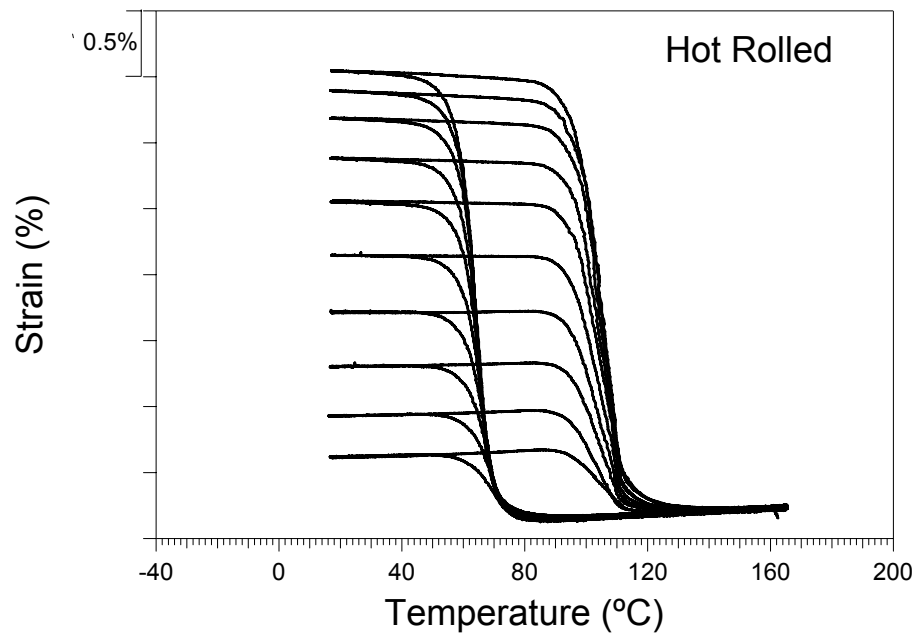
(a)

Figure 4.14 Strain vs. temperature response of the $Ni_{49.3}Ti_{50.7}$ alloy under 50MPa. (a) Hot rolled, (b) ECAE 4E at 450°C, (c) ECAE $4B_c$ at 425°C, (d) ECAE $4B_c$ at 400°C, (e) ECAE 1A at 300°C samples.
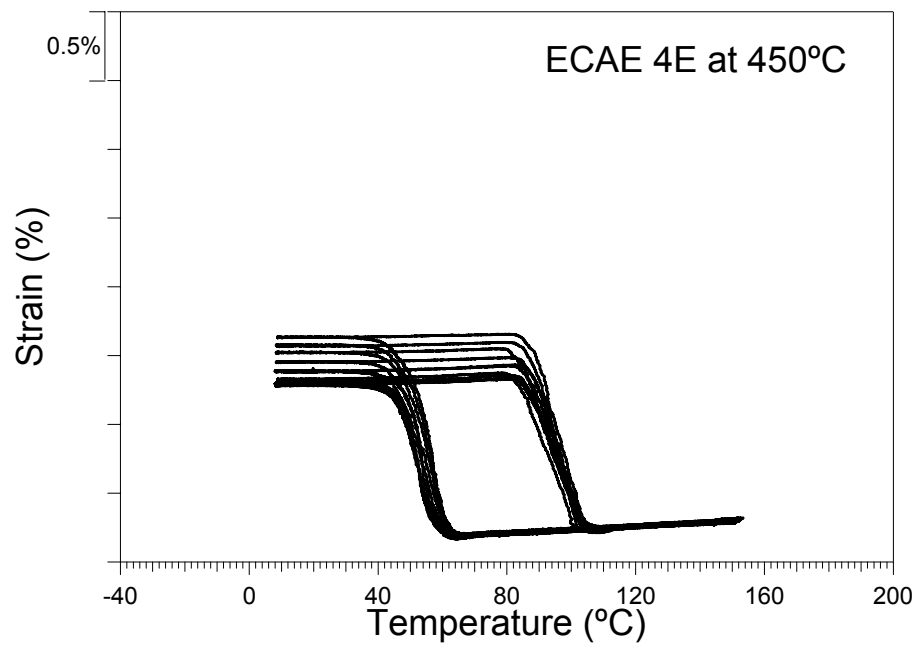
(b)
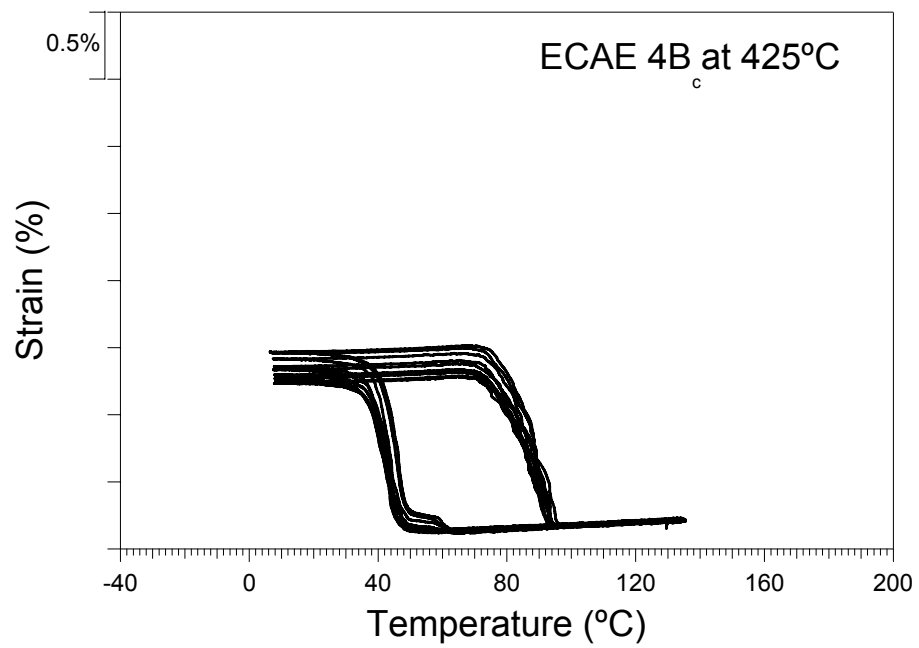
(c)

Figure 4.14 Continued
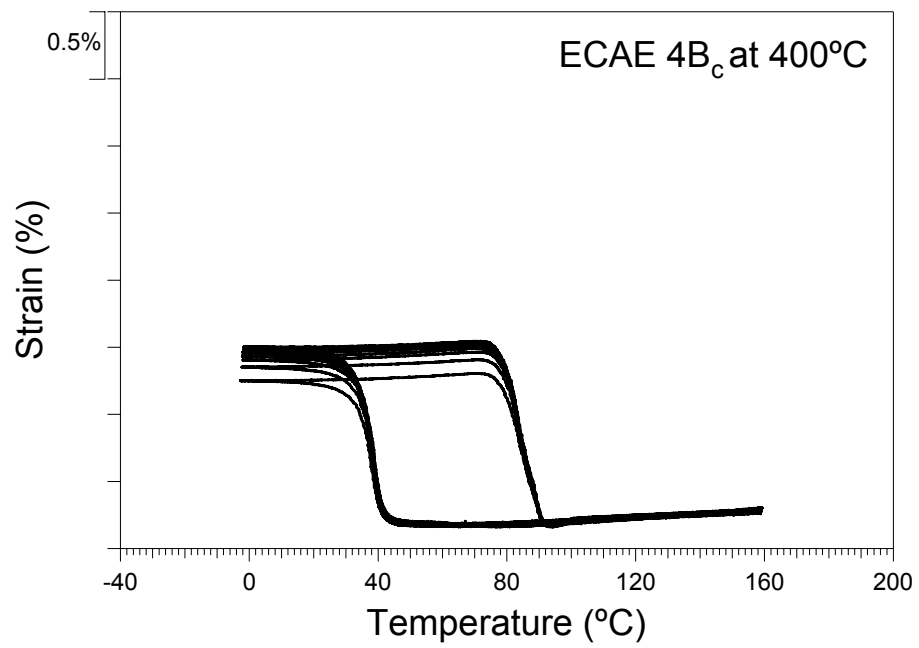
(d)
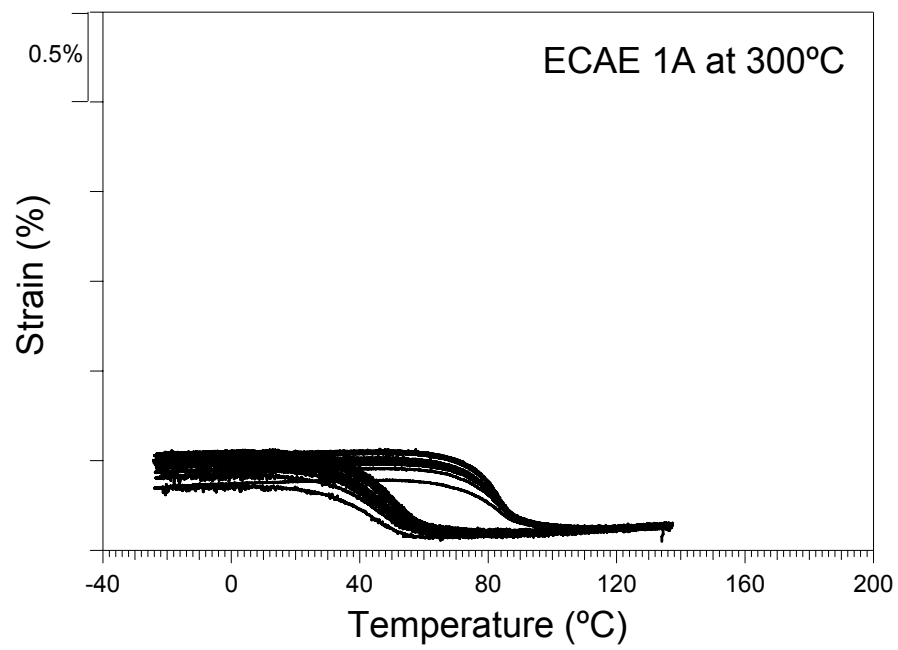
(e)

Figure 4.14 Continued
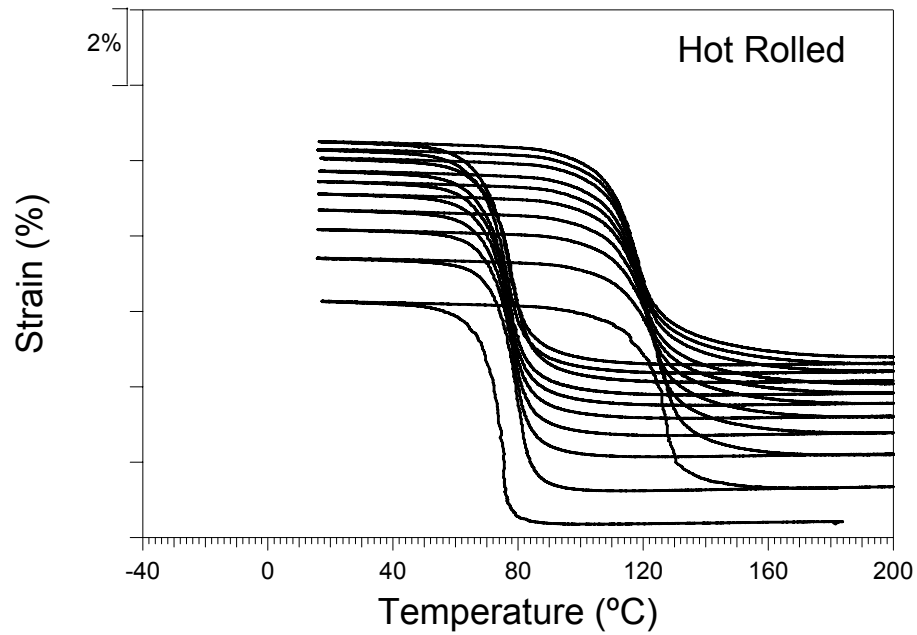
(a)
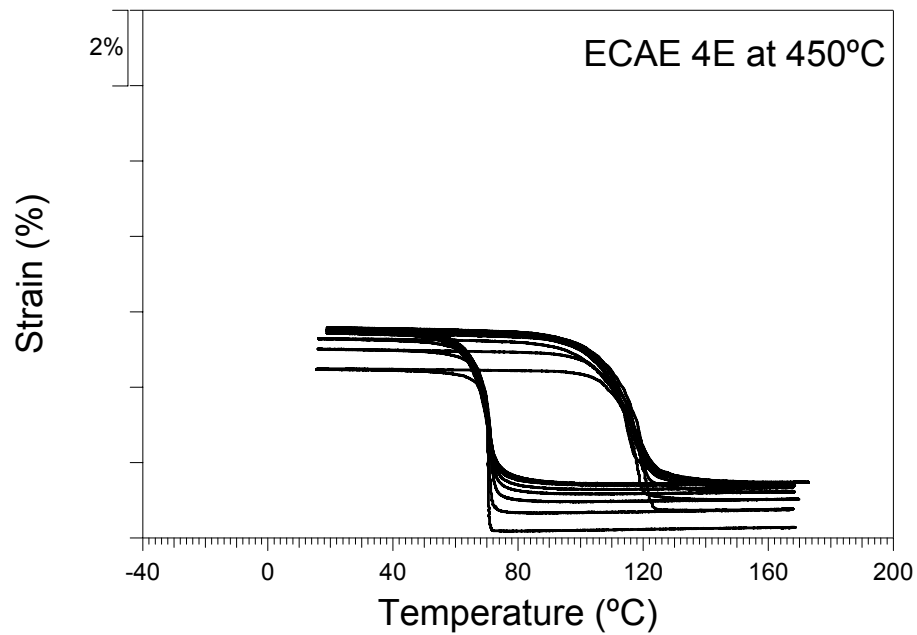
(b)

Figure 4.15 Strain vs. temperature response of the $Ni_{49.3}Ti_{50.7}$ alloy under 150MPa. (a) Hot rolled, (b) ECAE 4E at 450°C, (c) ECAE $4B_c$ at 425°C, (d) ECAE $4B_c$ at 400°C, (e) ECAE 1A at 300°C samples.
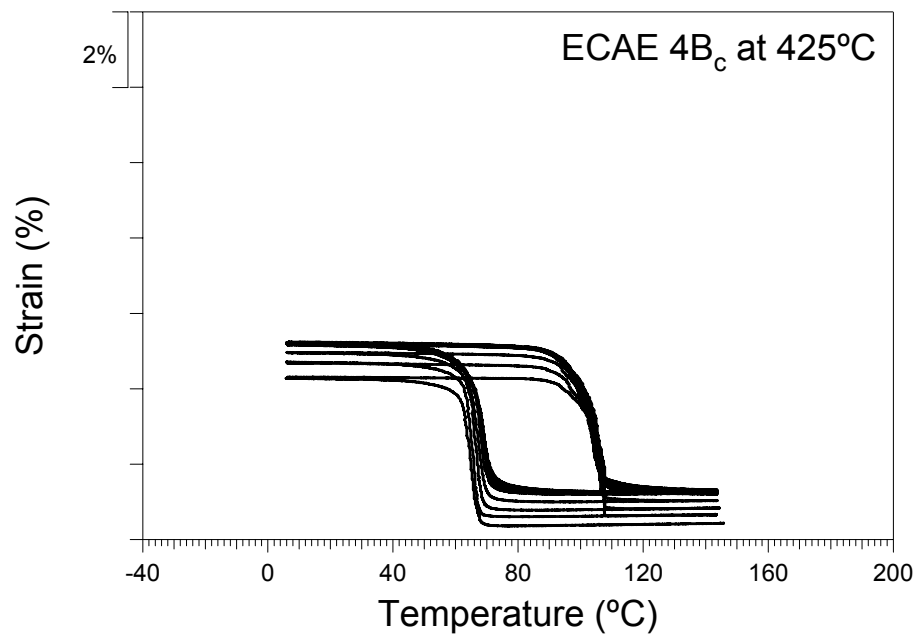
(c)
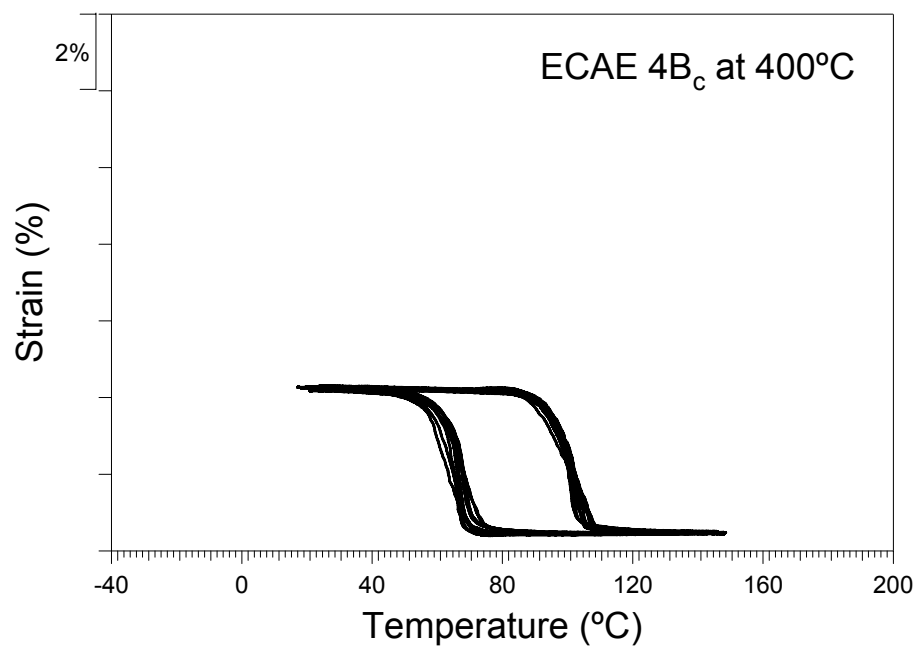
(d)

Figure 4.15 Continued

(e)
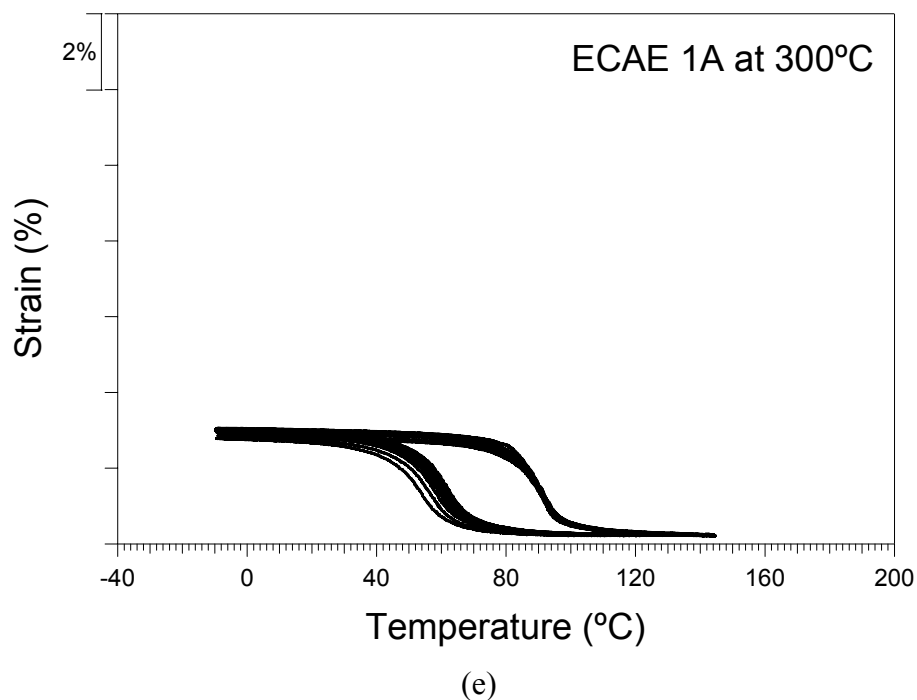
Figure 4.15 Continued

The main observation from Figure 4.14 and 4.15 is the considerable improvement in the cyclic stability after ECAE process.

The evolution of transformation strain under 50MPa and 150MPa and irrecoverable strain levels under 150MPa as a function of the number of cycles is given in Figures 4.16 and 4.17, respectively. As expected from isobaric heating-cooling experiments, none of the samples show irrecoverable strain under 50MPa. Under 150MPa, the samples which are ECAE processed at 400°C and 300°C show no irrecoverable strain respectively and irrecoverable strain levels of the other ECAE processed samples are much lower than that of the hot rolled sample. In all samples, the irrecoverable strain decreases with the number of cycles and seems to saturate in the last few cycles. In the samples ECAE processed at 425°C and 450°C, the irrecoverable strain values decreases down to 0% after 5th and 8th cycles, respectively, however, certain level of irrecoverable strain is measured in the hot rolled sample even at 10th cycle. Another observation from the strain vs. temperature graphs is the improved cyclic stability of the

transformation strain levels with ECAE, which enhances further with decreasing ECAE temperature. The transformation strain levels of the samples ECAE processed at 450°C, 425°C and 400°C under 50MPa are around 1.3% and ECAE processed at 300°C under 50MPa is 0.5%. There is almost no change in the transformation levels of ECAE processed samples with the number of cycles, however the transformation strain level of the hot rolled sample is initially 0.6% and continuously increases and becomes 3.4% after 10 cycles. Under 150MPa, the transformation strain levels of ECAE processed samples are lower than that of the hot rolled sample. These levels for the samples ECAE processed at 450°C, 425°C, 400°C and 300°C are approximately 4%, 3.9%, 3.5% and 2.5% respectively at the 1st cycle and none of these samples show distinctive transformation strain level change after 10 cycles. The transformation strain level of the hot rolled sample is approximately 6% at the 1st cycle and decreases down to 5.8% after 10th cycle.

The main observations for the thermal cycling under constant stress levels are: 1) the transformation and irrecoverable strain levels of ECAE processed samples are lower than that of the hot rolled sample, 2) the transformation strain level decreases with the decrease in ECAE temperature under 150MPa, 3) the transformation strain levels of ECAE processed samples are stable with the number of cycles, 4) No irrecoverable strain is evident in the sample ECAE processed at 400°C under 150MPa, and 5) the irrecoverable strain levels of other ECAE processed samples seem to saturate at 0% after few number of cycles.

Another intriguing observation from cyclic experiments under 50MPa and 150MPa is the decrease in thermal hysteresis of the ECAE processed samples with the increase in applied stress as shown in Figure 4.18. Under 50MPa, the hysteresis of the hot rolled sample vary between 35°C and 40°C, first slightly decreasing and then increasing with the number of cycles. Under 150MPa, the hot rolled sample experiences a decrease in ΔT with the number of cycles from 52°C to 42°C. On the other hand, under 50MPa, the hysteresis of the sample ECAE processed at 400°C is about 42°C and does not change notably with the number of cycles, More surprisingly, under 150MPa,

thermal hysteresis is 39°C at the first cycle and drops down to 32°C after ten cycles of cooling-heating. In other words, in the hot rolled sample, increasing stress level increases thermal hysteresis while the opposite is observed in the ECAE processed sample. Note that, thermal hysteresis is an indication of how much dislocation occurs in the material during the forward and reverse phase transformation.
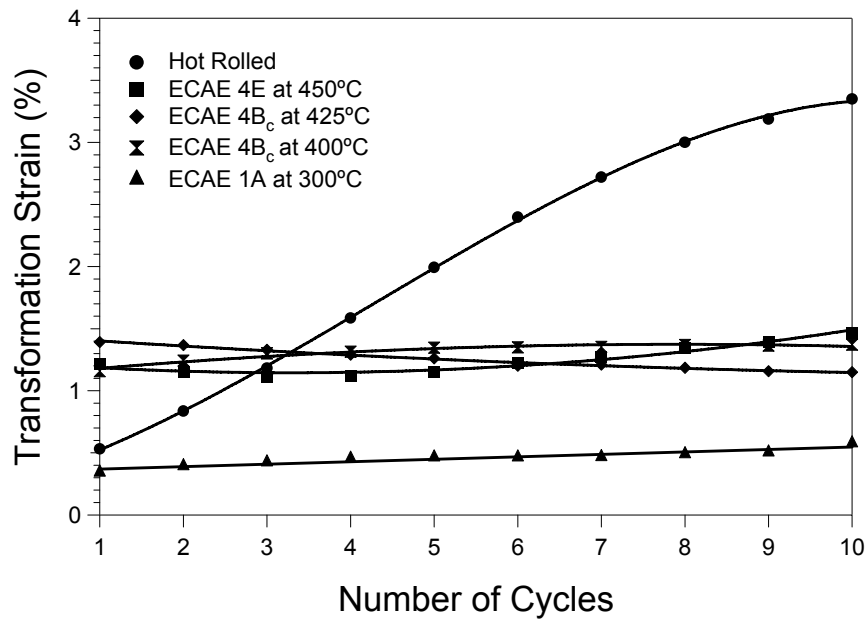
(a)

Figure 4.16 Transformation strain evolution of the hot rolled and ECAE processed Ni$_{49.3}$Ti$_{50.7}$ samples with the number of cycles under (a) 50MPa and (b) 150MPa.
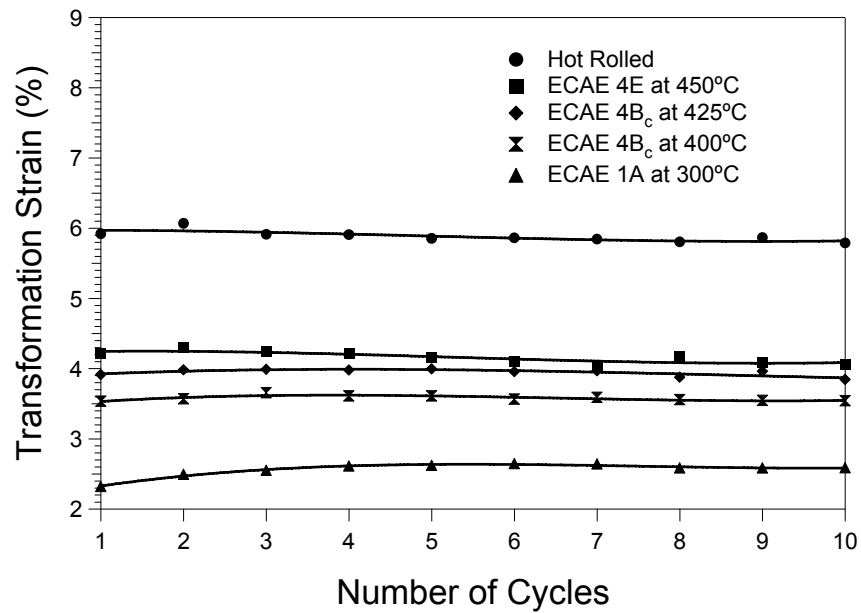
(b)

Figure 4.16 Continued
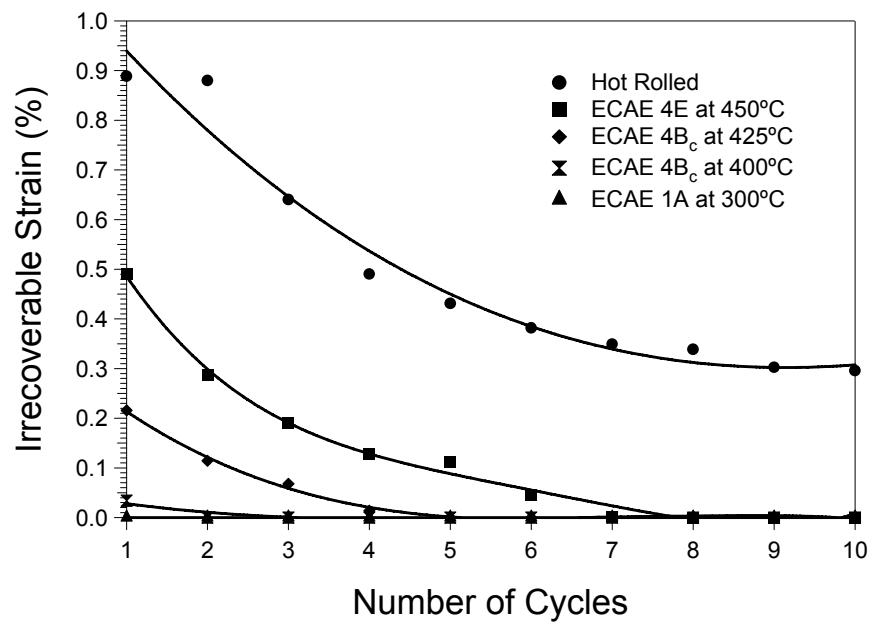
Figure 4.17 Irrecoverable strain evolution of the hot rolled and ECAE processed $Ni_{49.3}Ti_{50.7}$ samples with the number of cycles under 150MPa.
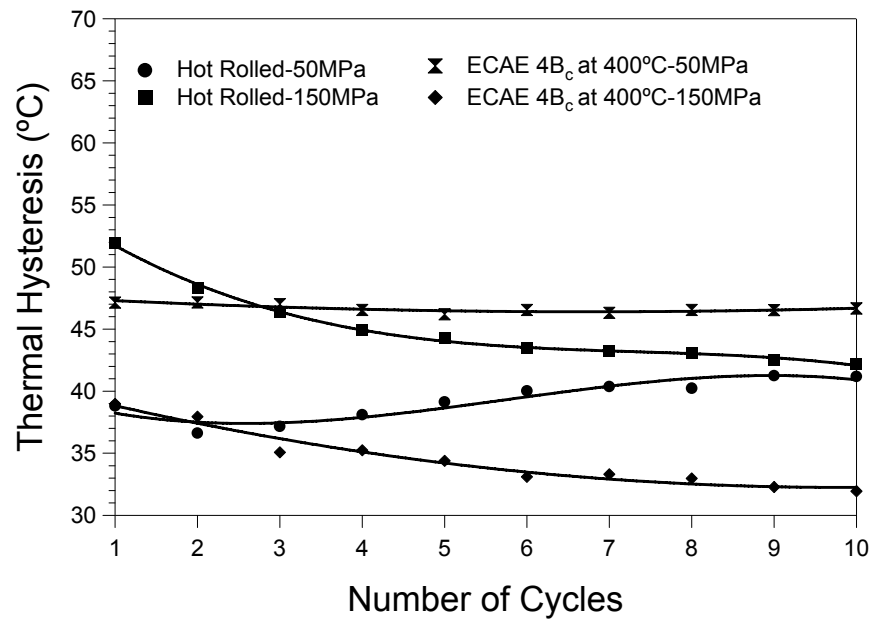
Figure 4.18 Thermal hysteresis comparison of the sample ECAE processed at 400°C and the hot rolled sample under 50MPa and 150MPa.

4.8 Discussion of the Results

In this part of work, the main goal was to reveal the effect of severe plastic deformation via ECAE and associated microstructural refinement on the thermo-mechanical cyclic stability of $Ni_{49.3}Ti_{50.7}$. The main observations could be summarized as:

1) The transformation temperatures decrease after ECAE process, however, the effect of ECAE is less pronounced in the sample ECAE processed at 300°C for 1 pass.

2) The thermal hysteresis of the samples ECAE processed for four passes are larger than that of hot rolled sample and the sample ECAE processed at 300°C for one pass. The transformation temperature interval (M_f-M_s) is low in the samples ECAE processed for four passes while the hot rolled sample and the sample ECAE processed for one pass have higher transformation temperature interval.

3) The grain sizes of the samples ECAE processed for four passes at 450°C,

425°C and 400°C were determined to be on the order of 100 to 300nm. Microstructural refinement in the sample ECAE processed at 300°C is achieved via deformation twinning-induced refinement.

4)   The twin mode in martensite was found to be a mixture of Type I and Type II twins in addition to the (001) compound twins in the samples ECAE processed for four passes.

5)   Austenite to R-phase transformation is observed in ECAE processed samples for four passes.

6)   ECAE led to an increase in the strength differential between the critical stress to induce martensite and the yield stress of martensite. Such increase was thought to be responsible for the significant improvement in the thermal cyclic stability and reduction in the irrecoverable strain levels under constant stresses. The negligible irrecoverable strain levels under very high stress levels observed in the samples ECAE processed at 400°C and 300°C is attributed to the increase in critical stress level for dislocation slip due to grain size and deformation twinning-induced refinement via ECAE.

The rationale and mechanisms responsible for these main observations are discussed below in detail.

4.8.1 Grain Size, Twin Formation and Microstructural Evolution during ECAE

Figure 4.3 shows both the grain size refinement and well-delineated grain boundaries which can be attributed to the dynamic recovery and recrystallization during ECAE at 400°C and above from the contrast changes across the grain boundaries, it can be deduced that the volume fraction of high angle grain boundaries is relatively large. The microstructural evolution in the sample ECAE processed at 300°C does not feature delineated grain boundaries due to the high volume fraction of deformation twins. The microstructural refinement in the samples ECAE processed at 400°C, 425°C and 450°C is achieved through grain refinement. The mechanism of grain refinement is the continuous dynamic recovery/recrystallization. Severe plastic deformation at slightly

high temperatures causes the development of new grains as a result of gradual increase in the misorientations between the subgrains. Further deformation reduces the grain size continuously and the volume fraction of newly generated ultrafine grains increases.

Figure 4.6 shows the $(1\bar{3}1)$ deformation twins in the austenite. There is a high volume fraction of deformation twins with a twin size of 20nm, thus, microstructural refinement in the sample ECAE processed at 300°C is achieved via deformation twinning-induced refinement. Deformation twinning in B2 nanograins instead of Type I and Type II twinning modes was also observed in severely plastically deformed NiTi alloys due to high strength and shear stress applied during room temperature deformation [125].

TEM images and diffraction patterns in Figure 4.4 showed that grain size refinement suppresses the formation of martensite due to the increase in energy barrier. Grain boundaries act as obstacles such that martensite plate nucleated within the grain is stopped at the boundary. To initiate the nucleation and growth of martensite in the next grain the martensite plates in the neighboring grain should induce some stress which could be a result of the mismatch between transformed and untransformed grains. However, according to Waitz et al. [25] grains that have sizes less than 60nm, the stresses are not enough to initiate martensite nucleation in the adjacent grain and the dislocations in each grain suppress the martensite nucleation and growth.

The grain size of B2 austenite phase affects the twinning mode and the size of the twin plates of B19' martensite in $Ni_{49.7}Ti_{50.3}$ alloys. In the refined grains of the samples ECAE processed for four passes, (001) compound twins are found in addition to common $<011>$ Type II and $\{11\bar{1}\}$ Type I twins. (001) compound twinning with fine platelet is selected as a internal defect of the matensite to minimize the transformation strain in nanograins, although (001) compound does not give solution to crystallographic theory [26, 123, 126]. The constraints of the grain boundaries facilitates the self accommodation of the martensite with selection of (001) compound twin formation as an energy minimizing transformation path. The morphological difference

between (001) compound, $<011>$ Type II and $\{11\bar{1}\}$ Type I twinning is in the twin plate width. The width of (001) compound twin platelets which show "herring-bone morphology is 2-3nm while the width of the twin platelets of Type I and Type II twins is 20-30nm.

4.8.2 Effect of ECAE and Grain Refinement on Martensitic Transformation Temperatures

In a thermoelastic martensitic transformation, there is a thermodynamic equilibrium between chemical and non-chemical energies which can be expressed as, for the forward and reverse transformation, respectively:

$$\Delta G = \Delta H - T\Delta S + \Delta E_e + \Delta E_{irr} \qquad (4.8.2.1)$$

ΔG, ΔH, ΔS, ΔE_e and ΔE_{irr} are the free energy, enthalpy, entropy, elastic free energy and irreversible energy changes upon phase transformation, respectively. In order to rationalize the isobaric cooling heating or cyclic under constant stress experiment results, it is necessary to consider the thermodynamic factors which control the martensitic transformations. The total free energy change in equation 4.8.2.1 is comprised of three contributions: the change in chemical free energy which is $\Delta H - T\Delta S$, the change in strain energy ΔE_e associated with the transformation induced elastic stresses and irreversible energy ΔE_{irr} needed to propagate the transforming interface. The chemical energy is not expected to change because the structure and the order of the parent and martensite phase remain unaltered. Therefore, the change in total free energy can be associated with the change in elastic strain energy and the irreversible energy. The change in elastic strain energy can be expressed as for a tensile loading [126]:

$$\Delta E_e^{p \to m} = -\sigma \varepsilon^t / \rho + \Delta E_{eo}^{p \to m} \qquad (4.8.2.2)$$

Here σ is the applied tensile stress and ε^t is the transformation strain. $\Delta E_{eo}^{p \to m}$ is the summation of ΔE_e^t and ΔE_e^d. ΔE_e^t and ΔE_e^d are transformation induced elastic

strain energy and elastic strain energy associated with the local stress field at defects. p→m represents the parent to martensite transformation.

For a single stage martensitic transformation the transformation temperatures of parent to martensite and the back transformations can be expressed as [126]:

$$T_{p \to m} = T_0 + (\Delta E_e^{p \to m} + \Delta E_{irr}^{p \to m})/\Delta S \qquad (4.8.2.3)$$

$$T_{m \to p} = T_0 + (\Delta E_e^{p \to m} - \Delta E_{irr}^{p \to m})/\Delta S \qquad (4.8.2.4)$$

Substituting equation 4.8.2.2 in 4.8.2.3 gives:

$$\Delta E_{e0}^{p \to m} = (T_{p \to m} - T_0)\Delta S + \sigma \varepsilon^t/\rho - \Delta E_{irr}^{p \to m} \qquad \text{.......(4.8.2.5)}$$

The irreversible energy which depends on the thermal hysteresis of the transformation can be determined using equations 4.8.2.2, 4.8.2.3 and 4.8.2.4 as [126]:

$$\Delta E_{irr}^{p \to m} = \Delta S(T_{p \to m} - T_{m \to p})/2 \qquad (4.8.2.6)$$

ΔS can be evaluated from the stress dependence of the transformation temperature via Clausius-Clapeyron equation obtained by differentiating equations 4.8.2.3 or 4.8.2.4.

$$\Delta S = -(d\sigma/dT)/(\varepsilon^t/\rho) \qquad (4.8.2.7)$$

The changes in the elastic and the irreversible energies under zero stress and 150MPa are calculated for hot rolled $Ni_{49.7}Ti_{50.3}$ and the $Ni_{49.7}Ti_{50.3}$ samples ECAE processed at 425°C and 400°C and tabulated in Table 4.3. The density of $Ni_{49.7}Ti_{50.3}$ which is represented as ρ in equation 4.8.2.7 is 6.5g/mm^{-3}. T_0 which is the equilibrium temperature is calculated from the equation in 4.8.2.8 as 100°C for the hot rolled case and should be unaltered after ECAE and applied stress because T_0 is only composition dependent.

$$T_0 = \frac{M_s + A_f}{2} \qquad (4.8.2.8)$$

Table 4.3 The changes in the elastic and irreversible energies under no stress and 150MPa for the $Ni_{49.7}Ti_{50.3}$ samples hot rolled and ECAE processed at 425°C and 400°C.

Material	$\Delta E_{e0}^{p \rightarrow m}$ (no stress) (J/g)	$\Delta E_{irr}^{p \rightarrow m}$ (no stress) (J/g)	$\Delta E_{e0}^{p \rightarrow m}$ (150MPa) (J/g)	$\Delta E_{irr}^{p \rightarrow m}$ (150MPa) (J/g)
Hot Rolled	0.87	0.4	1.41	1.47
ECAE $4B_c$ at 425°C	1.94	0.85	1.82	0.85
ECAE $4B_c$ at 400°C	2.70	1.06	2.49	0.84

From Table 4.1, M_s temperature decreases after ECAE process due to the increase in irreversible and elastic energy according to equation 4.8.2.3. This increase in irreversible energy can be attributed to the increase in strength levels via grain refinement and dislocation density. In such a microstructure multiple phase fronts should be nucleated and propagated which would require more energy (i.e., reduction in the transformation temperature) and more energy dissipation due to both difficulty of propagation of and interaction between multiple phase fronts, but especially due to the later. Grain boundaries and high dislocation density act as barriers to the transforming interfaces and require the nucleation of new phase fronts. Therefore, under no stress, the transformation temperatures decrease while the thermal hystereses increase after ECAE process for four passes. However, note that the increase in thermal hysteresis and the decrease in transformation temperature are only under no stress condition. The thermal hystereses of samples ECAE processed for four passes start to decrease with the increase in applied stress as shown in Figure 4.18 which can be attributed to the decrease in irreversible energy as represented in Table 4.3. The decrease in irreversible energy and the increase in elastic energy are due to the improved compatibility of the transforming interface between the austenite and martensite phases. In ECAE processed samples under no stress, there is a mixture of single variant martensite and self accommodating martensite variants which leads to some dissipation by local plasticity due to variant-variant interaction. The variant-variant interaction becomes less since the volume

fraction of single variant martensite increases which leads to less dissipation thus smaller thermal hysteresis [128]. In hot rolled sample, the increase in thermal hysteresis with the increase in applied stress originates from the partial accommodation of martensitic transformation with dislocations instead of twins. When the stress level increases dislocation formation becomes easy and thermal hysteresis increases.

One important indication of the improvement in cyclic stability is to compare the variation in thermal hystereses of ECAE processed and hot rolled samples under 50MPa and 150MPa. It is clearly seen in Figures 4.14 and 4.15, thermal hysteresis of ECAE processed samples during 10 cycles are very stable due to the less defect generation with cycles in ECAE processed samples.

Another observation from the DSC experiments and isobaric cooling-heating experiments is the decrease in transformation temperature interval (i.e. M_s-M_f) and increase in the thermal hysteresis in the samples ECAE processed for four passes. The transformation temperature interval elucidates the stored elastic energy during the phase transformation. When the stored elastic energy is high the slope of the cooling curve in isobaric cooling-heating experiment is shallow (i.e. M_s-M_f is high) whereas when the stored elastic energy is low the slope of the cooling curve is steep (i.e. M_s-M_f is low). Thus, the stored elastic energy during the phase transformation in the samples ECAE processed for four times is low, while the samples ECAE processed for one pass shows higher stored elastic energy during phase transformation. One of the reasons of observing low stored elastic energy is the dissipation of stored elastic energy during phase front motion. Increasing energy dissipation leads to higher thermal hysteresis. Thus, if the stored elastic strain energy is higher, the heating necessary to initiate reverse transformation is lower and thermal hysteresis will be lower as in the sample ECAE processed for one pass at 300°C. Therefore, there is an inverse relationship between the thermal hysteresis and the transformation temperature interval. The increase in dissipation energy during phase front motion in samples ECAE processed for four passes can be attributed to the grain refinement. Grain boundaries act as barriers to the transforming interfaces which require more energy. On the other hand, formation of

refined microstructure due to very fine deformation twins in the sample ECAE processed for one pass may help suppressing energy dissipation. Deformation twins in austenite or compound twins in martensite are shown to transform into twin boundaries in martensite or vice versa [20, 129]. Therefore, these twin boundaries in the sample ECAE processed at 300°C do not affect the elastic energy storage and the energy required for the phase transformation as much as a grain boundary or dislocation cell walls do.

4.8.3 Effect of ECAE on Monotonic Response under Tension

The increase in yield strength of martensite (σ_y) and the increase in the stress differential between yield strength and critical stress to induce martensitic transformation ($\sigma_y - \sigma_{SIM}$) after ECAE process can be attributed to the microstructural refinement (grain refinement and deformation induced twinning refinement) and hardening due to high dislocation density. σ_y, σ_{SIM}, and $\sigma_y - \sigma_{SIM}$ levels of all samples determined from Figure 4.9 are tabulated in Table 4.4.1.

There is a decrease in the critical stress to induce martensitic transformation in the samples ECAE processed for four passes and an increase in that of the sample ECAE processed at 300°C for one pass. The critical stress to induce martensitic transformation levels measured from the isothermal monotonic experiments are in good agreement with the critical stress levels found in Region II of stress vs. temperature curves in Figure 4.13.b.

There are few possible mechanisms responsible for the reduction in σ_{SIM} after ECAE for four passes as compared to that of hot rolled sample. These include: 1) small internal local stresses which may exist in the ECAE processed samples and help externally applied stress in triggering martensitic transformation; 2) R-phase transformation prior to martensitic transformation making martensitic transformation relatively easier via reducing the direct incompatibility between martensite and austenite, and the need for an accommodation mechanism which would increase the stress level required to continue transformation; 3) more significant elastic modulus mismatch

between austenite and martensite near M_s due to lattice softening in austenite near M_s leading to more severe incompatibility and thus, more dissipation, and higher stress levels for the continuation of transformation in the hot rolled case; and 4) the change in martensite twinning mode with the grain size in the ECAE processed samples and the lower nucleation strain energy and interfacial energy needs of (001) compound twins as compared to Type I and Type II transformation twins. On the other hand, the sample, ECAE processed for one pass at 300°C does not show a similar reduction in σ_{SIM} because, firstly, of the absence of R-phase transformation prior to martensite. Secondly, due probably to significant difference between 1A 300°C sample and other four pass ECAE processed samples, the internal local stress may oppose the externally applied tension. And finally, the martensite twin type might be different than (001) compound twins in the 1A 300°C sample, even though the microstructure of martensite in this sample was not studied. Note that the aforementioned possibilities can also shed some light onto the differences between the critical stress vs. critical temperature responses of the ECAE processed samples and the hot rolled sample at low stress ranges as shown in Figure 4.13.b and this will be elaborated on the following section.

4.8.4 Effect of ECAE on Cyclic Stability and Critical Stress vs. Critical Temperature Behavior

In this section the variation in the transformation and irrecoverable strain levels of ECAE processed and hot rolled samples in the isobaric cooling/heating experiments and thermal cyclic experiments under 50MPa and 150MPa, and mechanisms responsible for the improvement in the cyclic stability after ECAE will be introduced. Peculiarities in the critical stress vs. critical temperature response of the ECAE processed and hot rolled samples part of which can be expressed using Clausius-Clapeyron equation will be scrutinized in detail.

The consequence of observing notably lower transformation strain levels in ECAE processed samples than that of the hot rolled sample under 50MPa and 150MPa is the increase in slope of the critical stress vs. critical temperature curves of ECAE

processed samples in Region II shown in Figure 4.13.b. According to Clausius-Clapeyron equation introduced in section 4.6, transformation strain is inversely proportional to the slope of the curve in Region II. There are few possible reasons for the decrease in the transformation strain and increase in slope after ECAE.

First of all, it is observed that, in the very fine and nano grains, only R-phase exists. R-phase to martensite transformation leads to observe less transformation strain than that of B2 to martensite transformation. Secondly, due to very fine and nano grains, and considering the large elastic mismatch across the grain boundaries of the nanograins, it is likely to have regions near grain boundaries which are untransformed or with self accommodated martensite morphology limiting the overall transformation strain.

In the isobaric thermal cyclic experiment, the transformation of the hot rolled sample under 150MPa is 6.1% and the slope of the critical stress vs. critical temperature in Region II is 7.5MPa/°C. Using the equation 4.6.1, $\dfrac{\Delta H}{T_0}$ is calculated as

$45.75\,\text{J/cm}^3\,°\text{C}$. Assuming that ECAE has no effect on equilibrium temperature T_0, the transformation strain of the sample ECAE processed at 400°C can be calculated as 4.8% by using the slope 9.4MPa/°C from Figure 4.13.b and $\dfrac{\Delta H}{T_0}$ $45.75\,\text{J/cm}^3\,°\text{C}$. This

calculated transformation strain is higher than the measured strain (i.e. 3.5%) in both isobaric cooling/heating experiment and thermal cyclic experiment under 150MPa. This indicates that ΔH should be smaller. Thus, clearly, there should be some untransformed regions in the ECAE processed samples.

The last reason of observing lower transformation strains in ECAE processed samples can be crystallographic texture in the ECAE processed samples substantially different than that of the hot rolled sample. However, since the ECAE temperatures are high, significant texture evolution would not be expected. In addition, the texture formation after four passes of ECAE in several BCC and FCC materials is shown to be not as strong as in the case of what is usually observed after conventional cold working techniques. Therefore, it is believed that crystallographic texture cannot have a first

order effect in the transformation levels in the present cases. Note that texture measurements are challenging due to the need to measure austenite texture and thus in-situ heating requirement.

In Figure 4.13.b, extrapolating σ_{SIM} curve of the hot rolled sample gives the temperature 56°C which is 16°C below the M_s temperature of the hot rolled sample measured using DSC. Similarly, the M_s temperatures under 50MPa and 100MPa determined from the isobaric cooling/heating experiments are found to be the same as the $M_s^{\sigma=0}$. On the other hand, extrapolating σ_{SIM} curves of the ECAE processed samples gives approximately the same M_s temperatures measured using DSC. This peculiarity between the hot rolled and ECAE processed samples are in accordance with the reduction of the σ_{SIM} levels in the ECAE processed samples as discussed in section 4.8.3, and the similar microstructural factors are thought to be responsible for this observation. The increase in elastic mismatch between austenite and martensite near M_s due to austenite softening and inelastic accommodation of this mismatch in the hot rolled sample lead to the need for higher supercooling or higher stress levels for triggering martensite nucleis to grow in the hot rolled case. This causes austenite to transform into martensite at a lower temperature under a given stress or at a higher stress level under a constant temperature. Similarly, a possible internal local stress, the presence of R-phase, likelihood of more elastic accommodation due to grain size hardening, and transition in the martensite twin type to a lower strain and interfacial energy compound twins make the ECAE processed samples to phase transform earlier and follow the well-known Clausius-Clapeyron equation down to very low stress levels.

In the isobaric thermal cyclic experiments the transformation strains of the ECAE processed and hot rolled samples increase as the level of externally applied stress increase as shown in Figure 4.12. In SMAs, the externally applied stress favors certain variants over the others upon phase transformation [130]. This helps the formation of the martensitic variant with the most favorable orientation (single variant martensite morphology) instead of self accommodation morphology, and thus leads to external shape change. Transformation strain levels depend on the material's ability to form

single variant martensite morphology as opposed to self accommodating transformation structure [13]. The transformation strain level observed in ECAE processed and hot rolled samples is a function of externally applied stress. Note that, the transformation strain level of the hot rolled sample increases continuously due to the fact plastic deformation is induced at higher stress levels. The irrecoverable strain level of the hot rolled sample increases as the externally applied stress increases whereas the increase in the irrecoverable strain levels of ECAE processed samples is very low as shown in Figure 4.12. This could be attributed to the increase in critical shear stress for slip in ECAE processed sample due to microstructural refinement and increase in dislocation density.

The irrecoverable strain levels of ECAE processed samples in thermal cyclic experiments under 150MPa are considerably lower than that of hot rolled sample as shown in Figure 4.17 due to the same reason mentioned above (increase in CSS for slip after ECAE). Although the irrecoverable strain level of the hot rolled sample decreases with the number of cycle and stabilizes after 7th cycle, the irrecoverable strain level is still significant under 150MPa as shown in Figure 4.17. In four pass ECAE processed samples the irrecoverable strain levels diminish to be zero after 4th, 5th and 8th cycles of the samples ECAE processed at 400°C, 425°C and 450°C, respectively. Thermal cycling under constant stress causes a training effect due probably to defect generation, such as dislocations, at the phase front and/or the rearrangement of existing dislocations in both the hot rolled and ECAE processed samples. Note that, no irrecoverable strain is observed under 150MPa in the sample ECAE processed at 300°C.

CHAPTER V

SHAPE MEMORY BEHAVIOR OF THERMO-MECHANICALLY PROCESSED TiNiPd HIGH TEMPERATURE SHAPE MEMORY ALLOYS

5.1 Preamble

The transformation temperatures of NiTi alloys can be increased with the addition of Pd, however, Cai et al. [37] reported that the shape memory behavior of TiNiPd alloys is poor, especially at high temperatures due to the decrease in critical shear stress for dislocation slip. The other problem in TiNiPd high temperature shape memory alloys (HTSMAs) is the deterioration of fracture toughness due to the formation of detrimental precipitates/inclusions. In this chapter, few methods of engineering microstructure including the grain refinement and precipitate fragmentation using ECAE are studied. The thermo-mechanical response of the materials processed via ECAE including transformation strain, irrecoverable strain levels, transformation temperature, thermal hysteresis, enhanced cyclic reversibility and fracture strength are presented and the ramifications of the microstructural evolution on these properties are discussed.

ECAE processing schedules conducted on the $Ti_{50}Ni_{30}Pd_{20}$ and $Ti_{50.3}Ni_{33.7}Pd_{16}$ alloys are recalled for refreshing as: As-cast $Ti_{50}Ni_{30}Pd_{20}$ is solutionized at 1000° for one hour and ECAE processed at 600°C and 400°C for four passes using route C and at 500°C for two passes using route C. $Ti_{50.3}Ni_{33.7}Pd_{16}$ alloy was received in hot-rolled condition. Hot-rolled $Ti_{50.3}Ni_{33.7}Pd_{16}$ alloy was ECAE processed at 450°C for four passes using route B_c and at 400°C for two passes using route B.

5.2 Differential Scanning Calorimetry (DSC) Experiments

Figures 5.1 and 5.2 show the DSC response of the solutionized and ECAE processed $Ti_{50}Ni_{30}Pd_{20}$ samples and hot rolled and ECAE processed $Ti_{50.3}Ni_{33.7}Pd_{16}$

samples, respectively, during five thermal cycles. The transformation temperatures of all samples are highly stable during cycling. Comparing these figures with Figure 4.2 clearly demonstrates the impact of ternary Pd addition on cyclic stability of transformation temperatures. In addition, it can be deduced from Figures 5.1 and 5.2 that ECAE processing does not notably influence the cyclic stability of transformation temperatures of the TiNiPd alloys under no load.

To compare cyclic stability of the transformation temperatures of all TiNiPd samples, M_s temperatures are presented with respect to the number of cycle in Figure 5.3. As expected [30, 31], the transformation temperatures increase as the Pd content increases and the transformation temperatures decrease after ECAE. One intriguing finding is the effect of number of passes on the transformation temperatures of $Ti_{50.3}Ni_{33.7}Pd_{16}$ alloy. The decrease in transformation temperatures of $Ti_{50.3}Ni_{33.7}Pd_{16}$ sample ECAE processed at 450°C and at 400°C is almost the same since the sample ECAE processed at 450°C is processed for four passes.

The transformation thermal hysteresis ($A^* - M^*$) of all TiNiPd samples are presented in Figure 5.4. The thermal hysteresis decreases as the Pd content increases in the unprocessed samples. Note that, unprocessed sample means that ECAE processing is not conducted on the sample. After ECAE the thermal hysteresis increases and as the ECAE temperature decreases the increase in thermal hysteresis is higher.

The main observations from the transformation temperature measurements of TiNiPd alloys can be summarized as: 1) transformation temperatures are very stable before and after ECAE process, 2) transformation temperatures increase as the Pd content increases, 3) they decrease further with ECAE process, 3) thermal hysteresis decreases as the Pd content increases, 4) it increases as the ECAE temperature decreases, 5) the effect of number of ECAE passes is similar to the effect of ECAE temperature on the transformation temperatures.
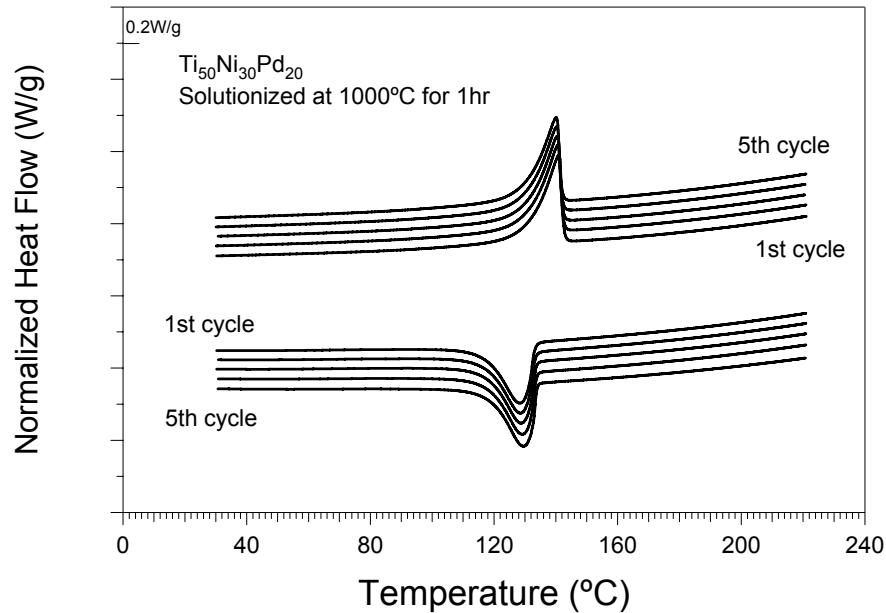
(a)
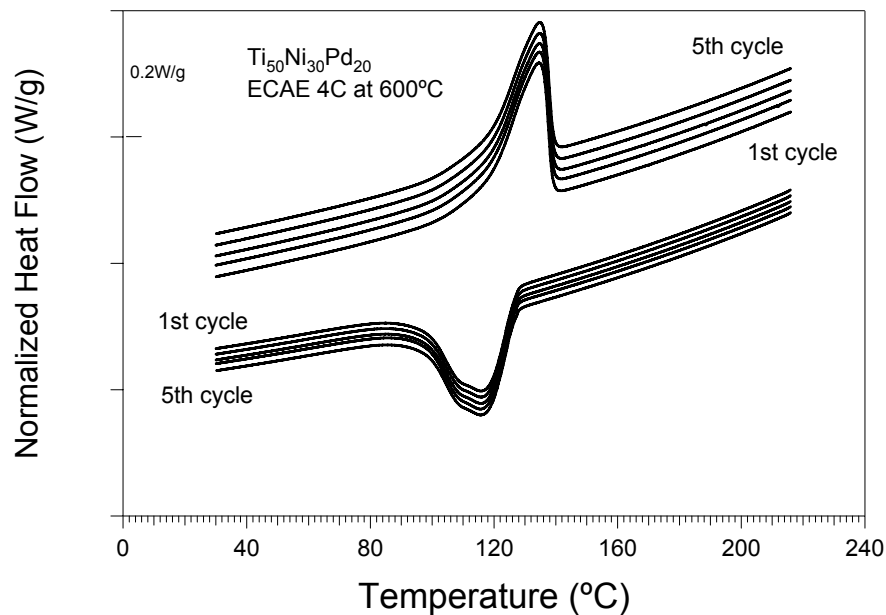
(b)

Figure 5.1 Cyclic DSC response of the solutionized and ECAE processed $Ti_{50}Ni_{30}Pd_{20}$ demonstrating the effect of ECAE processing and ECAE temperatures on the transformation temperatures, (a) solutionized, (b) ECAE 4C at 600°C, (c) ECAE 2C at 500°C, (d) ECAE 4C at 400°C.
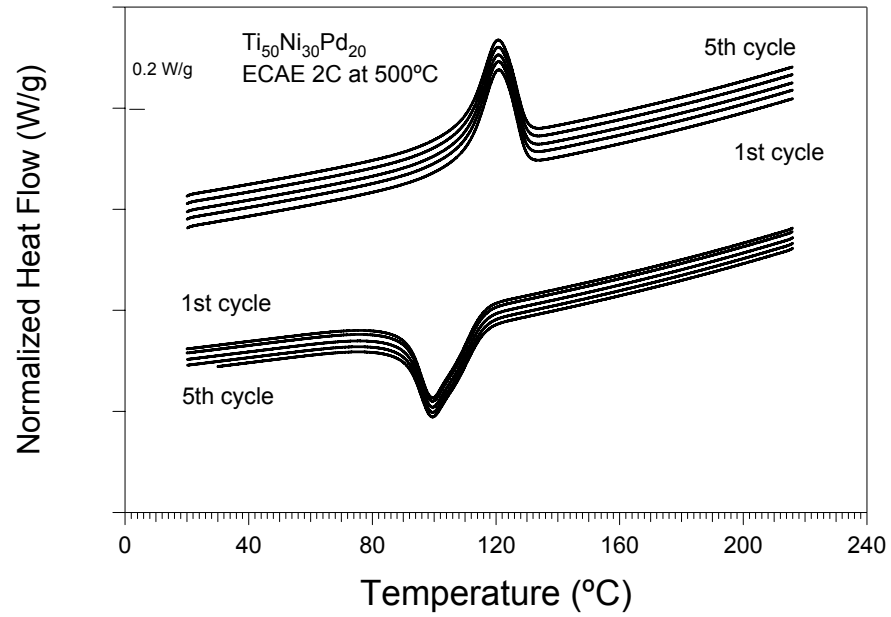
(c)
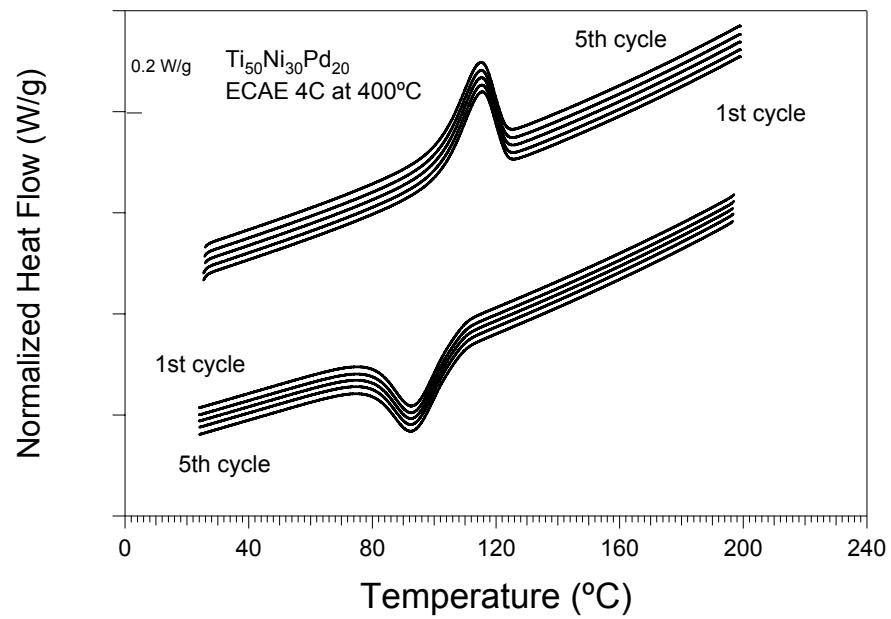
(d)

Figure 5.1 Continued
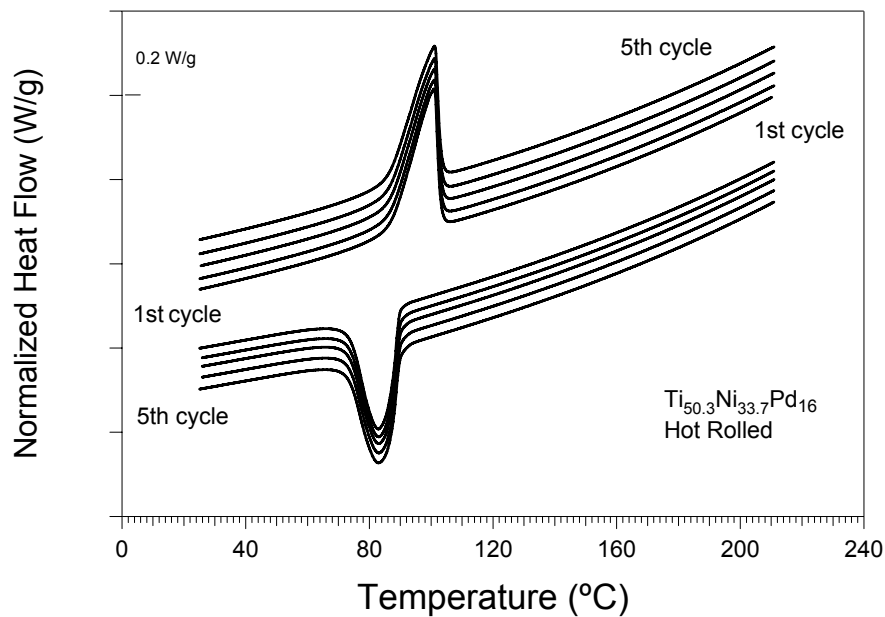
(a)
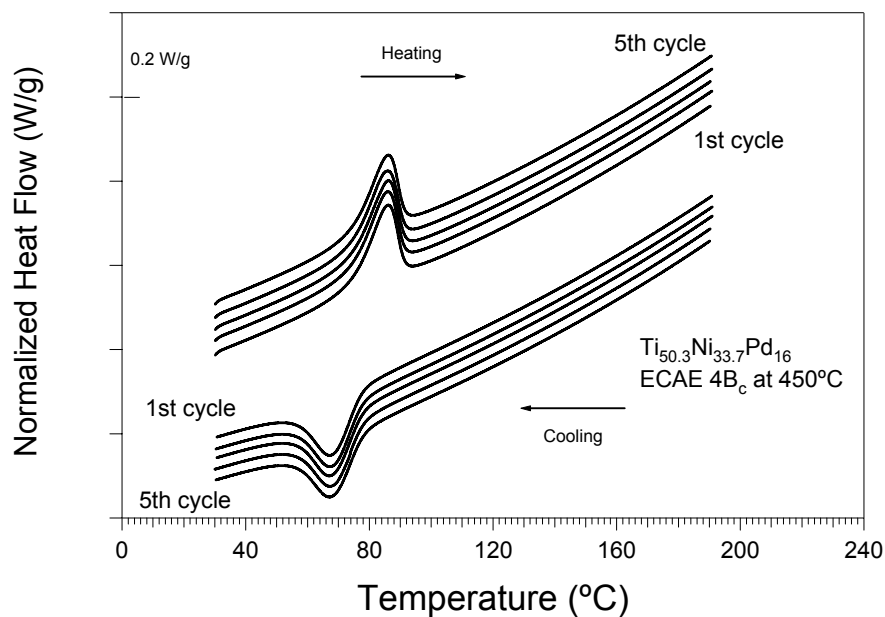
(b)

Figure 5.2 Cyclic DSC response of the hot-rolled and ECAE processed $Ti_{50.3}Ni_{33.7}Pd_{16}$. demonstrating the effect of ECAE processing and ECAE temperatures on the transformation temperatures, (a) Hot-rolled, (b) ECAE $4B_c$ at 450°C, (c) ECAE 2B at 400°C.
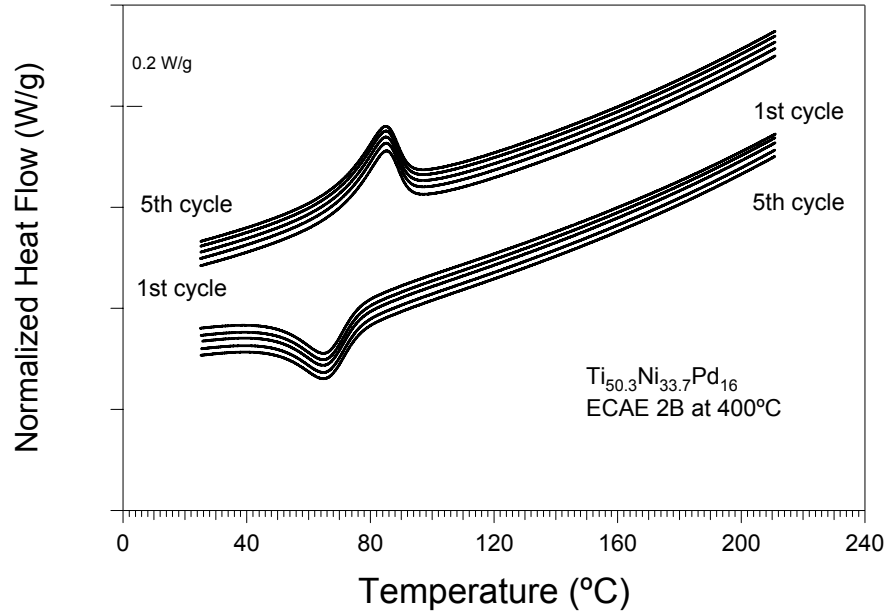
(c)

Figure 5.2 Continued
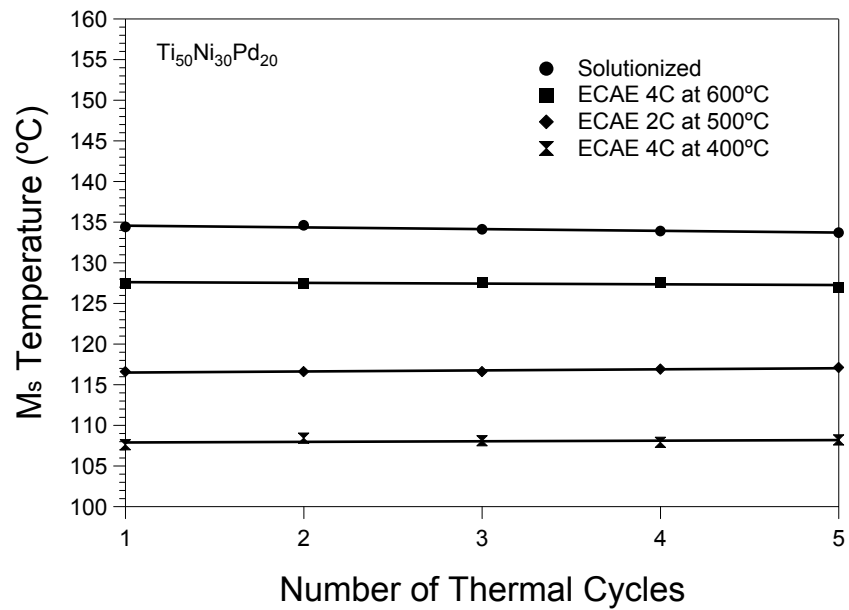
(a)

Figure 5.3 M_s temperatures of all TiNiPd samples extracted from the DSC data showing the effect of ECAE processing, ECAE temperature and Pd content (a) $Ti_{50}Ni_{30}Pd_{20}$, (b) $Ti_{50.3}Ni_{33.7}Pd_{16}$.
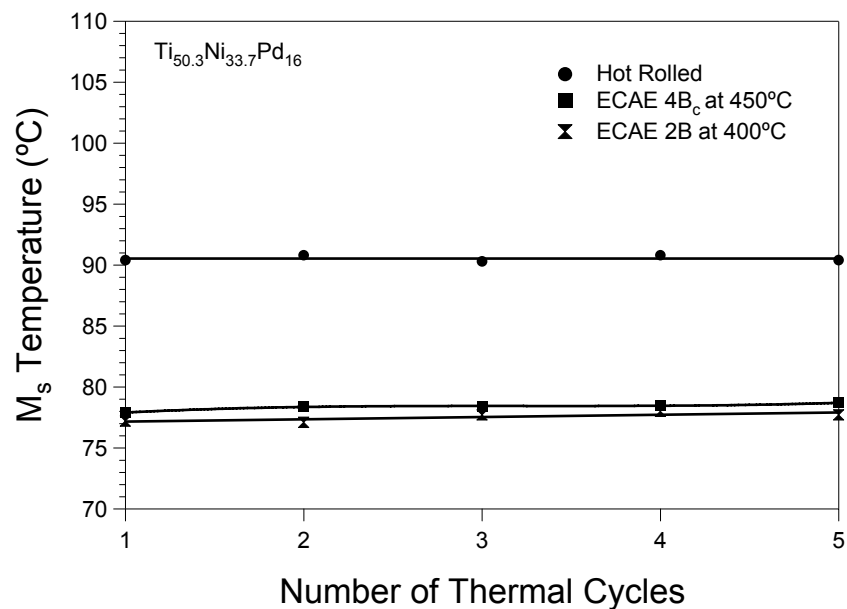
(b)

Figure 5.3 Continued
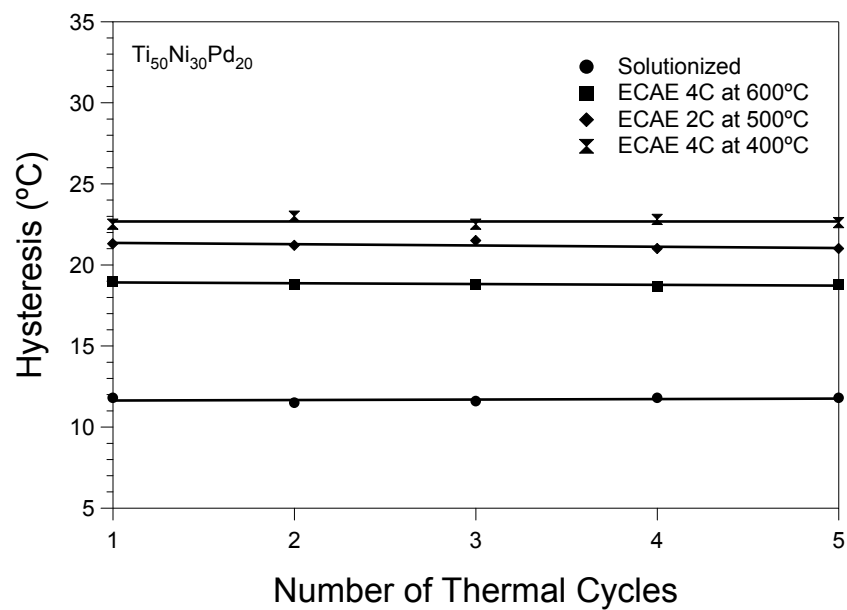
(a)

Figure 5.4 Hysteresis of all TiNiPd samples extracted from the DSC data showing the effect of ECAE processing, ECAE temperature and Pd content (a) $Ti_{50}Ni_{30}Pd_{20}$, (b) $Ti_{50.3}Ni_{33.7}Pd_{16}$.

(b)
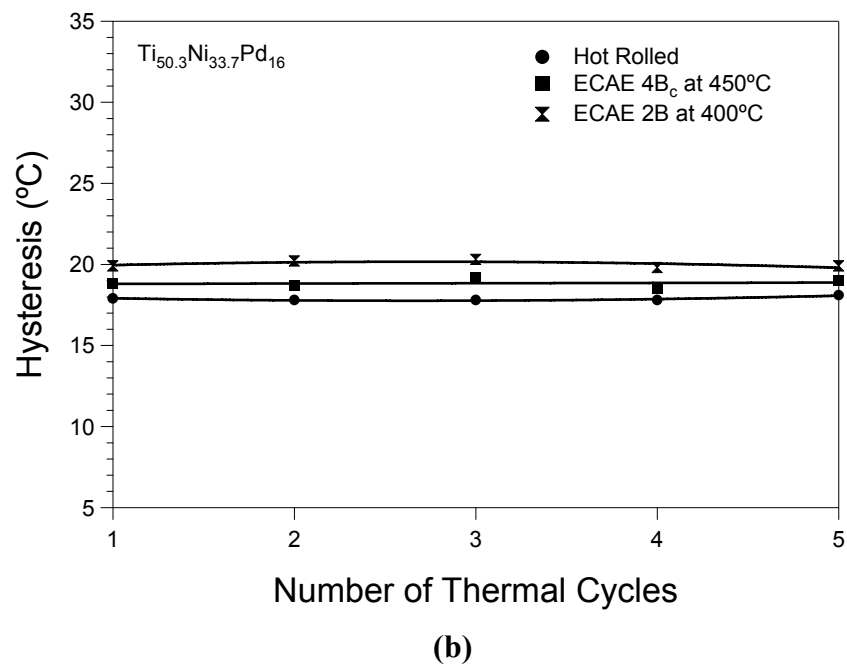
Figure 5.4 Continued

5.3 Microstructural Evolution

Figure 5.5 shows the optical microscopy image of the solutionized $Ti_{50}Ni_{30}Pd_{20}$ alloy demonstrating the average grain size of about 50μm. Figure 5.6 shows the bright field TEM images of the sample ECAE processed at 400°C taken at 200°C (above the A_f temperature) illustrating the grain size reduction after ECAE processing the sample at 400°C for four passes following route C. The grains are elongated as seen in Figure 5.6. The length and width of the grains are 0.5-1μm and 0.2-0.4μm on the average, respectively.
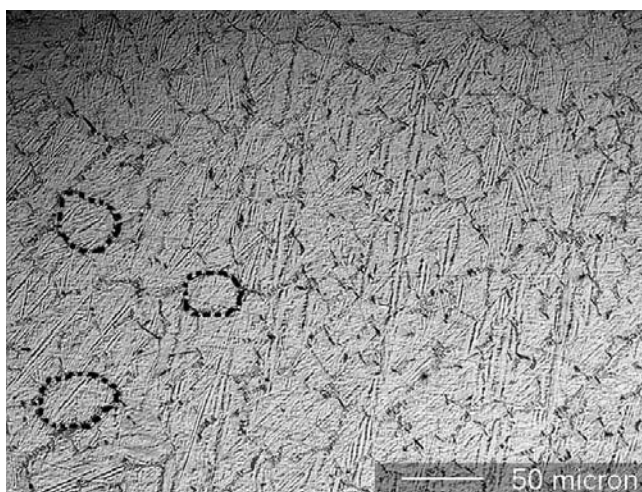
Figure 5.5 Optical micrograph of the solutionized $Ti_{50}Ni_{30}Pd_{20}$ alloy demonstrating the microstructure. Dotted lines are included to distinguish some of the grains and grain size.
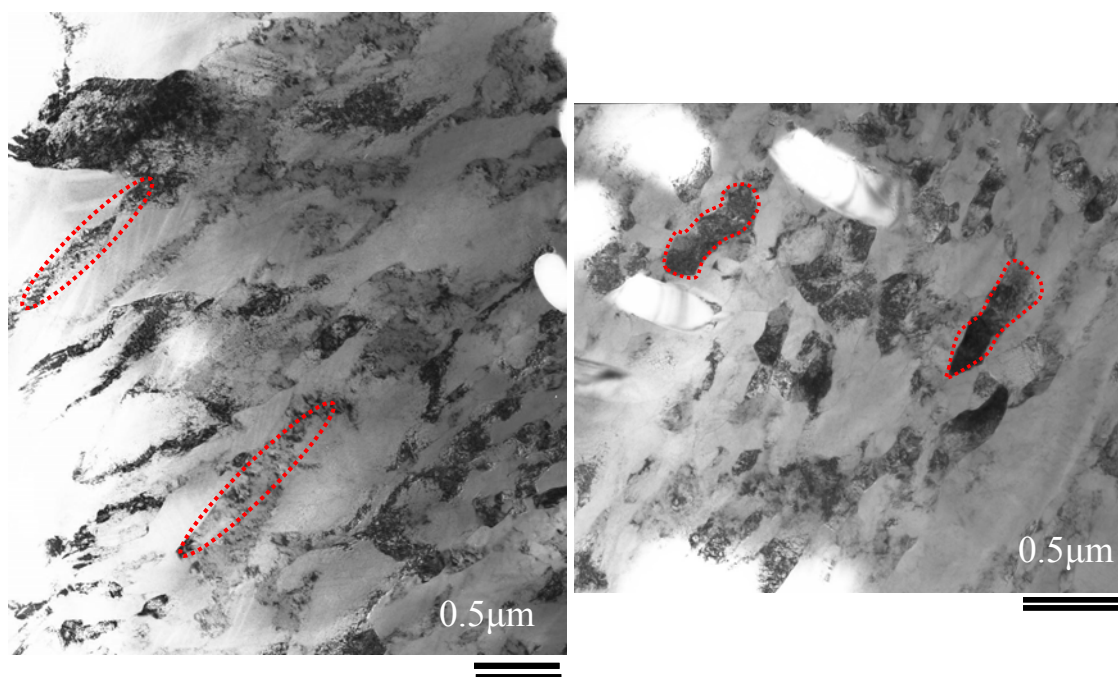
Figure 5.6 Bright field TEM images taken above A_f at 200°C showing the grain size reduction in $Ti_{50}Ni_{30}Pd_{20}$ due to ECAE processing for four passes following route C at 400°C.

Selected area diffraction (SAD) patterns were also recorded to analyze the existing phases in the solutionized and ECAE processed $Ti_{50}Ni_{30}Pd_{20}$ samples. Figure 5.7 shows TEM bright field image taken at room temperature from the solutionized $Ti_{50}Ni_{30}Pd_{20}$ sample and the corresponding selected area diffraction pattern (SAD) from the indicated area which demonstrates B19 martensite phase and [110] Type I twin. Figure 5.8 shows the bright field TEM image taken at room temperature from $Ti_{50}Ni_{30}Pd_{20}$ sample which is ECAE processed at 400° and the corresponding diffraction patterns recorded from the indicated areas in the bright field image. The SAD patterns in Figure 5.8.b and 5.8.c demonstrate <011>Type II and [110] Type I twins, respectively. Although the grain size of $Ti_{50}Ni_{30}Pd_{20}$ after ECAE process decreases the size of the martensite twins does not change. Figure 5.9 represents the bright field TEM image of $Ti_{50}Ni_{30}Pd_{20}$ sample ECAE processed at 400°C and confirms the dislocation density increase after ECAE process.

0.2μm
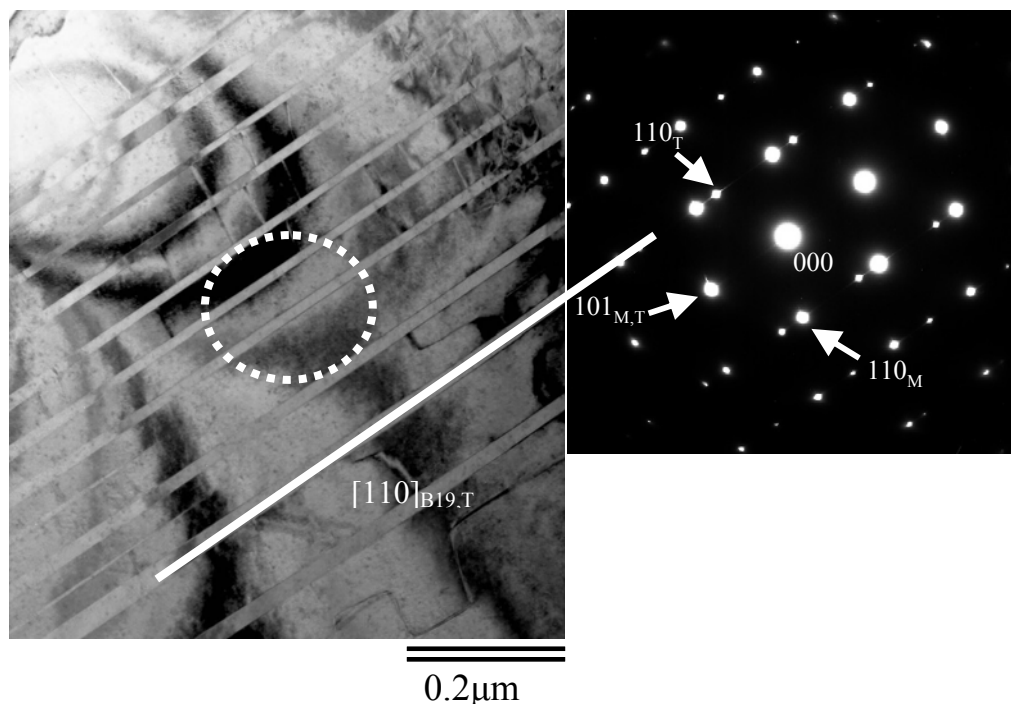
Figure 5.7 Bright field TEM image from the solutionized $Ti_{50}Ni_{30}Pd_{20}$ sample taken at room temperature in martensite and the corresponding diffraction pattern showing the martensite and [110] Type I twin.
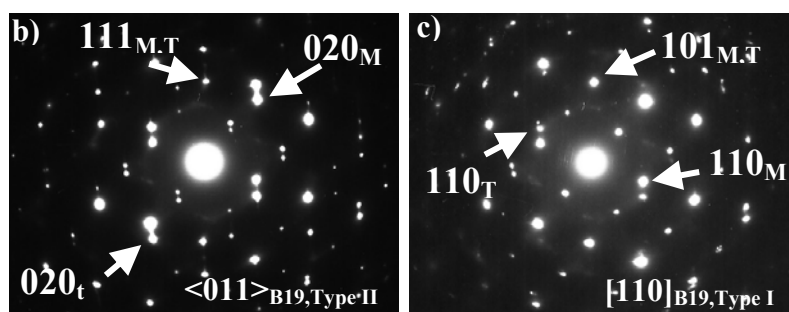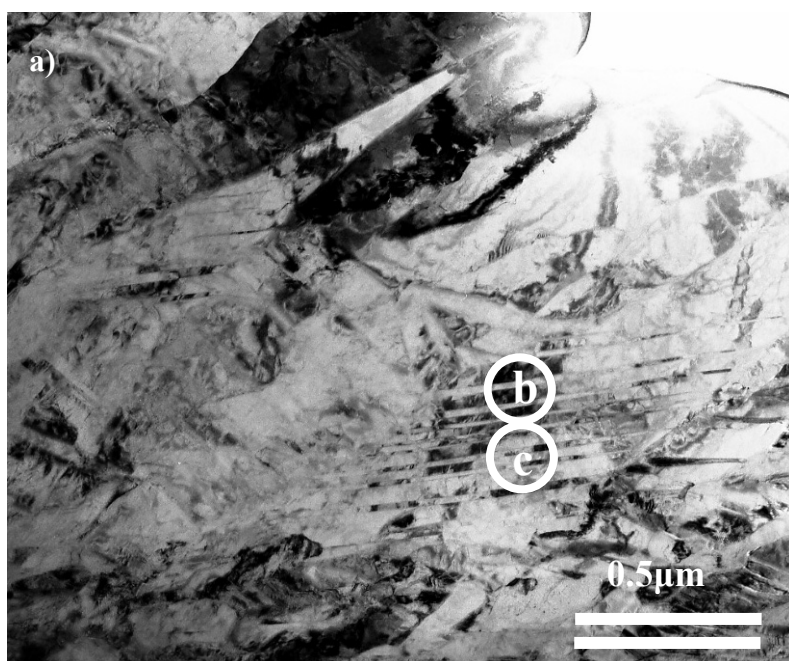
Figure 5.8 Room temperature bright field TEM image of $Ti_{50}Ni_{30}Pd_{20}$ sample ECAE processed at 400°C and the corresponding diffraction pattern showing the martensite b) <011> Type II and c) [110] Type I twins.

0.5μm
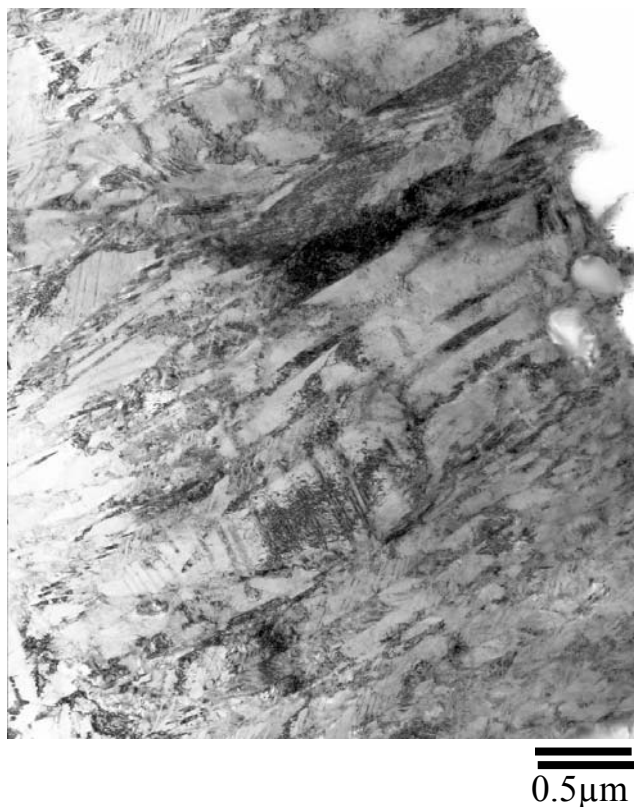
Figure 5.9 Room temperature bright field TEM image of $Ti_{50}Ni_{30}Pd_{20}$ sample ECAE processed at 400°C showing the high dislocation density.

5.4 Monotonic Response under Tension

To analyze the effect of severe plastic deformation on the critical stress level to induce martensite, σ_{SIM}, and the yield stress of stress induced martensite, σ_y^M levels, tension tests were conducted until failure on all the $Ti_{50.3}Ni_{33.7}Pd_{16}$ samples which are under investigation in this research. The test temperatures were chosen to be the same as in the equiatomic NiTi failure experiments which is 15°C above the M_s of each sample under 50MPa. Figure 5.10 illustrates the stress vs. inelastic strain response of the $Ti_{50.3}Ni_{33.7}Pd_{16}$ samples. The σ_{SIM}, σ_y^M and the stress differential (i.e. $\sigma_y^M - \sigma_{SIM}$) are tabulated in Table 5.1. σ_y^M and the stress differential increase after ECAE. The

change in σ_{SIM}, on the other hand, is not significant.
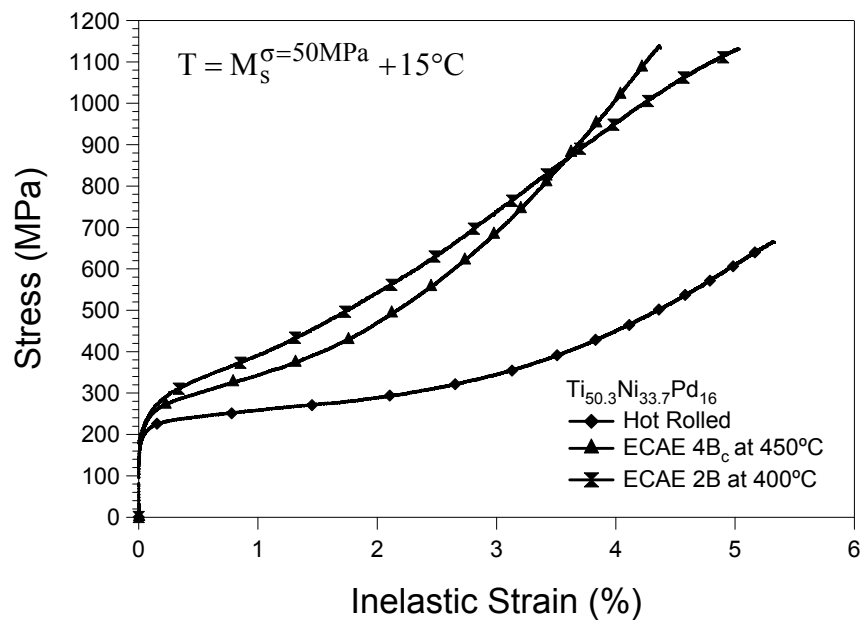
Figure 5.10 Monotonic tensile response of the hot rolled and ECAE processed $Ti_{50.3}Ni_{33.7}Pd_{16}$ samples.

Table 5.1 Critical stresses for the onset of phase transformation and plastic yielding and the stress differential of the $Ti_{50.3}Ni_{33.7}Pd_{16}$ samples determined from the monotonic experiments under tension.

Materials	σ_{SIM} (MPa)	σ_y^M (MPa)	$\sigma_y^M - \sigma_{SIM}$ (MPa)
$Ti_{50.3}Ni_{33.7}Pd_{16}$-Hot Rolled	240	660	420
$Ti_{50.3}Ni_{33.7}Pd_{16}$-ECAE $4B_C$ at 450°C	260	1130	870
$Ti_{50.3}Ni_{33.7}Pd_{16}$-ECAE 2B at 400°C	270	1130	860

5.5 Isobaric Thermal Cyclic Experiments

Isobaric thermal cyclic experiments were performed, incrementally increasing the applied stress after each thermal cycle, using the same specimens throughout the experiment. The transformation and irrecoverable strain levels were determined using the same procedure described in section 4.5.

Figures 5.11 and 5.12 show the strain vs. temperature response of the $Ti_{50}Ni_{30}Pd_{20}$ samples and the $Ti_{50.3}Ni_{33.7}Pd_{16}$ samples, respectively, before and after ECAE. Figures 5.13.a and 5.13.b represent the transformation and irrecoverable strain levels as a function of applied stress determined from the isobaric heating-cooling experiments of all $Ti_{50}Ni_{30}Pd_{20}$ and $Ti_{50.3}Ni_{33.7}Pd_{16}$ samples.

One of the most significant observations from these experiments is that there is a significant increase in the level of stress at which fracture occurs in the $Ti_{50}Ni_{30}Pd_{20}$ samples as the ECAE temperature decreases. The solutionized $Ti_{50}Ni_{30}Pd_{20}$ sample failed under 250MPa and the hot rolled $Ti_{50.3}Ni_{33.7}Pd_{16}$ sample failed under 300MPa, while $Ti_{50}Ni_{30}Pd_{20}$ sample ECAE processed at 400°C failed under 400MPa all during the transformation from austenite to martensite. $Ti_{50.3}Ni_{33.7}Pd_{16}$ sample ECAE processed at 400°C did not fail even at 400MPa. This was attributed to the positive effect of hot rolling prior to ECAE as it will be discussed in the following section. Clearly, ECAE affects considerably the fracture stress level of the TiNiPd alloys in this study. The mechanisms responsible for such improvement will be discussed later.
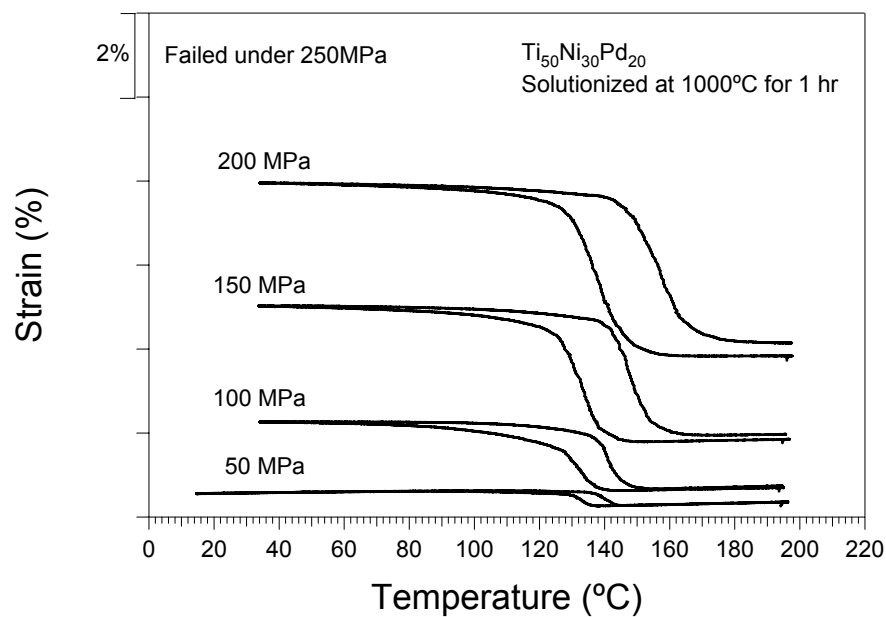
(a)
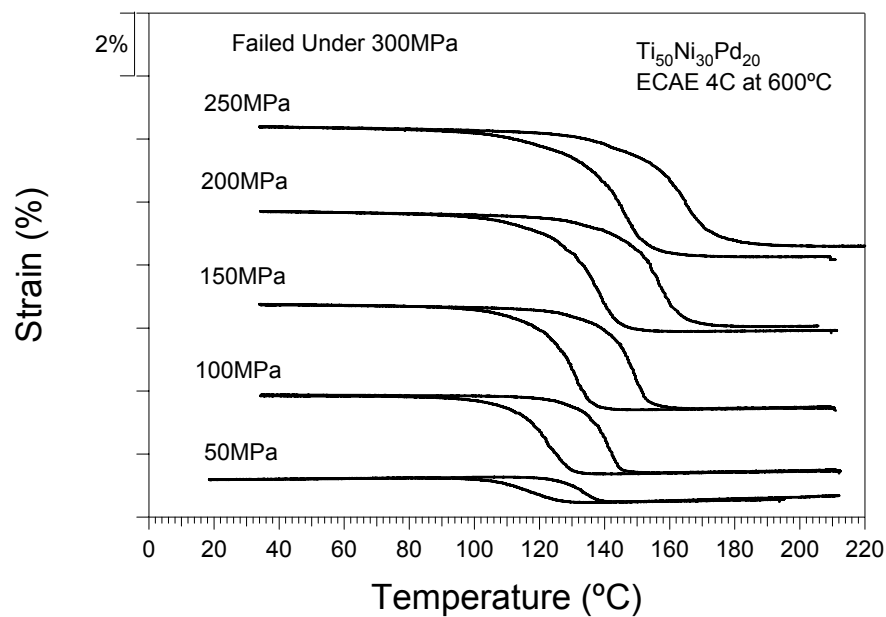
(b)

Figure 5.11 Strain vs. temperature response of the $Ti_{50}Ni_{30}Pd_{20}$ alloy under various constant stress levels: (a) solutionized, (b) ECAE 4C at 600°C, (c) ECAE 2C at 500°C, (d) ECAE 4C at 400°C.
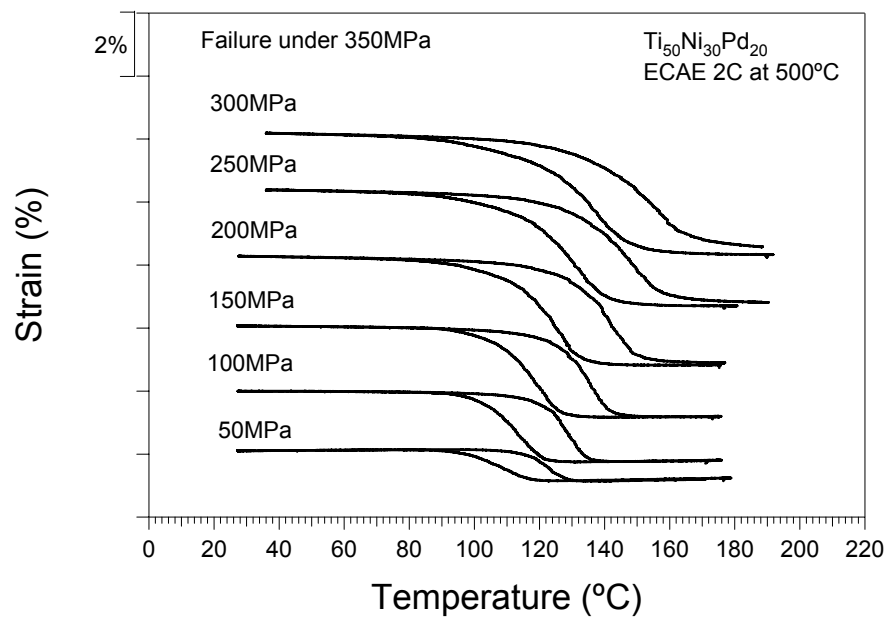
(c)
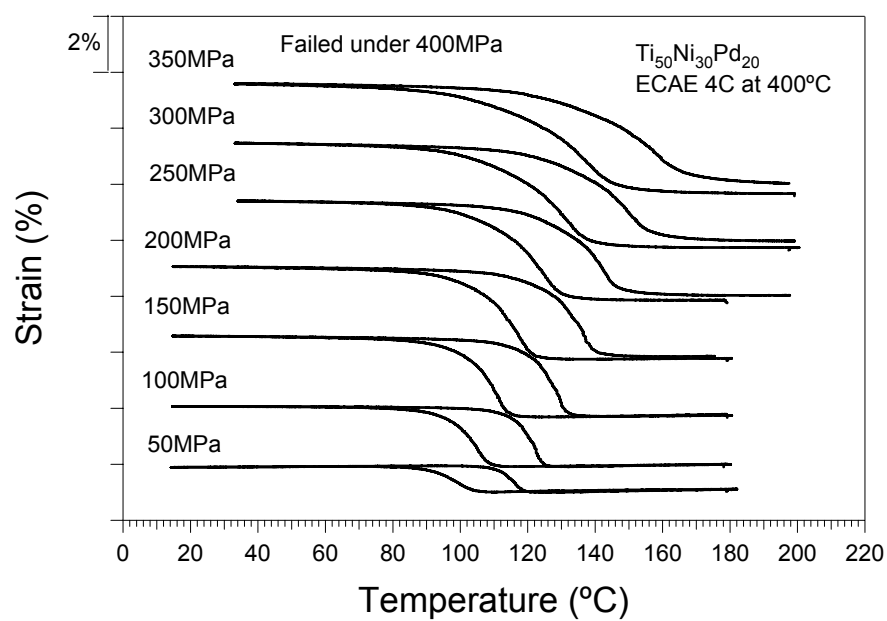
(d)

Figure 5.11 Continued
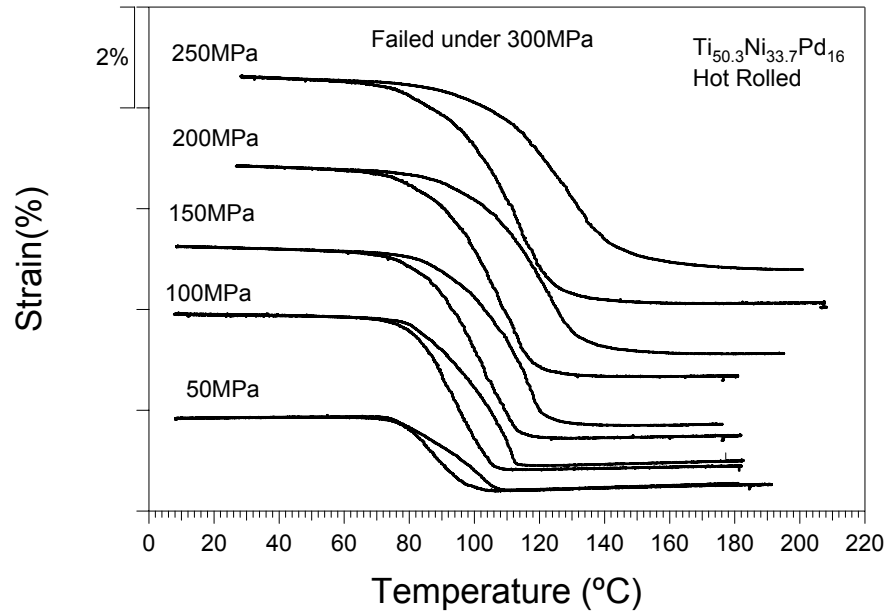
(a)
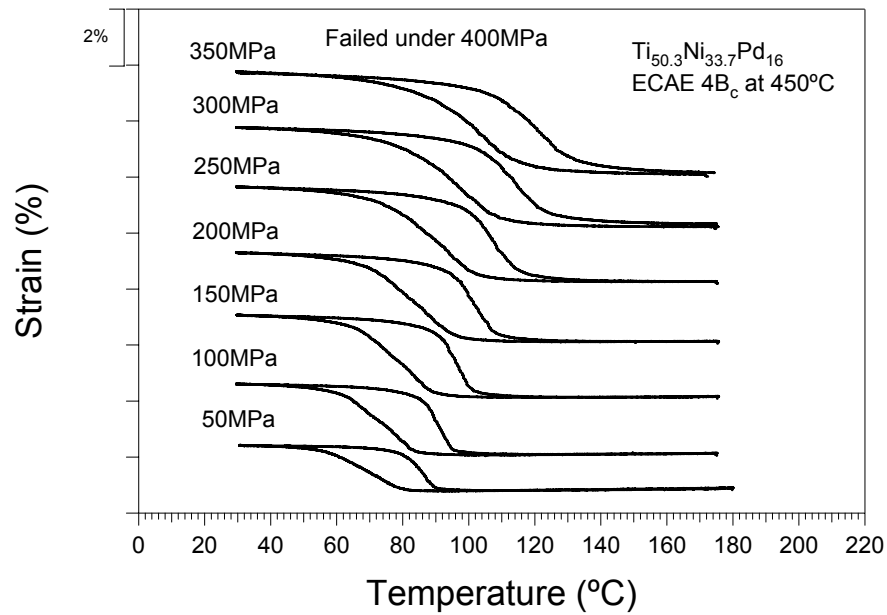
(b)

Figure 5.12 Strain vs. temperature response of the $Ti_{50.3}Ni_{33.7}Pd_{16}$ alloy under various constant stress levels: (a) hot rolled, (b) ECAE 4Bc at 450°C, (c) ECAE 2B at 400°C.

(c)
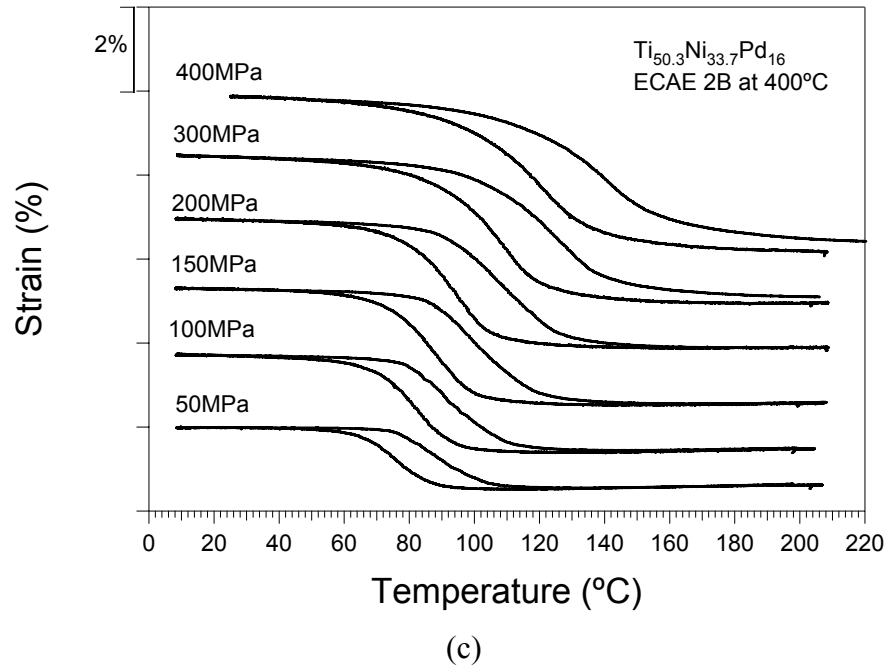
Figure 5.12 Continued

(a)
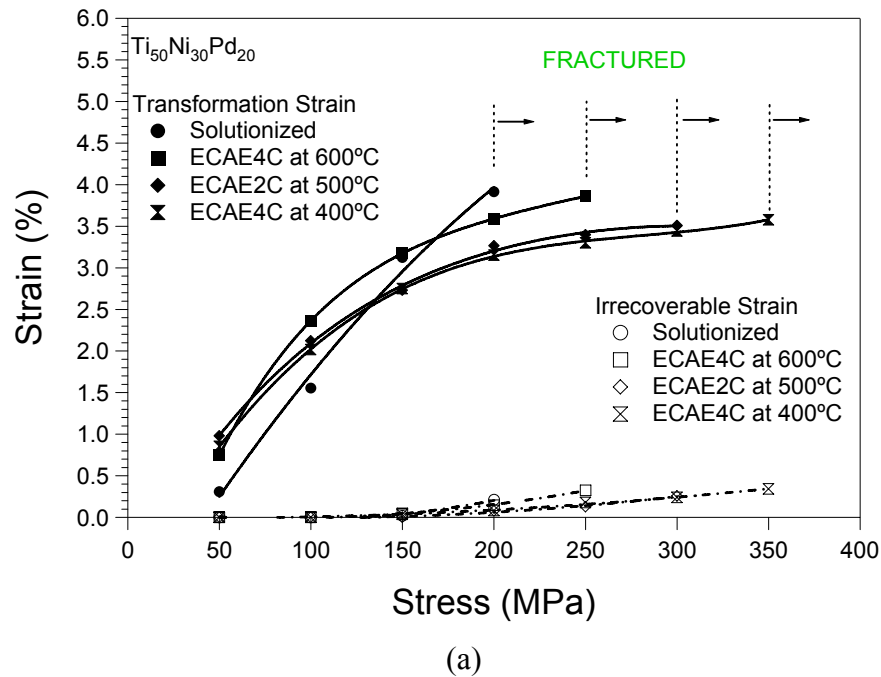
Figure 5.13 Transformation and irrecoverable strain response as a function of constant tensile stress levels in the (a) $Ti_{50}Ni_{30}Pd_{20}$, (b) $Ti_{50.3}Ni_{33.7}Pd_{16}$ samples during isobaric thermal cyclic experiments.

(b)
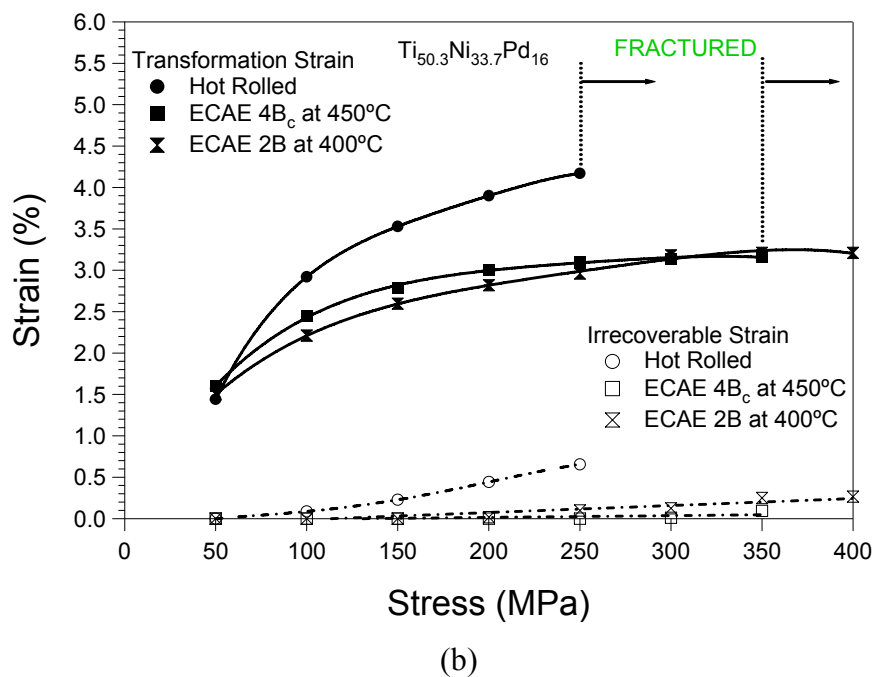
Figure 5.13 Continued

The irrecoverable and transformation strain levels were extracted from the isobaric cooling-heating experiments using the same procedure defined in section 4.5 and in Figure 4.10. Figure 5.13.a and 5.13.b represent the transformation and irrecoverable strain levels as a function of applied stress level determined from the isobaric cooling-heating experiments conducted on $Ti_{50}Ni_{30}Pd_{20}$ and $Ti_{50.3}Ni_{33.7}Pd_{16}$ samples, respectively. In Figure 5.13, the irrecoverable strain levels of the solutionized $Ti_{50}Ni_{30}Pd_{20}$ sample are lower than that of the $Ti_{50.3}Ni_{33.7}Pd_{16}$ hot rolled sample. One can observe a detectable irrecoverable strain only above 250MPa for the $Ti_{50}Ni_{30}Pd_{20}$ and $Ti_{50.3}Ni_{33.7}Pd_{16}$ samples extruded at 400°C. As the extrusion temperature decreases, the irrecoverable strain level of $Ti_{50}Ni_{30}Pd_{20}$ samples also decreases. The effect of number of passes on the irrecoverable strain can be monitored in the results of $Ti_{50.3}Ni_{33.7}Pd_{16}$ samples which are shown in Figure 5.13.b. The irrecoverable strain levels of the $Ti_{50.3}Ni_{33.7}Pd_{16}$ sample ECAE processed at 400°C do not exceed 0.3% under 400MPa. The irrecoverable strain levels of $Ti_{50.3}Ni_{33.7}Pd_{16}$ sample which is ECAE processed at 450°C for four passes are lower than that of $Ti_{50.3}Ni_{33.7}Pd_{16}$ sample which is processed at

400°C for two passes and are almost negligible at all stress levels below 400MPa.

The transformation strain level of the solutionized $Ti_{50}Ni_{30}Pd_{20}$ increases from 0.5% to 4% up to 200MPa at which the sample failed during cooling. The ECAE processed $Ti_{50}Ni_{30}Pd_{20}$ samples show higher transformation strain levels under 50MPa and 100MPa. Since the solutionized sample failed at 250MPa, it is not possible to compare the transformation strain levels after this point. However, the trend is the stabilization of the transformation strain levels of ECAE processed samples at 3.5% above 200MPa. On the other hand, the transformation strain level of solutionized sample keeps increasing drastically. The trend in the ECAE processed $Ti_{50.3}Ni_{33.7}Pd_{16}$ samples is the same for the ECAE processed $Ti_{50}Ni_{30}Pd_{20}$ samples. The difference in the transformation strain levels of $Ti_{50.3}Ni_{33.7}Pd_{16}$ and $Ti_{50}Ni_{30}Pd_{20}$ samples is that the transformation strain levels of ECAE processed $Ti_{50}Ni_{30}Pd_{20}$ samples are higher than that of the solutionized sample under 50MPa and 100MPa while the transformation strain levels of ECAE processed $Ti_{50.3}Ni_{33.7}Pd_{16}$ samples and hot rolled sample are almost same under 50MPa and are lower than that of the hot rolled sample under 100MPa and higher stress levels.

The main observations from Figures 5.13 can be summarized as: 1) fracture stress level of the samples increases as the ECAE temperature decreases, 2) irrecoverable strain levels of the ECAE processed samples are lower than the unprocessed samples, 3) the effect of the number of ECAE passes on the irrecoverable strain levels is similar to the effect of ECAE temperature i.e. the lower the ECAE temperature and the higher the number of ECAE passes is, the lower the irrecoverable strain level gets, 4) the transformation strain levels of the ECAE processed $Ti_{50}Ni_{30}Pd_{20}$ samples are higher than that of the solutionized sample at low stress levels and lower at high stress levels, and 5) the transformation strain levels of ECAE processed samples stabilize at 3.5% for $Ti_{50}Ni_{30}Pd_{20}$ alloy 3.0% for $Ti_{50.3}Ni_{33.7}Pd_{16}$ alloy above 200MPa.

The fracture stress levels are marked for each case except the $Ti_{50.3}Ni_{33.7}Pd_{16}$ sample ECAE processed at 400°C for two passes which did not fail even under 400MPa in Figure 5.13. All the samples were failed during cooling at the particular stress level,

i.e. during austenite to martensite transformation.

Figure 5.14 demonstrates the temperature and stress phase diagram for the onset of martensitic transformation for all $Ti_{50}Ni_{30}Pd_{20}$ and $Ti_{50.3}Ni_{33.7}Pd_{16}$ samples determined from the isobaric heating–cooling experiments. For the sake of completeness, M_s temperatures from the DSC experiments in Figure 5.3 are also included. Clearly, a linear relationship between stress and temperature can be observed in this figure for all samples, as expected from the Clausius-Clapeyron (CsCl) relationship for thermoelastic martensitic transformations. The CsCl slopes which can also be represented as $\frac{d\sigma}{dT}$ for each sample are tabulated in Table 5.2. The CsCl slopes of the $Ti_{50}Ni_{30}Pd_{20}$ alloy decrease after ECAE and the slopes of the $Ti_{50.3}Ni_{33.7}Pd_{16}$ alloy slightly increase after ECAE.

It was observed from Figure 5.14 that there is a mismatch between the $M_s^{\sigma=0}$ from DSC experiment and $M_s^{\sigma=0}$ from the extrapolation of CsCl curves in all $Ti_{50}Ni_{30}Pd_{20}$ samples. The mismatch gets smaller in $Ti_{50.3}Ni_{33.7}Pd_{16}$ samples. In hot rolled $Ti_{50.3}Ni_{33.7}Pd_{16}$ sample $M_s^{\sigma=0}$ from DSC experiment is similar to $M_s^{\sigma=0}$ from the extrapolation of CsCl curves. Another observation is the decrease in M_s temperature under applied stress with the decrease in ECAE temperature in $Ti_{50}Ni_{30}Pd_{20}$ samples. On the other hand, in $Ti_{50.3}Ni_{33.7}Pd_{16}$ samples, the effect of number of ECAE passes on M_s temperatures is more significant than the effect of ECAE temperature. The implications of these results and the possible rationale for such observations will be discussed in section 5.8.
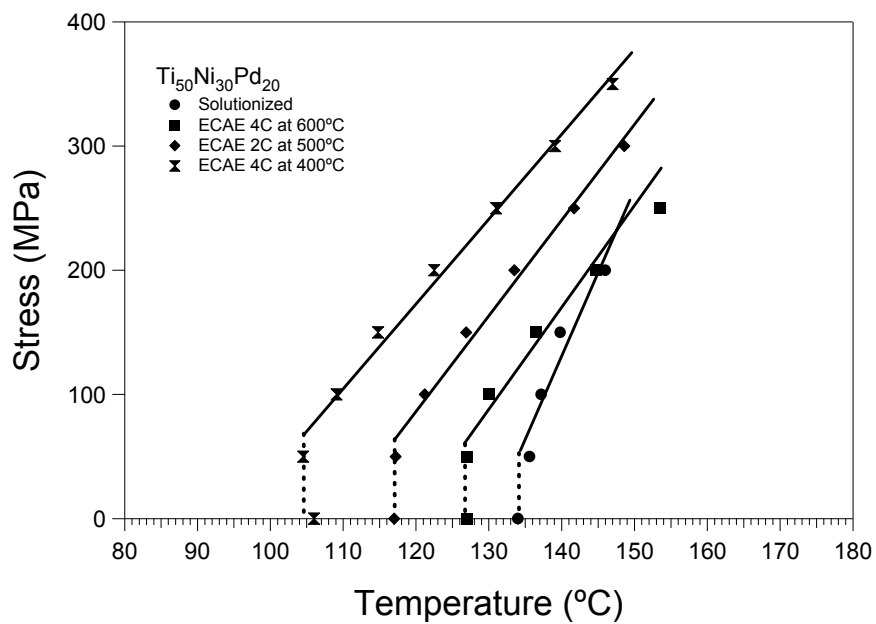
(a)
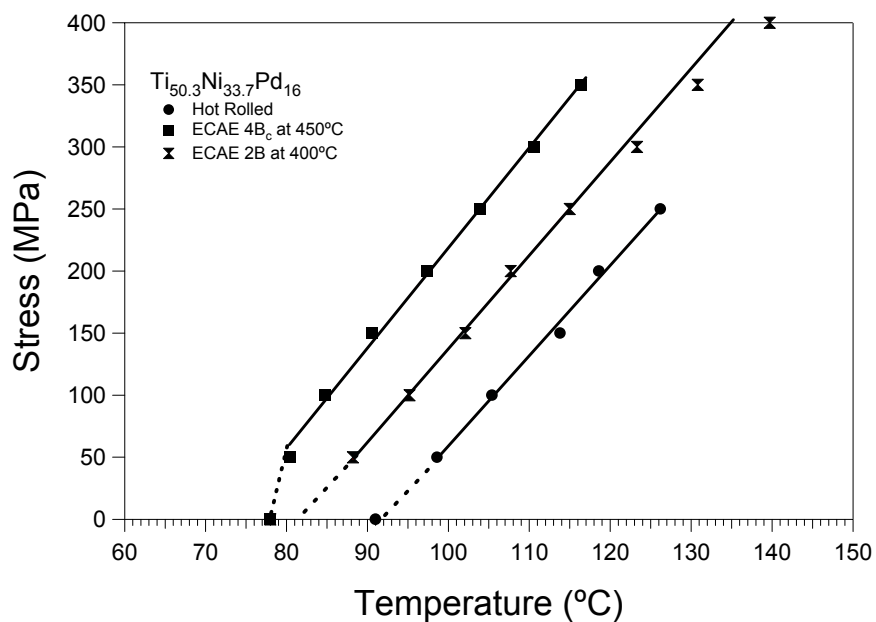
(b)

Figure 5.14 Critical stress versus M_s temperatures of (a) $Ti_{50}Ni_{30}Pd_{20}$ and (b) $Ti_{50.3}Ni_{33.7}Pd_{16}$ samples before and after ECAE determined from the isobaric heating-cooling shown in Figure 5.13. For the sake of the completeness the M_s temperatures from the DSC experiments (Figure 5.3) are also included in the figure.

Table 5.2 The slopes of the critical stress vs. temperature curves ($\frac{d\sigma}{dT}$) shown in Figure 5.14.

Material	$\frac{d\sigma}{dT}$ (MPa/°C)
$Ti_{50}Ni_{30}Pd_{20}$-Solutionized	13.5
$Ti_{50}Ni_{30}Pd_{20}$-ECAE 4C at 600°C	8.1
$Ti_{50}Ni_{30}Pd_{20}$-ECAE 2C at 500°C	7.7
$Ti_{50}Ni_{30}Pd_{20}$-ECAE 4C at 400°C	6.8
$Ti_{50.3}Ni_{33.7}Pd_{16}$-Hot Rolled	7.2
$Ti_{50.3}Ni_{33.7}Pd_{16}$-ECAE $4B_c$ at 450°C	8.1
$Ti_{50.3}Ni_{33.7}Pd_{16}$-ECAE 2B at 400°C	7.6

Thermal hystresis were extracted from the isobaric cooling-heating experiments using the same procedure defined in section 4.5 and in Figure 4.10. Figure 5.15.a and 5.15.b represent the thermal hysteresis as a function of applied stress level determined from the isobaric cooling-heating experiments conducted on $Ti_{50}Ni_{30}Pd_{20}$ and $Ti_{50.3}Ni_{33.7}Pd_{16}$ samples, respectively. Thermal hysteresis increase after ECAE $Ti_{50}Ni_{30}Pd_{20}$ and $Ti_{50.3}Ni_{33.7}Pd_{16}$ samples and increase further with the increase in applied stress. One intriguing observation is the lower thermal hysteresis under 50MPa with respect to thermal hysteresis under no load in all samples. The rationale behind this observation is not clear at this point.
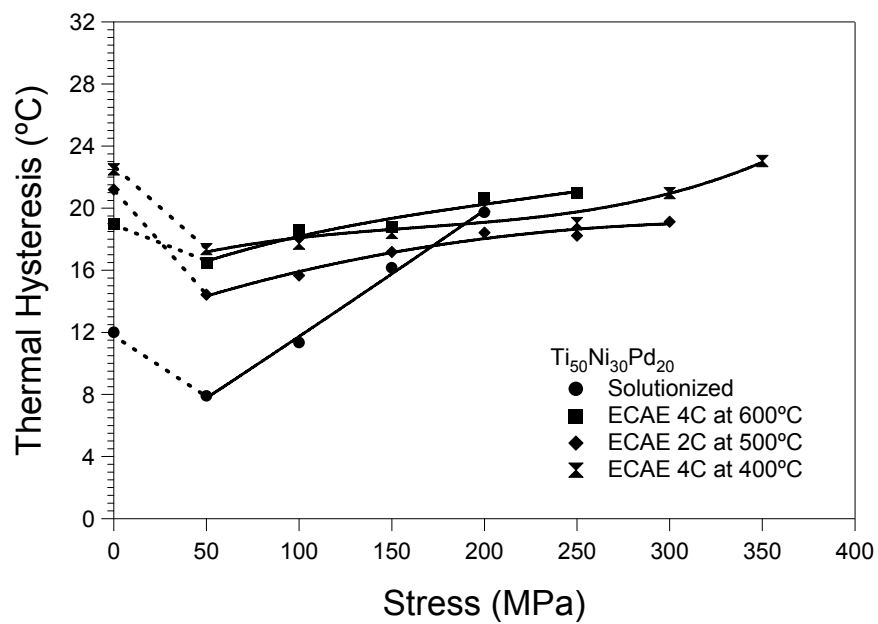
(a)
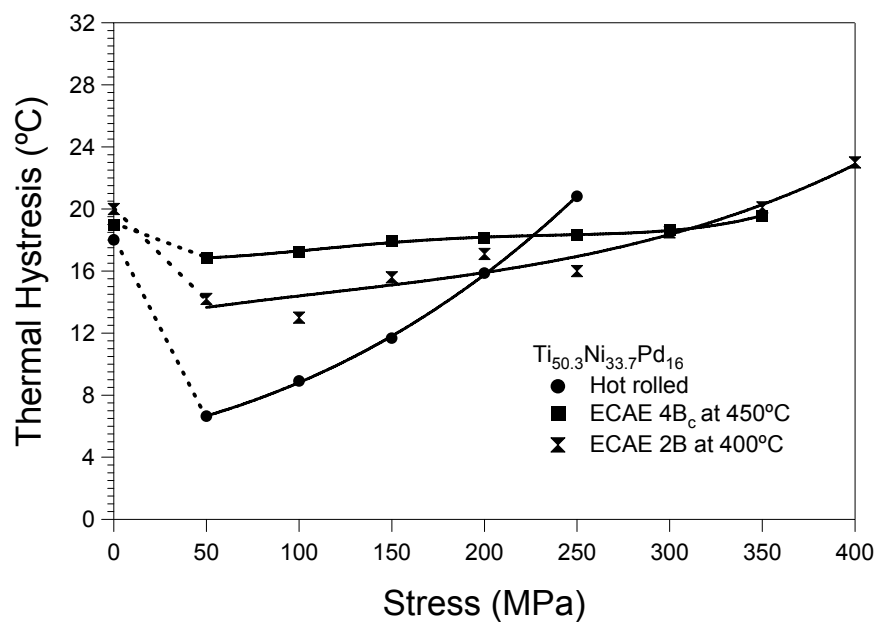
(b)

Figure 5.15 Thermal hysteresis as a function of constant tensile stress levels in the (a) $Ti_{50}Ni_{30}Pd_{20}$, (b) $Ti_{50.3}Ni_{33.7}Pd_{16}$ samples during isobaric thermal cyclic experiments.

5.6 Microstructural Investigation of Failure Samples

To reveal the potential reasons for premature failure at low stress levels in ternary alloys during the isobaric heating-cooling experiments, the microstructure of the failed samples were studied using scanning electron microscope (SEM) and Electron Microprobe (EM).

Figure 5.16 represents the back scattered electron SEM images taken from the $Ti_{50}Ni_{30}Pd_{20}$ solutionized sample and samples ECAE processed at 600°C and 400°C. The images demonstrate the second phase particles in the matrix. To analyze the composition of the precipitates, the wave dispersion spectroscopy (WDS) and energy dispersion spectroscopy (EDS) analysis were conducted on the selected precipitates. It was found from both of the analysis that the black precipitates indicated in Figure 5.16.b are Ti(C,O) precipitates while the light gray precipitates are $Ti_2(Ni, Pd)$ intermetallics. The EDS analyses of the indicated precipitates in Figure 5.16.b are represented in Figure 5.17. The carbon and oxygen elements in Ti(C, O) particles are also analyzed using WDS since WDS analysis allows a more spectral resolution and more sensitivity on low atomic number elements than EDS analysis does and this analysis is shown in Figure 5.17.b. The images in Figure 5.16 show the notable decrease in precipitate size and volume after ECAE at 400°C and the second phase particles are more homogeneously distributed in ECAE processed at 400°C sample than that of in solutionized sample. The average size and volume percent of the precipitates before and after ECAE is tabulated in Table 5.3.

(a)

(b)

(c)
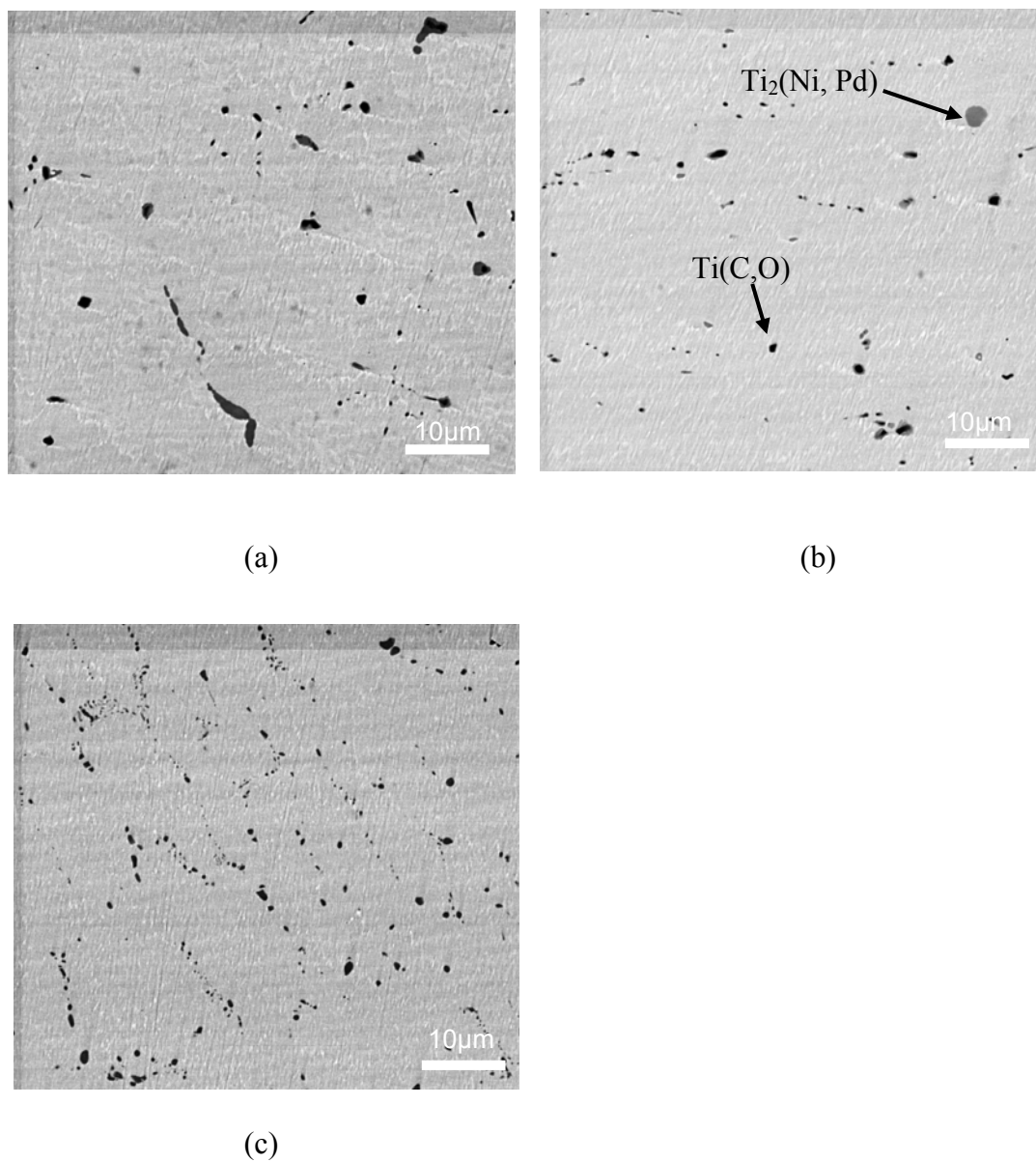
Figure 5.16 Back scattered electron SEM images showing the precipitate size and distribution within the matrix of $Ti_{50}Ni_{30}Pd_{20}$ samples (a) solutionized, (b) ECAE processed at 600°C and (c) ECAE processed at 400°C.
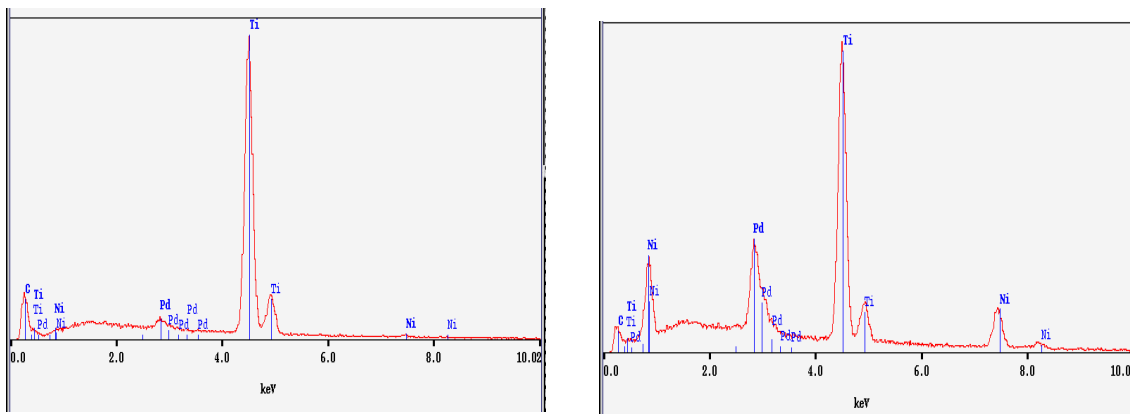
(a)   (b)
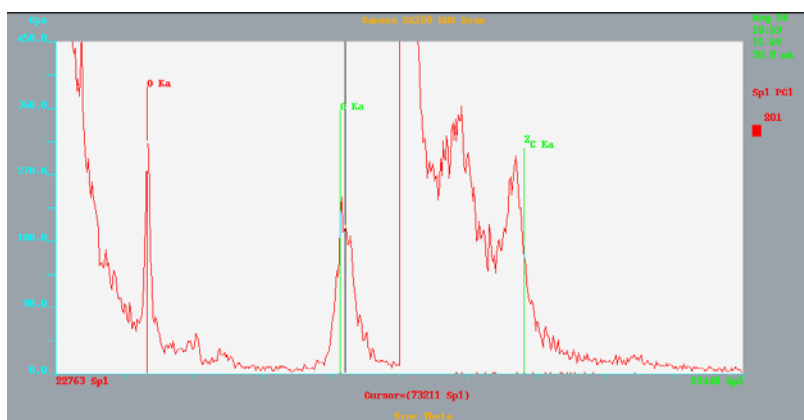
(c)

Figure 5.17 EDS and WDS analyses of the second phase particles in the matrix of Ti$_{50}$Ni$_{30}$Pd$_{20}$ samples for (a) dark particles Ti(C, O) in Figure 5.16 and (b) light gray particles Ti$_2$(Ni, Pd) in Figure 5.16 (c) WDS analysis showing the carbon and oxygen in dark particles Ti(C, O).

Figure 5.18 represents secondary electron SEM image of the solutionized Ti$_{50}$Ni$_{30}$Pd$_{20}$ sample. The image shows that there are pores in the matrix which might be responsible for the premature failures in the isobaric cooling-heating experiments. The length of the pore shown in Figure 5.18 is around 100μm. No pores were observed in the

$Ti_{50}Ni_{30}Pd_{20}$ sample ECAE processed at 400°C.
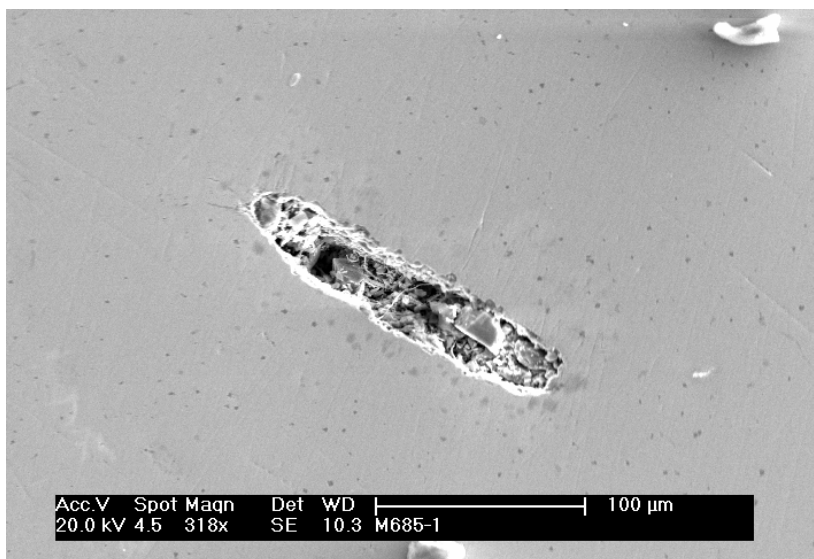
Figure 5.18 Secondary electron SEM image of solutionized $Ti_{50}Ni_{30}Pd_{20}$ sample showing one of the porosity in the matrix.

Table 5.3 The average size of the precipitates in $Ti_{50}Ni_{30}Pd_{20}$ samples before and after ECAE.

Materials	Average Size(μm)	Volume (%)
Solutionized	2.3±1	2.1±0.1
ECAE 4C at 400°C	1.2±0.4	1.6±0.1

It was shown that high strains induced in ECAE not only lead to the grain refinement but also affect the size and the distribution of the second phase/precipitates contained within the matrix. The precipitates either fragment into smaller parts or dissolve in the matrix since both the average size and volume percent of the precipitates decrease notably after ECAE. $Ti_2(Ni, Pd)$ precipitates are probably dissolved in the matrix since no light gray precipitates were observed in the sample ECAE processed at 400°C as shown in Figure 5.16.c. This observation is not uncommon for ECAE.

Langdon et al. showed that ECAE leads to the formation of ultrafine grain size with finely dispersed precipitates in AlZnMg alloys [131]. In addition, ECAE affects the porosity content of the $Ti_{50}Ni_{30}Pd_{20}$ samples.

5.7 Thermal Cyclic Experiments under Constant Stress

As shown in section 5.5, none of the ECAE processed $Ti_{50}Ni_{30}Pd_{20}$ samples demonstrate irrecoverable strain at and below 150MPa. Although the solutionized $Ti_{50}Ni_{30}Pd_{20}$ sample failed at 250MPa in isobaric heating-cooling experiments, it failed at the second cycle under 150MPa in the thermal cyclic experiments. Figures 5.19 and 5.20 represent the strain-temperature response of the ECAE processed $Ti_{50}Ni_{30}Pd_{20}$ samples under 150MPa and 250MPa for ten cycles, respectively. The main purpose to conduct cyclic tests was to evaluate the transformation and the irrecoverable strain levels as a function of the number of cycles. The samples ECAE processed at 600°C and 500°C show no irrecoverable strain under 150MPa, therefore, the sample ECAE processed at 400°C was not thermally cycled under 150MPa.The transformation and irrecoverable strain levels for ten cycles determined from these thermal cyclic experiments are presented in Figure 5.21. Under 250MPa, the samples ECAE processed at 500°C and 400°C show no detectable irrecoverable strain after the first cycle. The transformation strain levels of the samples ECAE processed at 600°C and 500°C under 150MPa are stable around 3%. Under 250MPa, the transformation strain levels of samples ECAE processed at 500°C and 400°C are again stable and about 3.2%.
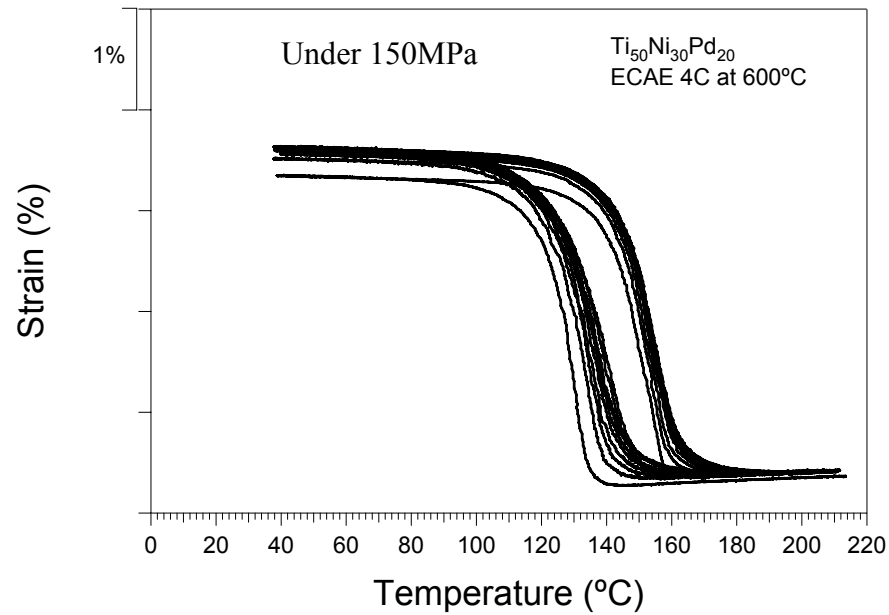
(a)
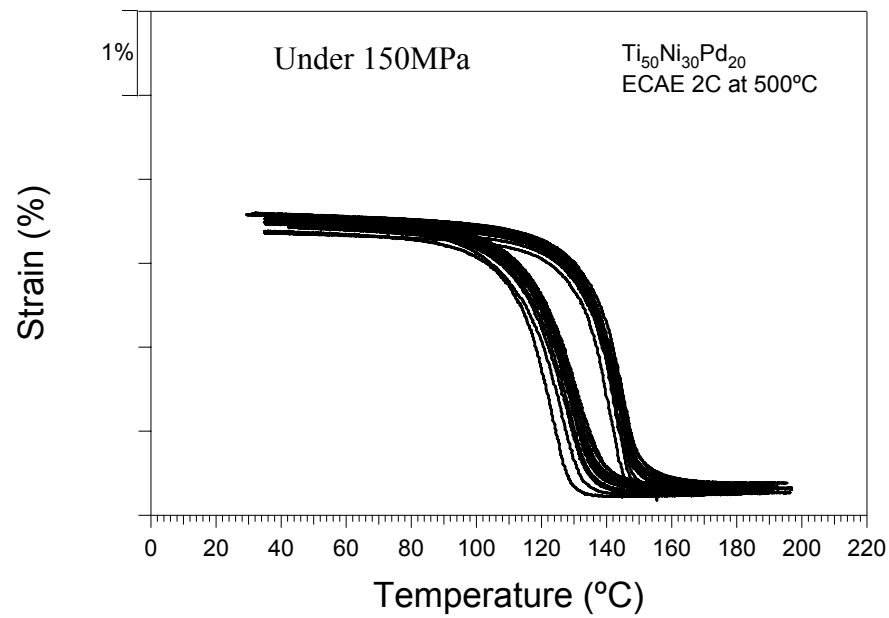
(b)

Figure 5.19 Strain vs. temperature response of the ECAE processed $Ti_{50}Ni_{30}Pd_{20}$ alloy under 150MPa (a) ECAE 4C at 600°C, (b) ECAE 2C at 500°C.
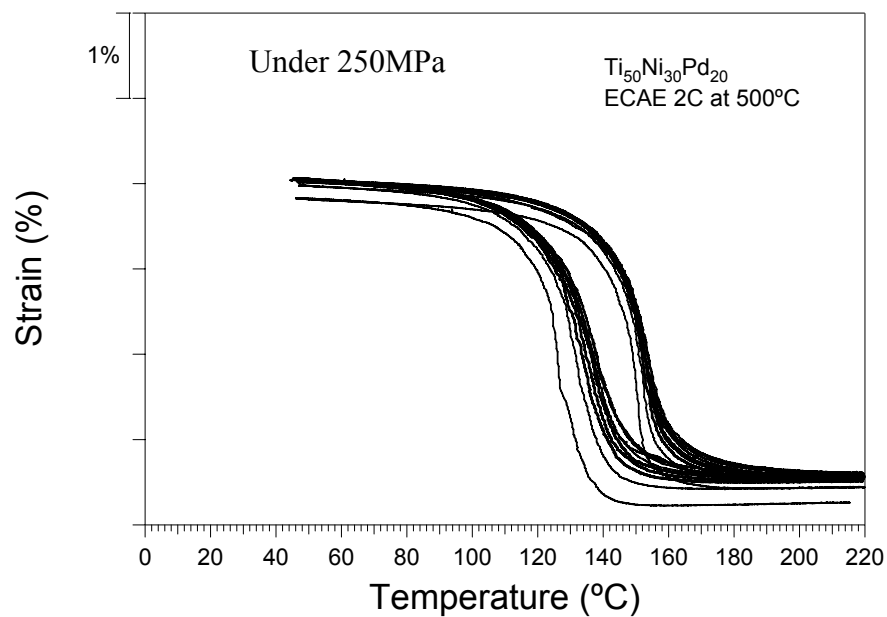
(a)
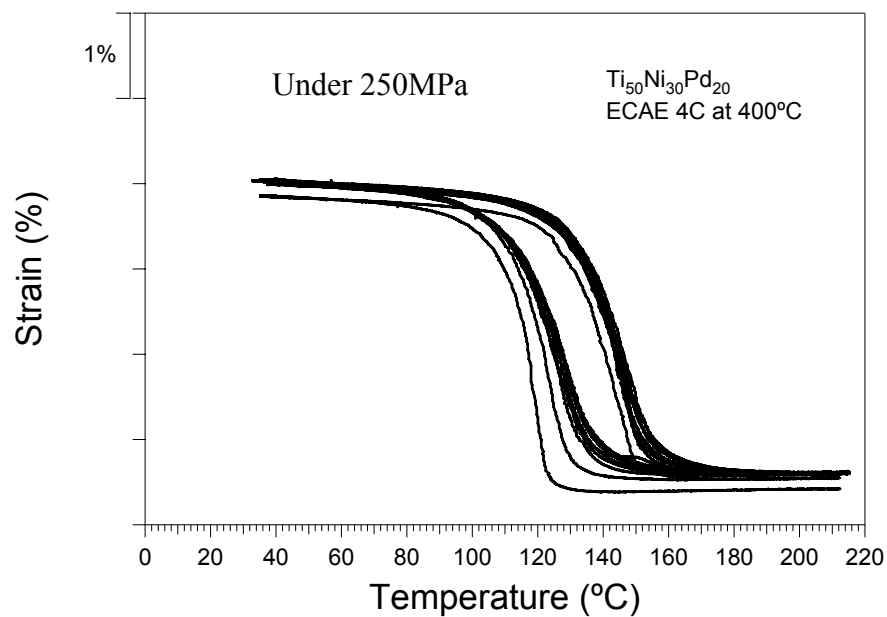
(b)

Figure 5.20 Strain vs. temperature response of the ECAE processed $Ti_{50}Ni_{30}Pd_{20}$ alloy under 250MPa (a) ECAE 2C at 500°C, (b) ECAE 4C at 400°C.
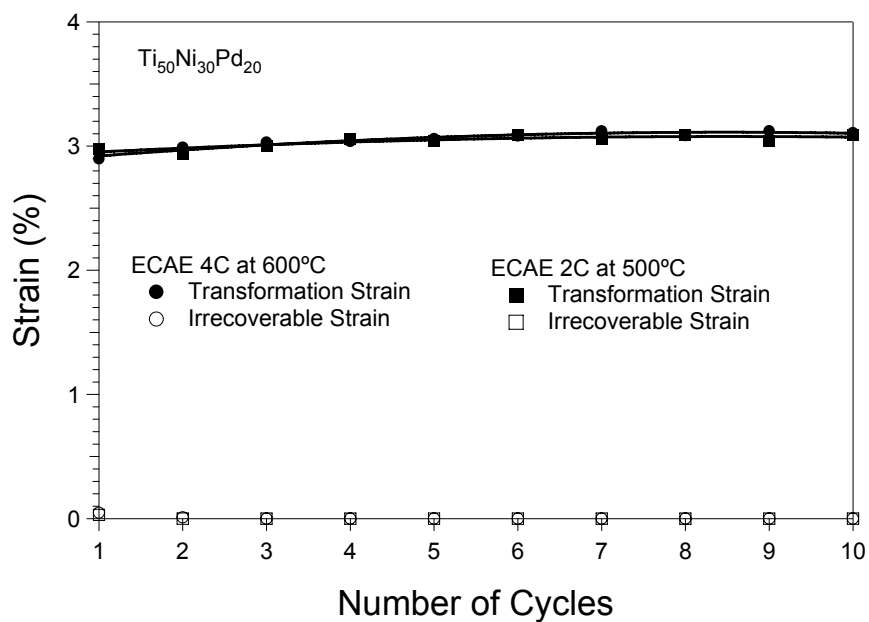
(a)
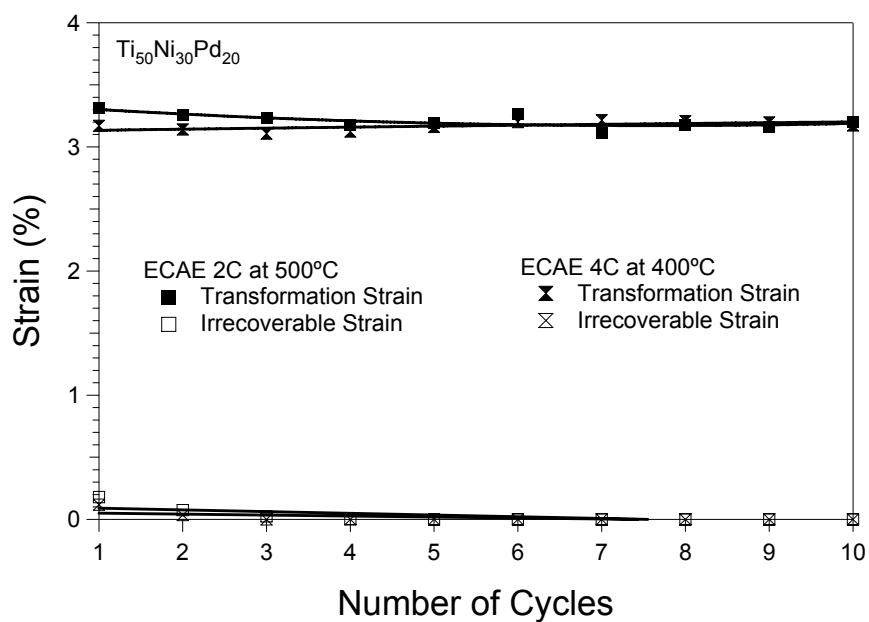
(b)

Figure 5.21 Transformation and irrecoverable strain evolution during thermal cyclic experiments in the ECAE processed $Ti_{50}Ni_{30}Pd_{20}$ samples as a function of number of cycles (a) ECAE 4C at 600°C and ECAE 2C at 500°C under 150MPa for 10 cycles and (b) ECAE 2C at 500°C and ECAE 4C at 400°C under 250MPa.

The thermal cyclic experiments were not conducted on $Ti_{50.3}Ni_{33.7}Pd_{16}$ because the results are expected to be similar to what determined from the thermal cyclic experiments on $Ti_{50}Ni_{30}Pd_{20}$.

The main observations from these experiments are: 1) there is no irrecoverable strain under 150MPa and insignificant irrecoverable strain under 250MPa; 2) the transformation strain levels are stable for all samples and vary between 3 to 3.5%, there is no significant strain evolution.

5.8 Discussion of the Results

In the present study, the main purpose is to investigate the shape memory characteristics of $Ti_{50}Ni_{30}Pd_{20}$ and $Ti_{50.7}Ni_{33.7}Pd_{16}$ alloys since only a limited number of studies were undertaken on TiNiPd alloys up to date [105, 112]. The experiments mimicking the real actuator operation (i.e. thermal cycling under load) were performed only by the NASA Glenn research group very recently, about the same time with the present work [32]. They have investigated the evolution in transformation temperatures, work behavior, and dimensional stability of the TiNiPd alloys with different Pd contents. The main differences between this study and the studies of the NASA group are the Pd content and in the present case the investigation of the effect of ECAE on microstructure and the corresponding improvement of the mechanical and shape memory behavior of the alloys. The present NiTiPd compositions were selected to have all transformation temperatures in between 100°C and 150°C for a particular target application. Thus, this is the first study that thoroughly investigates the shape memory and actuator characteristics of NiTiPd alloys. The main observations could be summarized as follows:

1)   The grains are elongated in the ECAE processed samples. The average grain size of the samples was reduced from 50μm down to 0.5 μm after ECAE. The length and width of the grains are 0.5-1μm and 0.2-0.4μm, respectively, for the sample ECAE processed at 400°C.

2)   The twin mode in martensite was found to be a mixture of typical Type I

and Type II twins. There is no change in the twin type and twin size after ECAE.

3)   Addition of Pd to TiNi alloy enhances the shape memory characteristics of NiTi alloys such as the significant decrease in thermal hysteresis and irrecoverable strain under constant stress levels, and transformation temperature cyclic stability under no load condition.

4)   ECAE led to increase the strength differential between the critical stress to induce martensite and the yield stress of martensite and led to a notable improvement in the thermal cyclic stability by further reducing the irrecoverable strain levels under constant stresses which can be attributed to the increase in critical stress level for dislocation slip due to grain size refinement and dislocation density increase via ECAE.

5)   ECAE led to decrease the size and volume fraction of the undesirable precipitates which is thought to be the main reason for the premature failure in the isobaric heating-cooling experiments.

6)   The decrease in size and volume fraction of the precipitates led to the increase in the stress levels at which the failure occurs during isobaric heating-cooling experiments.

The possible mechanisms responsible from these observations are discussed below.

5.8.1 Grain Size and Microstructural Evolution during ECAE

The knowledge base gathered from the transmission electron microscopy study of equiatomic NiTi alloy showed us that the lowest ECAE processing temperature has the most influence on the grain size refinement. Therefore, the solutionized $Ti_{50}Ni_{30}Pd_{20}$ sample and the sample ECAE processed at 400°C were chosen for the transmission electron microscopy study to investigate the grain refinement. Figure 5.6 shows both the grain size refinement and elongated grain structure after the ECAE process. Langdon et al. [118] presented the model for grain refinement in ECAE routes A, B_c and C and confirmed the formation of elongated grains when using route C in ECAE processing. The development of new refined grains is a result of gradual increase in the misorientations between subgrains that is caused by the deformation at slightly high

temperature and with further deformation, the grain size continues to decrease and the amount of newly generated ultrafine grains increase.

TEM images and diffraction patterns showed that ECAE has no real effect on martensite twinning mode observed in TiNiPd alloys. The diffraction patterns taken from the twins demonstrate the common twinning modes in TiNi based shape memory alloys. In the literature, none of the previous works showed one of the compound twinning modes in TiNiPd SMAs which are occasionally observed in NiTi binary alloys. Madangopal et al. stated that (001) plane cannot be a twinning plane in B19 martensite as it is a mirror plane of the orthorhombic structure [126]. Similarly, in this study, no traces of compound twins were detected even after ECAE, although in the binary, compound twins are in abundance after ECAE. ECAE parameters used in this study affect neither the twinning mode nor the twin size in NiTiPd. It is known that B19 martensite exists in TiNiPd alloys, which is of higher symmetry than B19'. Therefore there are less variants in B19 martensite than in B19' martensite of binary NiTi. This leads to difficulties in the accommodation of the transformation strain as effectively as that in B19' martensite, which might be the reason why compound twinning does not exist.

5.8.2 Effect of ECAE Processing on Martensitic Transformation Temperatures

It is quite interesting to observe excellent thermal cyclic stability of the transformation temperatures in solutionized $Ti_{50}Ni_{30}Pd_{20}$ and hot rolled $Ti_{50.3}Ni_{33.7}Pd_{16}$ samples without application of any thermo-mechanical treatment. Previous studies on equiatomic NiTi and TiNiHf alloys [9, 13] showed that thermal stability of transformation temperatures is improved after thermo-mechanical treatments. It is found that addition of Hf to NiTi alloys leads to the degradation of thermal cyclic stability due to the decrease in critical shear stress for slip [132]. On the contrary, the results of DSC experiments of TiNiPd alloys in this study showed that addition of Pd to TiNi alloys improves the thermal cyclic stability possibly due to increase in critical shear stress for slip and to the improvement in the geometrical lattice compatibility between austenite

and martensite upon Pd addition similar to Cu addition [133]. The rationale of the improvement of geometrical compatibility will be discussed extensively in Chapter VI.

The decrease in transformation temperatures after ECAE in stress free DSC experiments can be explained using the same approach introduced in section 4.8.2. From Figure 5.3, the transformation temperatures decrease after ECAE process due to the increase in irreversible energy. This increase in irreversible energy can be attributed to the increase in strength levels via grain refinement and dislocation density. In such a microstructure multiple phase fronts should be nucleated and propagated which would require more energy (i.e., reduction in the transformation temperature) and more energy dissipation due to both difficulty of propagation of and interaction between multiple phase fronts, but especially due to the later. Grain boundaries and high dislocation density act as barriers to the transforming interfaces and require the nucleation of new phase fronts. However, note that above is only valid at stress-free conditions. Under applied stress, the situation is slightly different. From isobaric cooling-heating experiments in section 5.5, the transformation temperatures increase under the influences of the external stress. The increase is proportional to the applied stress according to the equation 4.8.2.3.

The decrease in thermal hysteresis upon Pd addition can be explained using the same approach for the explanation of improved thermal cyclic stability in stress free DSC experiments. The geometric lattice compatibility between austenite and martensite is improved upon Pd addition. This improvement leads to decrease in the required energy for the propagation of phase front, thus the decrease in dissipation energy for the phase front propagation leads to a decrease in thermal hysteresis. Thermal hysteresis increases after ECAE due to the grain size refinement and the increase in dislocation density. Grain boundaries and high dislocation density act as barriers to the transforming interfaces and require the nucleation of new phase fronts. Thus, additional energy is required to overcome this energy barrier. The temperature must be raised above the transformation temperature on heating and lowered below on cooling. This leads to an increase in thermal hysteresis.

Thermal hysteresis extracted from isobaric cooling-heating experiments alters from the expected behavior. Thermal hysteresis of all samples initially decreases under 50MPa and the increases upon increasing the external stress. The rationale behind the initial decrease is not clear at this point. However, the increase in thermal hysteresis with the increase in external stress levels is due to the increase in dislocation density under higher stress levels. The dislocations introduced due to thermal cycling under stress act as barriers to the transforming interface which leads to a further increase in the energy to overcome this energy barriers. Thus, thermal hysteresis increases as the external stress level increases.

5.8.3 Effect of ECAE on Monotonic Mechanical Response under Tension

The increase in yield strength of martensite (σ_y) and the increase in the stress differential between yield strength and critical stress to induce martensitic transformation ($\sigma_y - \sigma_{SIM}$) of ECAE processed $Ti_{50.3}Ni_{33.7}Pd_{16}$ samples as compared to the hot rolled sample in the same thermodynamic conditions can be attributed to the grain size refinement and the increase in dislocation density. The grain refinement and the increase in dislocation density after ECAE were clearly shown in the TEM micrographs in Figure 5.2 and Figure 5.4, respectively.

5.8.4 Effect of ECAE on Fracture Strength, Cyclic Stability and Critical Stress vs. Critical Temperature Behavior

The premature failures observed in $Ti_{50}Ni_{30}Pd_{20}$ and $Ti_{50.3}Ni_{33.7}Pd_{16}$ samples in isobaric heating-cooling experiments can be attributed to the second phase particles observed in the matrix. Karaman et al. [20] showed that Ni_4Ti_3 were found to exist in Ti-50.8at%Ni alloy after heat treatment at 450°C, but no precipitates were observed after ECAE processing at 450°C indication that the precipitates dissolved during the ECAE process or precipitates fragment into small parts such that their sizes are below the detection limit of TEM (<0.01μm). Langdon et al. [131] also studied the effect of ECAE

on precipitate size and shape and found that ECAE helps to fragment the precipitates into smaller parts and to dissolve the smaller ones in the matrix. From Figure and Table 5.3, there is a notable decrease in precipitate size and volume fraction after ECAE processing. In addition, it is observed that ECAE leads to the elimination of the porosities in the matrix. Thus, the increase of the fracture strength in isobaric heating-cooling experiments can be attributed to the decrease in the precipitate size and volume fraction and the elimination of the porosities after ECAE, however, whichever has the most influence is not clear yet.

The stress levels at which hot rolled and ECAE processed at 450°C $Ti_{50.3}Ni_{33.7}Pd_{16}$ samples failed in isobaric heating-cooling experiments are lower than the fracture stress levels obtained from the monotonic failure experiments. The failures in isobaric experiments occurred during cooling at which the austenite is transforming to martensite. This might be due to the fact that B19 martensite is of higher symmetry than B19' martensite. Therefore, there are less variants in B19 martensite than in B19' martensite of binary NiTi. This leads to difficulties in the accommodation of the transformation strain as effectively as that in B19' martensite [134].

In the isobaric thermal cyclic experiments the transformation strains of the ECAE processed and hot rolled samples increase as the level of externally applied stress increase as shown in Figure 5.13. The externally applied stress favors certain variants over the others upon phase transformation [135]. This helps the formation of the martensitic variant with the most favorable orientation (single variant martensite morphology) instead of self accommodation morphology, and thus leads to external shape change. Note that, the transformation strain levels of ECAE processed $Ti_{50}Ni_{30}Pd_{20}$ are higher than that of the solutionized sample under 50, 100 and 150MPa. It was also observed that Clausius-Clapeyron (CsCl) slopes of ECAE processed $Ti_{50}Ni_{30}Pd_{20}$ samples are lower than that of the solutionized sample. The lower CsCl slopes and higher transformation strains in ECAE processed $Ti_{50}Ni_{30}Pd_{20}$ samples can be a consequence of the local internal stress due to the favorable deformation structure formation, refinement of the grains and increased dislocation density during ECAE. The

local internal stress may help externally applied stress to bias the single variant martensite [13]. On the other hand, the transformation strain levels of ECAE processed $Ti_{50.7}Ni_{33.7}Pd_{16}$ samples are lower than that of the hot rolled $Ti_{50.7}Ni_{33.7}Pd_{16}$ sample under each stress level in isobaric heating-cooling experiments and CsCl slopes of ECAE processed $Ti_{50.7}Ni_{33.7}Pd_{16}$ samples are higher than that of hot rolled sample. The lower transformation strain levels in ECAE processed can be due to the texture formation during route B_c and B ECAE processing. This texture might be the one which gives lower transformation strain as oppose to the texture formed during route C ECAE processing. Although the texture of austenite could not be studied due to the high temperature requirement and the lack and difficulty of high temperature texture measurements it is reasonable to expect deformation texture formation in TiNiPd alloys during ECAE processing at relatively low temperatures considering the recrystallization temperature of $Ti_{50}Ni_{30}Pd_{20}$ alloy around 600°C for is considered [112].

The irrecoverable strain levels of both $Ti_{50}Ni_{30}Pd_{20}$ and $Ti_{50.3}Ni_{33.7}Pd_{16}$ decrease after ECAE which can be attributed to the increase in the difference between the yield strength of stress induced martensite and the critical stress to induce martensite. This increase in stress difference leads to an increase in critical shear stress for slip due to the grain size refinement and the increase in dislocation density. This conclusion is also consistent with recent the results from the NASA Glenn group [32]. They also found that TiNiPd alloys with lower Pd content show less permanent deformation since the strength of austenite is very much higher than the strength of martensite such that transformation from martensite to austenite occurs without slip formation [34].

In Figure 5.14.a, extrapolating σ_{SIM} curve of the $Ti_{50}Ni_{30}Pd_{20}$ samples gives lower temperatures at 0MPa than that of the M_s temperatures measure from DSC. On the other hand, extrapolating σ_{SIM} curves of the $Ti_{50.3}Ni_{33.7}Pd_{16}$ samples gives approximately the same M_s temperatures measured using DSC. This peculiarity between the $Ti_{50}Ni_{30}Pd_{20}$ and $Ti_{50.3}Ni_{33.7}Pd_{16}$ samples might be due to the increase in elastic mismatch between austenite and martensite near M_s due to austenite softening and inelastic accommodation of this mismatch in the $Ti_{50}Ni_{30}Pd_{20}$ samples. The increase in

elastic mismatch with the increase in Pd content leads to the need for higher supercooling or higher stress levels for triggering martensite nucleis to grow in the $Ti_{50}Ni_{30}Pd_{20}$. This causes austenite to transform into martensite at a lower temperature under a given stress or at a higher stress level under a constant temperature.

CHAPTER VI

COMPARISON OF SHAPE MEMORY CHARACTERISTICS OF THERMO-MECHANICALLY PROCESSED NiTi AND TiNiPd SMAs

6.1 Preamble

NiTi alloys have become widely used in medical field and have been receiving increased attention in the aerospace, automotive, and power generation industries, especially if the application needs actuator type behavior. For example, the actuation systems in aeronautics and aerospace propulsion technologies can benefit from SMAs which have transformation temperatures higher than 150° or the SMAs that could be applicable in and around the engines of automobiles should have transformation temperatures at least 100°C to 300°C. NiTi can do work equivalent to 10-20 J/cm^3 under biased load [136] and these alloys have the ability to recover 8% strain when unconstrained [137]. Even though NiTi alloys demonstrate the best known SMAs, its undesirable cyclic instability response when unconstrained, along with large thermal and stress hysteresis and low operational temperature range in the aforementioned actuation type applications leads to investigate ternary alloy systems. The development of new ternary alloys is largely based on trial and error without a suitable guidance of theoretical approach. In one of these trial and errors, it is found that the addition of Pd and Pt increases the transformation temperatures and decreases thermal hysteresis [30, 31, 35]. However, the increase in transformation temperatures and the decrease in thermal hysteresis come at the expense of diminished work capability [32].

In this chapter, the effect of Pd addition to NiTi on the transformation temperatures, thermal hysteresis and cyclic stability response will be revealed. In addition, microstructural evolution with severe plastic deformation in $Ti_{50}Ni_{30}Pd_{20}$ and $Ni_{49.7}Ti_{50.3}$ alloys will be compared since, in the previous chapters, it is shown that, the microstructural refinement and evolution with thermo-mechanical processing have influence on the shape memory responses of both of the alloys. Although TiNiPd and

NiTi alloys can't be each others alternative for high temperature applications, it is useful to compare the shape memory response of TiNiPd with superior shape memory properties of NiTi alloys in order to show TiNiPd ternary alloys are promising for high temperature applications and it is worth while to carry out extensive research for further improvement in the shape memory and cyclic stability response of these ternary alloys.

6.2 Comparison of Microstructural Evolution in NiTi and TiNiPd alloy after ECAE

Severe plastic deformation via ECAE of the $Ni_{49.7}Ti_{50.3}$ and $Ti_{50}Ni_{30}Pd_{20}$ showed that grain size refinement of these alloys was different. The average grain size of the $Ni_{49.7}Ti_{50.3}$ and $Ti_{50}Ni_{30}Pd_{20}$ alloys before ECAE process was determined as 50μm using optical microscope (OM) images and the OM images of hot rolled $Ni_{49.7}Ti_{50.3}$ and solutionized $Ti_{50}Ni_{30}Pd_{20}$ alloys were demonstrated in Figure 4.2 and 5.5, respectively. Figure 6.1 represents the grain size reduction in both of these alloys after ECAE processing at 400°C. It was found that the average grain size of the $Ni_{49.7}Ti_{50.3}$ sample ECAE processed at 400°C is 100nm, on the other hand, the grains in the $Ti_{50}Ni_{30}Pd_{20}$ sample ECAE processed at 400°C are elongated and the average length and width of the grains are 0.5 and 1μm, respectively. Thus, the grain size refinement using ECAE in TiNiPd is not as pronounced as that of in NiTi alloy.
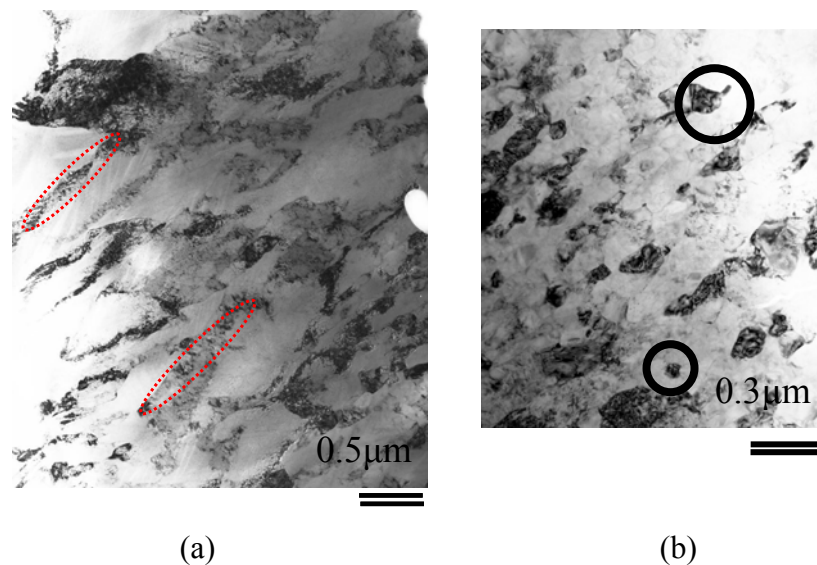
Figure 6.1 Bright field TEM images taken above A_f temperature of the samples showing the grain size reduction due to ECAE processing, (a) $Ti_{50}Ni_{30}Pd_{20}$ ECAE 4C at 400°C, and (b) $Ni_{49.7}Ti_{50.3}$ ECAE 4B_c at 400°C.

The mechanism of grain refinement is the continuous dynamic recovery/recrystallization as mentioned in section 4.8 and 5.8. Severe plastic deformation using ECAE at slightly high temperatures causes the development of new grains as a result of gradual increase in the misorientations between the subgrains. Further deformation reduces the grain size continuously and the volume fraction of newly generated ultrafine grains increases. Thus, there should be another mechanism which restricts the misorientation increase between the subgrains. It was found that, there are Ti rich $Ti(C, O)$ and $Ti_2(Ni, Pd)$ precipitates in TiNiPd alloy as mentioned in section 5.6. These precipitates might play a role during grain size reduction such as pinning the subgrains and restricting the formation new grains as a result of gradual increase in the misorientations between the subgrains. Therefore, the grain size refinement is less pronounced in TiNiPd alloys utilizing ECAE at relatively high temperatures.

Another intriguing observation is the lack of formation of (001) compound twins in TiNiPd alloys. From the TEM study on TiNiPd alloys, no compound twin formation was observed. However, it is realized that, (001) plane cannot be a twinning plane in B19 martensite as it is a mirror plane of the orthorhombic structure [126]. Thus, (001) compound twin formation in TiNiPd alloys which have B19 martensite structure is not possible.

6.3 The effect of Pd Addition on Transformation Temperatures, Thermal Hysteresis and Cyclic Stability of NiTi Alloys

Aforementioned studies showed that the transformation temperatures increase and thermal hysteresis decrease upon Pd addition to NiTi binary alloys [33-35]. However, the effect of Pd addition on the cyclic response of NiTi as function of thermal cycles has not been shown up to date. Figure 6.2 demonstrates the increase in transformation temperatures, the decrease in thermal hysteresis and the improved stability of the transformation temperatures upon Pd addition.

The main observations upon 20at%Pd addition to NiTi alloy are, 1) The increase in M_s temperature is 55°C, 2) thermal hysteresis decreases from 36.5°C down to 12°C, and 2) there is no shift in M_s temperature after 5 cycles (improved cyclic stability).

The decrease in thermal hysteresis and improved stability of transformation temperatures can be explained by the enhancement of the geometric compatibility of the martensite-austenite upon addition of Pd [133]. Thermal hysteresis is the direct indication of the dissipation energy as mentioned in Chapter IV and V. Elastic and interfacial energy are stored owing to the presence of martensite and austenite at the transition interface because of the incompatibility between these two phases. This occurs in both austenite to martensite and martensite to austenite transformation. Thus, additional energy is required to overcome this energy barrier. In the case of thermally activated phase transformations, the temperature must be raised above the transformation temperature on heating and lowered below on cooling. This leads to an increase in thermal hysteresis. If the stored energy due to the incompatibility between austenite and

martensite is reduced, less energy is needed to overcome the dissipation energy which arises from the incompatibility. Thus, thermal hysteresis decreases upon Pd addition because of the enhanced geometrical compatibility between austenite and martensite. The improvement in the cyclic stability upon Pd addition also depends on this geometrical compatibility. If the compatibility is obtained at the transition interface dislocation formation, which suppresses M_s temperature, does not occur and this leads to cyclic stability.
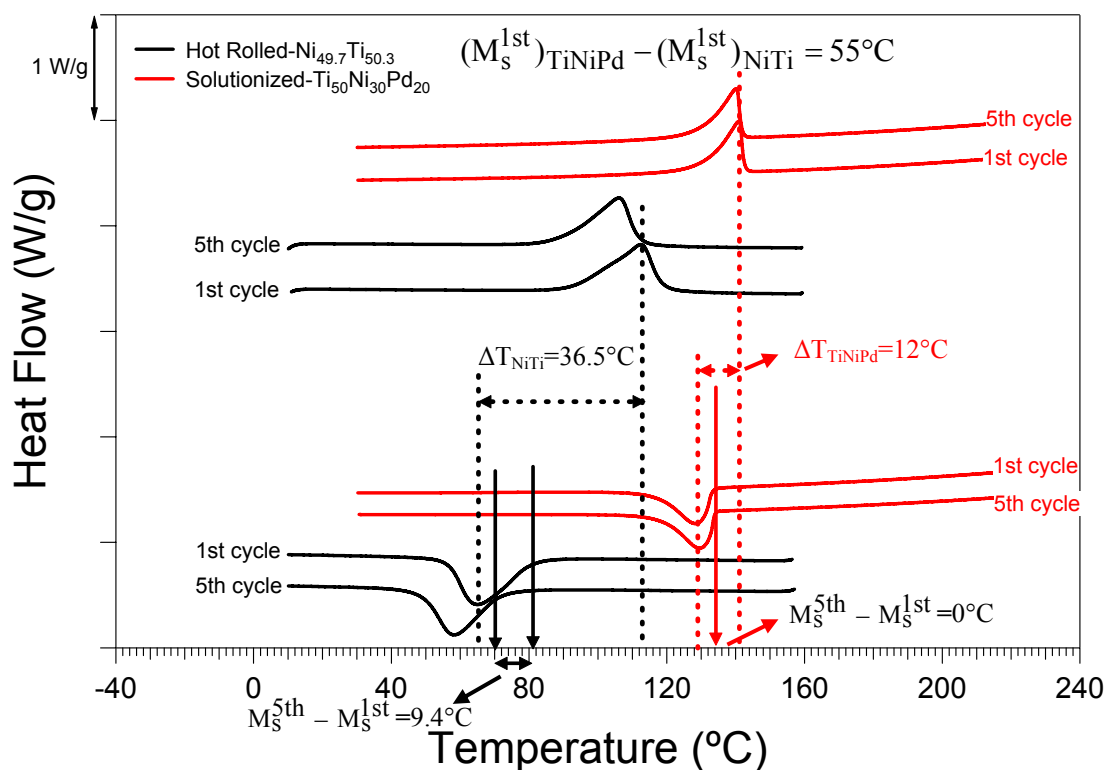
Figure 6.2 Cyclic DSC response of the hot rolled $Ni_{49.7}Ti_{50.3}$ and solutionized $Ti_{50}Ni_{30}Pd_{20}$ alloys demonstrating the increase in transformation temperatures, decrease in thermal hysteresis and improvement in the cyclic stability of the transformation temperatures upon Pd addition.

6.4 The Effect of Pd Addition on Transformation and Irrecoverable Strain Levels in Isobaric Cooling Heating Experiments

The transformation and irrecoverable strain levels of the hot rolled and ECAE processed $Ni_{49.7}Ti_{50.3}$ and solutionized and ECAE processed $Ti_{50}Ni_{30}Pd_{20}$ samples are compared in Figure 6.3. The transformation strain levels of solutionized and ECAE processed $Ti_{50}Ni_{30}Pd_{20}$ samples are lower than that of the hot rolled and ECAE processed $Ni_{49.7}Ti_{50.3}$ due to the change in lattice parameter and structure. In both of the alloys, the transformation strain level increases as the applied stress increases due to the fact that externally applied stress helps the formation of the martensitic variant with the most favorable orientation (single variant martensite morphology) instead of self accommodation morphology which leads to external shape change. The most important observation in isobaric cooling-heating experiments is the decrease in irrecoverable strain levels at each stress level upon Pd addition. No significant irrecoverable strain is observed under 200MPa in solutionized $Ti_{50}Ni_{30}Pd_{20}$ sample, on the other hand, the irrecoverable strain level of the hot rolled $Ni_{49.7}Ti_{50.3}$ sample under 200MPa is around 1%. The decrease in irrecoverable strain upon Pd addition can be attributed to the decrease in elastic modulus mismatch between austenite and martensite due to the increase in geometrical compatibility between two phases which leads to strengthening of the alloy. ECAE leads to decrease in irrecoverable strain levels in both of the alloys due to the grain size refinement and the increase in dislocation density.
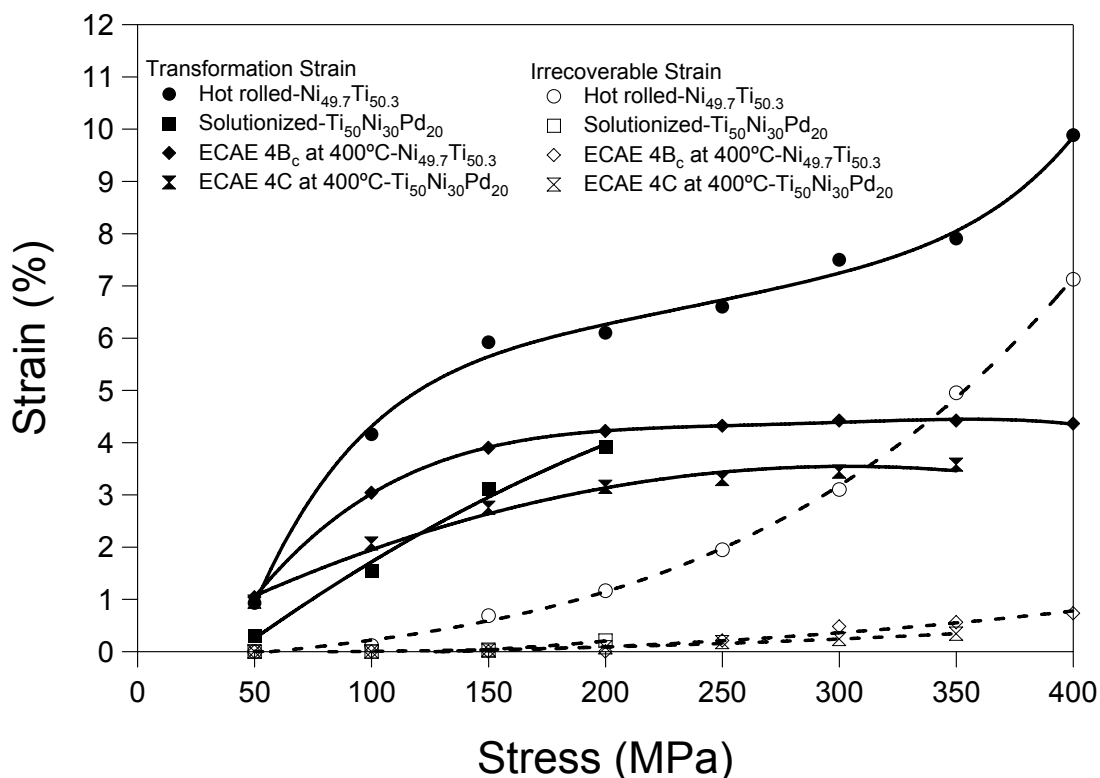
Figure 6.3 Transformation and irrecoverable strain response as a function of constant tensile stress levels in the hot rolled $Ni_{49.7}Ti_{50.3}$ and solutionized $Ti_{50}Ni_{30}Pd_{20}$ samples, ECAE processed $Ni_{49.7}Ti_{50.3}$ and $Ti_{50}Ni_{30}Pd_{20}$ samples from the isobaric cooling-heating experiments under increasing applied stress levels.

6.5 Comparison of Thermal Hysteresis in NiTi and TiNiPd Alloys

Thermal hysteresis is another important characteristic of shape memory alloys for their application since thermal hysteresis is directly related with the energy dissipation which depends on the irreversible component of the non-chemical energy in equation 4.8.2.1. There are two energy dissipative mechanisms which are the energy dissipation in the form of frictional work and the dissipation of the stored elastic energy. Frictional work is spent in resistance to interface motion during transformation. Dissipation of stored elastic energy is the relaxation of coherency strains of austenite-martensite interface.

Figure 6.4 shows the thermal hysteresis decrease with the addition of Pd in the

present materials in their initial conditions. Thermal hysteresis of the hot rolled $Ni_{49.7}Ti_{50.3}$ and the solutionized $Ti_{50}Ni_{30}Pd_{20}$ samples under 150MPa are 53°C and 17°C, respectively. Figure 6.5 represents the comparison of the thermal hysteresis after ECAE process. Thermal hysteresis of the samples $Ni_{49.7}Ti_{50.3}$ and $Ti_{50}Ni_{30}Pd_{20}$ samples ECAE processed at 400°C under 150MPa are 45°C and 18°C, respectively. The thermal hystresis of $Ni_{49.7}Ti_{50.3}$ sample decreases after ECAE which can be attributed to the improved elastic modulus compatibility of austenite-martensite interface. The improved compatibility is a result of the strengthening due to grain size refinement and accommodation of the lattice deformation mostly elastically. The effect is opposite in the TiNiPd alloy. However, the increase in thermal hysteresis of TiNiPd alloys is not significant.
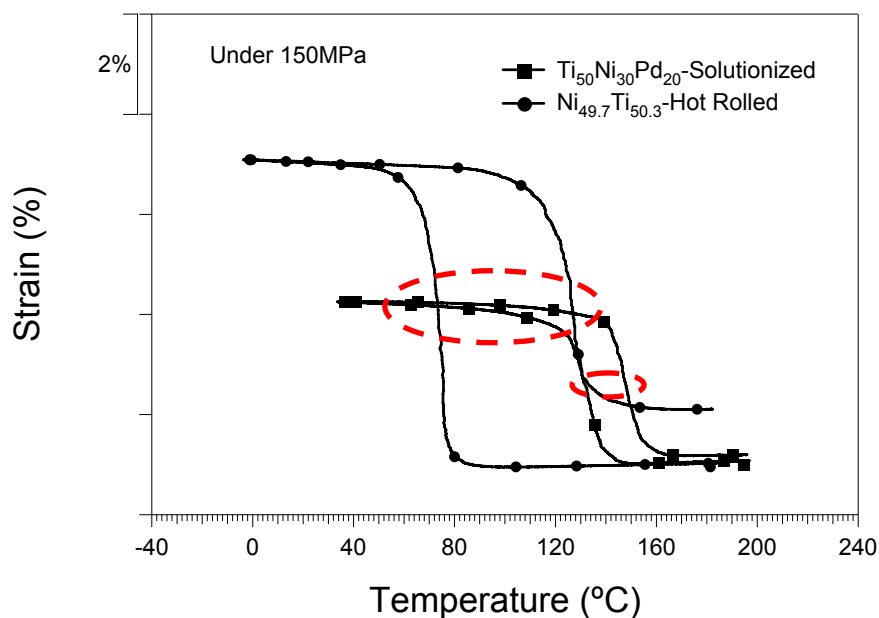
Figure 6.4 Comparison of the thermal hysteresis of the hot rolled $Ni_{49.7}Ti_{50.3}$ and the solutionized $Ti_{50}Ni_{30}Pd_{20}$ samples.
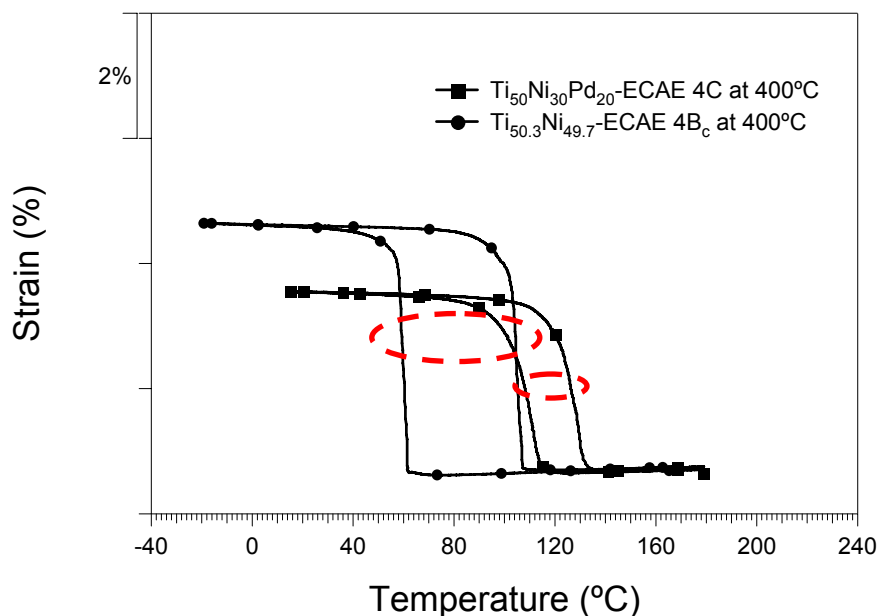
Figure 6.5 Comparison of the thermal hysteresis of the $Ni_{49.7}Ti_{50.3}$ and $Ti_{50}Ni_{30}Pd_{20}$ samples ECAE processed at 400°C.

6.6 Comparison of the Work Outputs in NiTi and TiNiPd Alloys

The performance of a thermally activated actuator material is dependent on the work output of the alloy which is the product of recoverable strain and the applied stress. In real applications of high temperature shape memory alloys, the material must be able to perform work against an externally applied load in order to function properly. The recoverable strain is obtained by subtracting the irrecoverable strain from transformation strain. The transformation and irrecoverable strains are defined in Figure 4.10.

The work outputs under constrained stress levels of the hot rolled $Ni_{49.7}Ti_{50.3}$ and solutionized $Ti_{50}Ni_{30}Pd_{20}$ alloys were calculated and shown in Figure 6.6. The effect of ECAE on the work outputs of the alloys is represented in Figure 6.7.
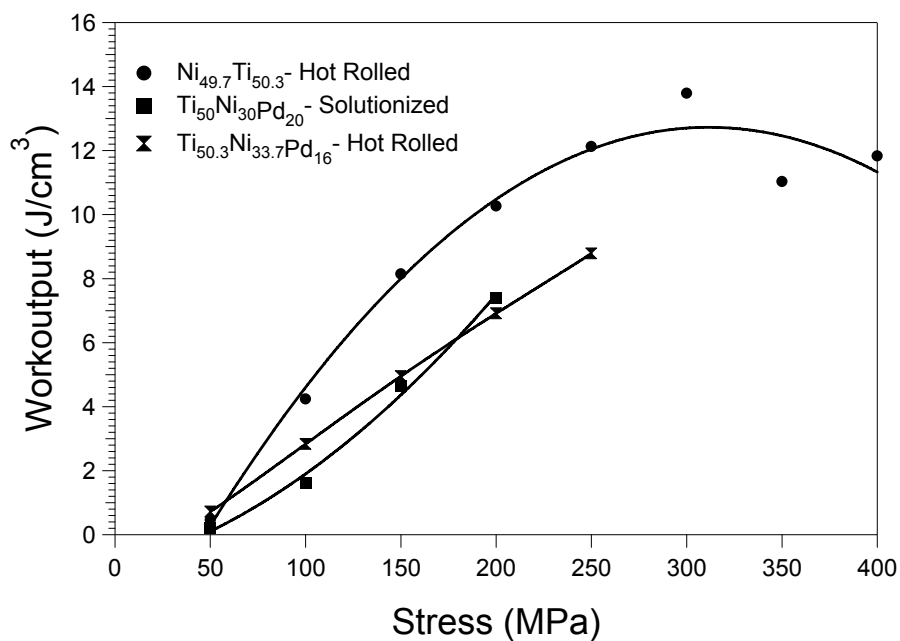
Figure 6.6 Work output as a function of applied stress in hot rolled $Ni_{49.7}Ti_{50.3}$, solutionized $Ti_{50}Ni_{30}Pd_{20}$, and hot rolled $Ti_{50.3}Ni_{33.7}Pd_{16}$ alloys.
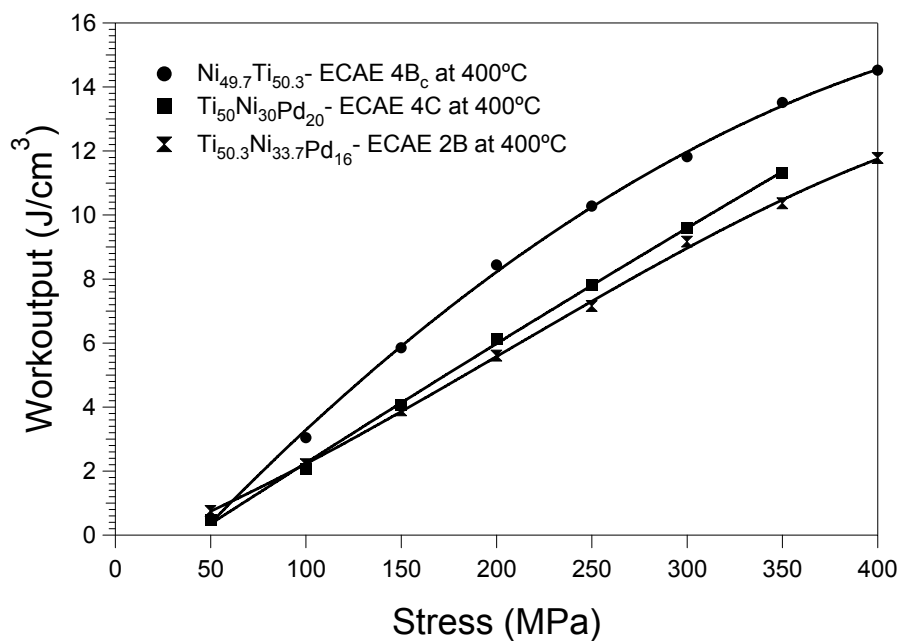
Figure 6.7 Work output as a function of applied stress in the ECAE processed $Ni_{49.7}Ti_{50.3}$, $Ti_{50}Ni_{30}Pd_{20}$ and $Ti_{50.3}Ni_{33.7}Pd_{16}$ samples.

In Figure 6.6, work output of the hot rolled $Ni_{49.7}Ti_{50.3}$ increases with increasing stress up to 300MPa, because the higher stresses cause martensite variants to reorient to form a single martensite variant at the expense of the others, therefore there is more strain available to be recovered during the transition to austenite which leads an increase in the work output level. However, above 300MPa, applied stress becomes high enough to prevent full recovery of the martensite since permanent deformation starts being more influential. Thus, the recoverable strain level begins to decrease. Since work output is the product of recoverable strain and applied stress it also starts to decrease above 300MPa. The peak stress at which the highest transformation strain, thus the recoverable strain, is attained is not observed in the TiNiPd alloys. This is due to premature failure of the alloys because of the second phase particles in the matrix.

Figure 6.7 compares the work outputs of the $Ni_{49.7}Ti_{50.3}$ and $Ti_{50}Ni_{30}Pd_{20}$ and samples which are ECAE processed at 400°C. The work outputs of the ECAE processed samples never decrease up to 400MPa and until failure for $Ni_{49.7}Ti_{50.3}$, $Ti_{50.3}Ni_{33.7}Pd_{16}$ and $Ti_{50}Ni_{30}Pd_{20}$, respectively. As the applied stress increases the work output also increases since there were no irrecoverable strains up to 200MPa and above 200MPa the levels were negligible as shown in the previous chapters. In addition, the transformation strain level does not change noticeable above a certain stress level. The work output levels decrease after ECAE since the transformation strain and the corresponding recoverable strain levels decrease due to the reasons explained in Chapter IV and V. Under 200MPa, the work output of the hot rolled $Ni_{49.7}Ti_{50.3}$ is 10.2 J/cm^3 while 8.5 J/cm^3 in ECAE processed alloy and for the solutionized $Ti_{50}Ni_{30}Pd_{20}$, the work output is 7.4 J/cm^3 and reduces down to 6.2 J/cm^3. One intriguing finding is that higher work output values are obtained under 200MPa in the present TiNiPd alloys as compared to earlier work on the TiNiPd alloys having compositions [34]. The main difference between the samples used in the present study and in this previous work is the thermo-mechanical treatment applied. In the previous work the $Ni_{34.5}Ti_{50.5}Pd_{15}$ and $Ni_{29.5}Ti_{50.5}Pd_{20}$ alloys were extruded at 900°C which is higher than the recrystallization temperature of TiNiPd alloys. Such processing might possibly help the homogenization

of the samples, however, the grain size would be quite large and dislocation density would be low. In this study, the work output under 200MPa for the $Ti_{50}Ni_{30}Pd_{20}$ ECAE processed at 400°C is 6.2 J/cm^3, notably higher than what has been reported before. This might be due to refined grain size and high dislocation density which lead to decrease in irrecoverable strain under stress.

In addition to work output analysis, it is very useful to calculate the available energy efficiency in the design and development of SMA actuators. The proportion of Carnot efficiency in practical engines is 60% and the way of improving the energy efficiency of an engine is to increase the Carnot efficiency (i.e. by extension of the difference in temperature sources of heat between which the engine operates) [138]. The energy efficiency of an SMA engine is theoretically restricted by Carnot efficiency since an SMA actuator is a heat engine works at low temperature. Application of stress forces the martensitic transformations to occur at higher temperatures and provides a method to increase the Carnot efficiency although the onset of slip above critical stress imposes a critical limit. The Carnot efficiency of an SMA engine is a function of the dependence of transformation temperatures on the applied stress and can be represented as:

$$\eta = \frac{A_f(\sigma_{max}) - M_f(\sigma \to 0)}{A_f(\sigma_{max})} \tag{6.6.1}$$

where:

$$A_f(\sigma_{max}) = A_f(\sigma = 0) + \sigma \frac{dA_f}{d\sigma} \tag{6.6.2}$$

The equation shown below can be derived from equations 6.6.1 and 6.6.2:

$$\eta = 1 - \frac{M_f(\sigma \to 0)}{A_f(\sigma = 0) + \sigma_{max} \frac{dA_f}{d\sigma}} \tag{6.6.3}$$

$\dfrac{dA_f}{d\sigma}$ can be found as the ratio of the change in the strain and entropy during the transformation. Strain can be evaluated from the strain vs temperature curves, however, the entropy change is more elusive because it is not reproducible due to a range of orthogonality resulting from the occurrence of differently deformed crystals in polycrystalline SMAs [138]. Therefore, $\dfrac{dA_f}{d\sigma}$ can be determined from the slopes of

stress vs A_f temperature curves. Using the equation 6.8, the transformation temperatures from differential scanning calorimetry results and A_f dependence on the applied stress levels, the Carnot efficiencies are calculated for the hot rolled $Ni_{49.7}Ti_{50.3}$ and $Ti_{50.3}Ni_{33.7}Pd_{16}$, solutionized $Ti_{50}Ni_{30}Pd_{20}$ alloys and for all materials ECAE processed at 400°C. The comparison of the Carnot efficiencies of all materials before and after ECAE is represented in Figure 6.8.
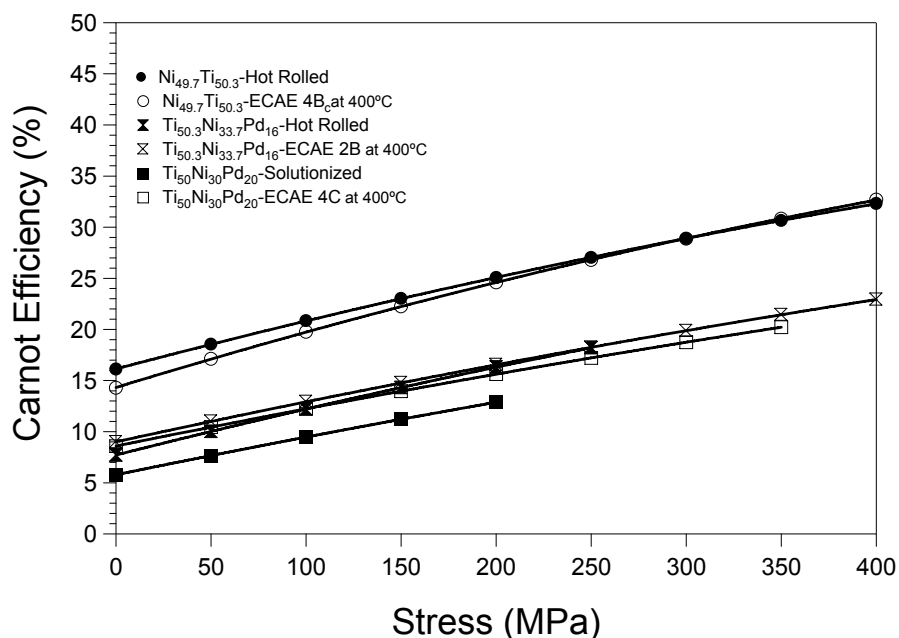
Figure 6.8 Carnot efficiencies of $Ni_{49.7}Ti_{50.3}$, $Ti_{50.3}Ni_{33.7}Pd_{16}$ and $Ti_{50}Ni_{30}Pd_{20}$ before and after ECAE.

It was shown that the Carnot efficiencies increase after ECAE in TiNiPd samples which might be due to the increase in resistance to dislocation formation by increasing the stress differential between yield strength of martensite and critical stress to induce martensite. Since the applied stress forces the martensitic transformation to occur at higher temperatures the Carnot efficiencies increase with the increase in applied stress levels in all alloys. The Carnot efficiencies of the TiNiPd samples are lower than that of NiTi alloy because of the lower transformation strain levels.

TiNiPd alloy can be considered as a very good candidate for high temperature shape memory applications in the light of the results presented in this chapter.

Transformation temperatures increase, thermal hysteresis and irrecoverable strains decrease with the addition of Pd to NiTi binary shape memory alloys. In addition, work outputs and the Carnot efficiencies of the TiNiPd alloys used in this study are close to the work outputs and Carnot efficiencies compiled from equiatomic NiTi alloy at higher temperatures. The increase in transformation temperatures with the addition of Pd does not come at the expense of diminished work capability. TiNiPd alloys demonstrate good work capability with dimensional stability under thermal cycling conditions, especially after ECAE process.

CHAPTER VII

SUMMARY OF THE RESULTS AND CONCLUSIONS

The present work investigated the effect of severe plastic deformation via ECAE on the microstructural refinement and dislocation substructure, and the corresponding evolution in the mechanical properties such as yield strength and stress differential between the yield strength of martensite and critical stress for stress induced martensitic transformation of $Ni_{49.7}Ti_{50.3}$, $Ti_{50}Ni_{30}Pd_{20}$ and $Ti_{50.3}Ni_{33.7}Pd_{16}$ shape memory alloys. The effect of microstructural evolution such as grain refinement, deformation twinning induced refinement and dislocation density increase the transformation temperatures, transformation temperature interval and thermal hysteresis under isobaric conditions was revealed. Possible effects of microstructural evolution on the transformation thermodynamics, in particular the elastic and irreversible energy, were introduced and their ramifications on the shape memory properties such as transformation and irrecoverable strain levels and thermal hysteresis were discussed. Thermal cyclic stability responses of the ECAE processed and unprocessed alloys at stress free and under isobaric conditions were investigated. The isobaric thermal cyclic stability of transformation temperatures, thermal hysteresis, transformation and irrecoverable strain levels of unprocessed and ECAE processed $Ni_{49.7}Ti_{50.3}$, $Ti_{50}Ni_{30}Pd_{20}$ and $Ti_{50.3}Ni_{33.7}Pd_{16}$ SMAs was compared. The effect of ECAE on the premature failure of the TiNiPd alloys was investigated. The evolution in transformation temperatures, thermal hysteresis, irrecoverable strain levels and the corresponding work outputs of the NiTi alloy with the addition of Pd was also revealed. Due to the limited ductility of the alloys which is partially a consequence of their purity level, $Ni_{49.7}Ti_{50.3}$ alloy was ECAE processed at 400°C, 425°C and 450°C for four passes and at a relatively lower temperature, i.e. 300°C, for one pass, $Ti_{50}Ni_{30}Pd_{20}$ alloy was ECAE processed at 400°C, and 600°C for four passes and at 500°C for two passes and $Ti_{50.3}Ni_{33.7}Pd_{16}$ alloy was ECAE processed at 450°C for four passes and 400°C for two passes.

The following conclusions can be drawn from the study on $Ni_{49.7}Ti_{50.3}$ alloy:

1) It is shown that severe plastic deformation via ECAE can lead to grain refinement in NiTi alloys at relatively high temperatures such as 400°C and above, and deformation-twinning induced refinement at relatively low temperatures such as 300°C.

2) ECAE microstructure triggers the formation of (001) compound twins with fine platelets in martensite in addition to common $<011>$ Type II and $\{11\bar{1}\}$ Type I twins. (001) compound twinning with fine platelet is selected as an internal martensite defect to minimize the transformation energy in nanograins, although it does not result in a solution to the crystallographic theory of martensitic transformation.

3) Grain refinement via ECAE led to R-phase stabilization in some of the submicron/nanosize grains.

4) The transformation temperatures at stress free condition decrease while the thermal cyclic stability of them is improved after ECAE process due to high dislocation density and grain refinement.

5) The transformation temperature interval, which is the indication of stored elastic energy, decreases in the ECAE processed NiTi due to the increase in energy dissipation. The increase in energy dissipation causes an increase in thermal hysteresis.

6) ECAE leads to an increase in strength differential between the critical stress to induce martensite and the yield stress of martensite upon grain refinement and dislocation substructure formation.

7) ECAE improves the thermal cyclic stability of transformation temperatures, thermal hysteresis and transformation strains and significantly reduces irrecoverable strain levels under constant stress. The negligible irrecoverable strain levels even under very high stress levels in the samples ECAE processed at 300°C and 400°C is attributed to the increase in critical stress level for dislocation slip due to grain size and deformation twinning-induced refinement via ECAE.

The following conclusions can be drawn from the study on $Ti_{50}Ni_{30}Pd_{20}$ and $Ti_{50.3}Ni_{33.7}Pd_{16}$ alloy:

1)   Severe plastic deformation via ECAE refines the grains down to submicron size and increase the dislocation density in the $Ti_{50}Ni_{30}Pd_{20}$.

2)   Pd addition to NiTi alloy significantly increases transformation temperatures and decreases thermal hysteresis. The enhancement of lattice compatibility between transforming phase upon addition of Pd and less need for plastic accommodation and energy dissipation is the reason for shrinking thermal hysteresis. The transformation temperatures of ternary alloys decrease and thermal hysteresis increases after ECAE due to the grain refinement and increase in dislocation density.

3)   Unexpected premature failures are observed in non-SPD processed $Ti_{50}Ni_{30}Pd_{20}$ and $Ti_{50.3}Ni_{33.7}Pd_{16}$ alloys in isobaric cooling-heating experiments due to the presence of Ti-rich Ti(C, O) and Ti_2(Ni, Pd) precipitates in the matrix. The fracture stress levels increase after ECAE due to the fact that fragmentation and partial dissolution of the precipitates. The increase in fracture stress levels is also due to the elimination of large pores observed in the solutionized $Ti_{50}Ni_{30}Pd_{20}$ sample after ECAE.

4)   Addition of Pd to NiTi alloy enhances thermal cyclic stability of transformation temperatures and thermal hysteresis at stress free conditions.

5)   It also decreases irrecoverable strain levels under isobaric heating-cooling.

6)   ECAE improves the thermal cyclic stability notably by further reducing and stabilizing the irrecoverable strain levels under isobaric heating-cooling. This is due to the increase in critical stress for dislocation slip upon grain size refinement and dislocation density increase via ECAE.

7)   The work output of NiTi alloys decreases with the addition of Pd due to the decrease in transformation strain.

8)   TiNiPd alloys are very good candidates for high temperature shape memory applications due to the fact that transformation temperatures increase, thermal hysteresis and irrecoverable strain decrease, the former two are due to the Pd addition and the later is due to microstructural refinement via ECAE.

9)   TiNiPd alloys in this study demonstrate good work capability and dimensional stability under thermal cyclic conditions, especially after ECAE.

Therefore, it can be concluded that the increase in transformation temperatures with the addition of Pd does not come at the expense of diminished work capability with the help of microstructural refinement.

CHAPTER VIII
FUTURE WORK

ECAE processing leads to thermo-mechanical strengthening by increasing critical shear stress for slip via grain size refinement and increase in dislocation density. ECAE processed shape memory alloys show cyclic thermal cyclic stability under no load and biased load conditions. The parameter for thermal cyclic stability includes stable transformation temperatures, transformation and irrecoverable strain and thermal hysteresis as a function of the number of cycles. ECAE has advantages in terms of ease of processing, control on grain morphology, evolution of microstructure and formation of specific texture. In addition, ECAE permits the application of large amount of uniform strain without changing the cross section of the work piece. However, in this study, the limited ductility of TiNi, especially very low ductility of TiNiPd alloys made ECAE processing challenging. In the light of the results gathered in this study, future recommendations can be divided into three different parts: recommendations on (1) severe plastic deformation and post processing treatments, (2) different ternary alloys, and, (3) characterization experiments.

1) Recommendations on severe plastic deformation and post processing treatments:

1) Higher number of passes following different routes can be conducted at different temperature ranges such as from room temperature to 300°C.

2) Marforming (deformation in martensite) via ECAE can be conducted on extremely pure alloys due to ductility limitations. Marforming might be a more efficient method in microstructural refinement.

3) The effect of cold rolling after ECAE can be studied to investigate the effectiveness strain path changes on the microstructural evolution and corresponding change in the shape memory characteristics of the NiTi and TiNiPd alloys.

4)   Low temperature annealing after ECAE should be investigated on TiNiPd alloys because it was found in our previous study that short time low temperature annealing improves the thermal cyclic stability of TiNiHf shape memory alloys due to the rearrangement of dislocations upon annealing, polygonization and/or vacancy/interstitial pair formation [19].

5)   Large diameter billets can be used to obtain large product cross sections not to have difficulties of having limited number of samples for experimentation.

6)   Lubrication of the work piece is a very important parameter in ECAE processing in terms of decreasing the friction between the die walls and the work piece. Different high temperature lubricants should be searched and evaluated in terms of improvement in the ECAE performance.

2) Recommendations on different ternary alloys:

1)   TiNiPd alloys with different compositions can be investigated considering different target applications (target transformation temperatures). Addition of different amounts of Pd definitely changes the shape memory behavior of the TiNiPd alloys.

2)   In this study, the second phase particles in the TiNiPd alloys were the most challenging problem in terms of processability of the alloys and the resulting shape memory response due to their brittle nature. Therefore, TiNiPd alloys should be obtained from another source which provides more clean alloys in terms of oxygen and carbon contents.

3)   TiNiPt ternary alloy system which is another promising high temperature shape memory alloy system can be ECAE processed and then compared with the TiNiPd alloys.

3) Recommendations on characterization experiments:

1)   One of the expected consequences of using different ECAE routes is certain texture evolution. Thus, it should be examined and the effect of texture on the shape memory characteristics of NiTi and TiNiPd alloys should be investigated.

2)   Monotonic response of the alloys should be determined for investigating the deformation behavior of martensite and austenite at different temperatures.

3)   Pseudoelastic cyclic behavior of TiNiPd alloys should be investigated. There is no report of high temperature pseudoleasticity in these alloys, thus, it is a great interest to find out the effect of ECAE on whether high temperature pseudoelasticity would be possible in ECAE processed NiTiPd alloys.

4)   Incremental strain loading experiments in other words, incremental step loading experiments should be conducted to investigate the evolution of irrecoverable strain which is the amount of strain remaining in the sample after loading to a particular strain and then unloading back to zero stress at a constant temperature and to determine the permanent strain which is the amount of this irrecoverable strain remaining after the sample is thermally cycled at zero stress. The irrecoverable and permeanent strain values could be different at each cycle unless the irrecoverable strain is zero after unloading. This experimental technique could be useful in understanding the reason of irrecoverable strain observed in thermal cyclic experiments in this study whether it is due to slip or due to retained martensite after heating the sample above A_f temperature.

REFERENCES

[1]   Otsuka K, Wayman CM. Shape Memory Materials. London: Cambridge University Press; 1998.

[2]   Melton KN. In: Duerig TW, Melton KN, Stöckel D, Wayman CM. editors. Engineering Aspects of Shape Memory Alloys. Boston: Butterworth-Heinemann Ltd; 1990.

[3]   Duerig T, Pelton A, Stockel D. Mater Sci Eng A 1999;273-275:149.

[4]   Miyazaki S. Engineering Aspects of Shape Memory Alloys. Boston: Butterworth-Heinemann Ltd; 1990.

[5]   Miyazaki S, Imai T, Igo Y, Otsuka K. Metall Trans 1986;17A:115.

[6]   Lexcellent C, Bourbon G. Mech of Mat 1996;24:59.

[7]   Tobushi H, Iwanaga N, Tanaka K, Hori T, Sawada T. Cont Mech Therm 1991;3:79.

[8]   Miller DA, Lagoudas DC, Mat Sci and Engr A 2001;308:161.

[9]   Kockar B, Karaman I, Kulkarni A, Chumlyakov Y, Kirieva IV. J of Nuclear Mater 2007;361:298.

[10]   Wada K, Liu Y, Smart Mater Struct 2005;14:273.

[11]   Tanaka K, Hayashi T, Itoh Y, Tobushi H. Mechanics of Materials 1992;13:207.

[12]   Sehitoglu H, Hamilton R, Maier HJ, Chumlyakov Y. J. Phys. IV France 2005;115:3.

[13]   Kockar B, Karaman I, Kim JI, Chumlyakov Y. Scripta Mater 2006;54:2208.

[14]   Hornbogen E. J of Mat Sci 1999;34:599.

[15]   Gall K, Maier HJ. Acta Mater 2002;50:4643.

[16]   Hornbogen E, Mertinger V, Wurzel D. Scripta Mater 2001;44:171-178.

[17]   Gall K, Sehitoglu H, Anderson R, Karaman I, Chumlyakov YI. Mat Sci and Engr A 2001;317:85.

[18]   Miyazaki S, Igo Y, Otsuka K. Acta Metall 1986;34:2045.

[19]   Gall K, Sehitoglu H, Chumlyakov YI, Kireeva IV. Acta Mater 1999;47:1203.

[20]   Karaman I, Kulkarni A, Luo ZP. Philos Mag 2005;85:1729.

[21]   Segal VM, Hartwig KT, Goforth RE. Mat Sci and Engr A 1997;224:107.

[22]   Valiev RZ, Islamgaliev RK, Alexandrov IV. Progress in Mat Sci 2000;45:103.

[23]   Moberly WJ, Proft JL, Duerig TW. Acta Metal Mater 1990;38:1601.

[24]   Waitz T, Antretter T, Fischer FD, Simha NK, Karnthaler HP. J of the Mech and Phys of Solids 2007;55:419.

[25]   Waitz T, Kazykhanov V, Karnthaler HP. Acta Mater 2004;52:137.

[26]   Waitz T. Acta Materialia 2005;53:2273.

[27]   Pushin VG, Stolyarov VV, Valiev RZ, Kourov NI, Kuranova NN, Prokofiev EA, Yurchenko LI. Ann Chim Sci Mat 2002;27:77.

[28]   Sergueeva AV, Song C, Valiev RZ, Mukherjee AK. Mater Sci Eng A 2003; 339:159.

[29]   Pushin VG, Stolyarov VV, Valiev RZ, Lowe TC, Zhu YT. Mater Sci Eng A 2005;410-411:386.

[30]   Lo YC, Wu SK, Wayman CM. Scripta Metall Mater 1990;24:1571.

[31]   Eckelmeyer KH. Scripta Metall Mater 1976;10:667.

[32]   Noebe R, Padula II S, Bigelow G, Rios G, Garg A and Lerch B, SPIE Conference Proceedings: Smart Structures and Materials 2006: Active Materials; Behavior and Mechanics San Diego, CA, 2006;6170. p. 279-291.

[33]   Olier P, Brachet J.C, Bechade J.L, Foucher C, and Guenin G, J De Phys IV 1995;8:741.

[34]   Padula A, Bigelow G, Noebe R, Gaydosh D, Garg A. In: Mitchell MR, Berg B, editors. SMST 2006: Proceedings of the International Conference on Shape Memory and Superelastic Technologies. ASM International, Metals Park, OH, 2006, Article in Press.

[35]   Donkersloot HC, Van Vucht JH. J. Less-Common Mets 1970;20:83.

[36]   Lindquist PG, Wayman CM. In: Duerig TW, Melton KN, Stöckel D, Wayman CM. editors. Engineering Aspects of Shape Memory Alloys. Boston: Butterworth-Heinemann Ltd; 1990.

[37]   Cai W, Tanaka S, Otsuka K. Mat Sci Forum 2000;279:282

[38]   Yang WS, Mikkola DE. Scripta Metal Mater 1993;28:161.

[39]   Shimizu S, Xu Y, Okunishi E, Tanaka S, Otsuka K, Mitose K. Mater Lett 1998;34:23.

[40]   Goldberg D, Xu Y, Murakami Y, Morito S, Otsuka, K, Ueki T, Horikawas HM. Scripta Metall Mater 1994;30:1349.

[41]   Goldberg D, Xu Y, Murakami Y, Morito S, Otsuka K, Intermetallics 3, 35-46, 1995

[42]   Buehler W, Wang F. Ocean Eng 1960;1:105.

[43]   Kaufman L, Cohen M. Prog Met Phys 1957;7:169

[44]   Funakubo H. Shape Memory Alloys. Amsterdam: Gordon & Breach Publishing Group 1987.

[45]   Kessler H, Pitsch W. Acta Metall 1967;15:401.

[46]   Kurdjumov GV, Khandros LG. Dokl Nauk SSSR 1949;66:211.

[47]   Saburi T, Nenno S. In: Aaronson HI, Laughlin DE, Sekerka RE, Wayman CM, editors. Proc Int Conf Solid-Solid Phase transformations, Warrendale, PA: AIME, 1981.

[48]   Otsuka K, Shimizu K. Int Metals Rev 1986;31:93.

[49]   Wang FE, Buehler WJ. Appl Phys Letter 1972;21:105.

[50]   Nagasawa A, Enami K, Ishino Y, Abe Y, Nenno S. Scripta Metall 1974;8:1055

[51]   Saburi T, Nenno S, Scripta Metall 1974;8:1363

[52]   Takezawa T, Sato S. Proc 1st JIM Int Symp on new aspects of Martensitic Transformations, Suppl. Trans JIM 1976;17:233.

[53]   Schroeder TA, Wayman CM. Scripta Metall 1977;11:225.

[54]   Ren X, Otsuka K. Phys Rev Lett 2000;85:1016.

[55]   Buehler WJ, Wiley RC, Gilfrich JV. J of Appl Phys 1963;34:1475.

[56]   Mulder JH. Ph.D Dissertation, University of Twente, Netherlands;1995.

[57]   Font J, Cesari E, Muntasell J, Pons J. Mat Sci and Engr A 2003;354:207.

[58]   Segui C, Cesari E, Van Humbeeck J. J Mat Trans JIM 1990;31:375.

[59]   Pops H, Massalski TB. Trans AIME 1964;230:1662.

[60]   Husain SW, Clapp PC. J Mater Sci 1987;22:2351.

[61]   Miyazaki S, Kawai T, Otsuka K. J De Phys 4 1982;43:813.

[62]   Oishi K, Brown LC. Metall Trans 1971;2:1971.

[63]   Miyazaki S, Otsuka K, Sakamoto H, Shimizu K. Trans Jpn Inst Metals 1981; 22:244.

[64]   Sakamoto H, Shimizu K. Trans Jpn Inst Metals 1986;27:601.

[65]   Laves F, Wallbaum HJ. Naturwissenschaften 1939;27:674.

[66]   Poole DM, Hume-Rothery. J Ist Met (Trans AIME) 1954;83:473.

[67]   Duwez P, Taylor JL. Trans AIME 1950;188:1173.

[68]   Purdy GR, Parr JG. Trans AIME 1961;221:636.

[69]   Wasilewski RJ, Butler SR, Hanlon JE, Worden D. Metall Trans 1971;2:229.

[70]   Nishida M. Wayman CM, Honma T. Metall Trans 1986;17A:1505.

[71]   Massalski TB, Okamoto H, Subramanian PR, Kacprzak L, editors. Binary alloys phase diagrams, 2nd edition, vol.3. Materials Park, OH: ASM International; 1990.

[72]   Ishida A, Sato M, Takei A, Miyazaki S, Mater Trans JIM 1995;36:1349.

[73]   Otsuka K, Ren X. Progress in Materials Science 2005;50:511.

[74]   Miyazaki S, Otsuka K. Metall Trans 1986;17A:53.

[75]   Khachin VN, Paskal YI, Gunter VE, Monasevich AA, Sivokha VP. Phys Met Metallogr 1978;46:49.

[76]   Salamon MB, Meichle ME, Wayman CM. Phys Rev B 1985;31:7306.

[77]   Miyazaki S, Ohmi Y, Otsuka K, Suzuki Y. J De Phys 4 1982;43:255.

[78]   Miyazaki S, Otsuka K. Philos Mag A 1984;50:393.

[79]   Hwang CM, Wayman CM. Scripta Metall 1983;17:381.

[80]   Miyazaki S, Otsuka K, Wayman CM. Acta Metall 1989;37:1873.

[81]   Miyazaki S, Ishida A. Mat Sci and Engr A 1999;273-275:106.

[82]   Frick CP, Ortega AM, Tyber J, Maksound AEM, Maier HJ, Liu Y, Gall K, Mat Sci and Engr A 2005;405:34.

[83]   Knowles KM, Smith DA. Acta Metall 1981;29:101.

[84]   Zheng YF, Huang BM, Zhang JX, Zhoa JX, Mat Sci and Engr A 2000;279:25.

[85]   Otsuka K, Sawamura T, Shimizu K. Phys Statu Solidi 1971;5:457.

[86]   Gupta SP, Johnson AA. Trans JIM 1973;14:292.

[87]   Onda T, Bando Y, Ohba T, Otsuka K. Mater Trans JIM 1992;33:354.

[88]   Nishida M, Ii S, Kitamura K, Furukawa T, Chiba A, Hara T, Hiraga K. Scripta Mater 1998;39:1749.

[89]   Nishida M, Yamauchi KK, Itai I, Ohgi H, Chiba A. Acta Metall Mater 1995;43:1229.

[90]   Kudoh Y, Tokonami M, Miyazaki S, Otsuka K. Acta. Metall 1985;33:2049.

[91]   Xu X, Thadhani NN. Scr Mat 2001;44:2477.

[92]   Saburi T, Yoshida M, Nenno S. Scr Matell 1984;50:363.

[93]   Liu Y, Xie ZL, Humbeeck JV, Delaney L. Acta Mater 1999;47:645.

[94]   Li S, Beyerlein IJ, Necker CT, Alexender DJ, Bourke M. Acta Mater 2004;52:4859.

[95]   Firstov GS, Van Humbeeck J, Koval YN. Scr Mat 2004;50:243.

[96]   Firstov GS, Koval YN, Van Humbeeck J, Portier R, Vermaut P, Ochin P. Mat Sci and Engr A 2006;438:816.

[97]   Oikawa K, Ota T, Gejima F, Ohmori T, Kainuma R, Ishida K, Mat Trans 2001;42:2472.

[98]   Kainuma R, Ise M, Jia CC, Ohtani H, Ishida K. Intermetallics 1996;4:151.

[99]   Xu Y, Otsuka K, Furubayashi E, Mitose K. Materials Letters 1998;34:14.

[100]   Cai W, Otsuka K. Scripta Materialia 1999;41:1311.

[101]   Fonda RW, Jones HN, Vandermeer RA, Scripta Mater 1998;39:1031.

[102]   Fonda RW, Jones HN. Mat Sci and Engr A 1999;273-275:275.

[103]   Wu SK, Wayman CM, Metallography 1987;20:1987.

[104]   Wu SK, Wayman CM, Scripta Metall 1987;21:83.

[105] Mulder JH, Maas JH, Beyer J. In: Wayman CM, Perkins J. editors. Proceedings of the International Conference on Martensitic Transformations, Monterey Institute for Advanced Studies Carmel CA 1993.

[106] Angst DR, Thoma PE, Kao MY. J De Phys 4 1995;5:747.

[107] Besseghini S, Villa E, Tuissi A. Mater Sci Eng A 1999;273-275:390.

[108] Meng XL, Cai W, Wang LM, Zheng YF, Zhao LC, Zhou LM. Scripta Mater 2001;45:1177.

[109] Han XD, Zou WH, Wang R, Zhang Z, Yang DZ, Wu KH, J De Physique IV 1995;5:753.

[110] Meng XL, Zheng YF, Wang Z, Zhao LC. Scripta Mater 2000;42:341.

[111] Thoma PE, Boehm JJ. Mater. Sci. Eng 1999;273-275:385.

[112] Xu Y, Shimizu K, Suzuki Y, Otsuka K, Ueki T, Mitose K. Acta Mater 1997;45:1503.

[113] Bastin GF, Rieck GD. Metall Trans 1974;5:1817.

[114] Cai W, Tanaka S, Otsuka K. Materials Science Forum 2000;327:279.

[115] Khachin VN, Matveeva NM, Sivokha VP, Chernov DB, Yu K. Doklady Akad Nauk SSSR 1981;257:167.

[116] Otsuka K, Oda K, Ueno Y, Piao M, Ueki T, Horikawa H. Scripta Metall Mater 1993;29:1355.

[117] Segal VM. Mat Sci and Engr A 1995;197:157.

[118] Langdon T. Mat Sci and Engr A 2007;462:3.

[119] Barber RE, Dudo T, Yasskin PB, Hartwig KT. Scripta Mater 2004;51:373.

[120] Hansen N, Huang X, Hughes DA. Mat Sci and Engr A;317:3.

[121] Furukawa M, Iwahashi Y, Horita Z, Nemoto M, Langdon T, Mat Sci and Engr A 1998;257:328.

[122] Niendorf T, Canadinc D, Maier HJ, Karaman I. International Journal of Fatique, 2007, Article in Press

[123] Nishida M, Itai I, Kitamura K, Chiba A, Yamauchi K. J De Phys IV 1995;5:635.

[124] Liu Y, McCormick PG. Acta Metall Mater 1994;42:2401.

[125] Karaman I, Yapici GG, Chumlyakov YI, Kireeva IV. Mat Sci and Engr A 2005;410-411:243.

[126] Krishnan M, Singh JB. Acta Mater 2000;48:1325.

[127] McCormick PG, Liu Y. Acta Metall Mater 1994;42:2407

[128] Karaca HE., Karaman I, Chumlyakov YI, Lagoudas DC, Zhang X. Scr Mater 2004;51:261.

[129] Li S, Yamauchi K, Nishida M. Scripta Mater 2003;49:723.

[130] Saburi T, Wayman CM. Acta Metall 1979;27:979

[131] Langdon T, Mat Sci and Engr A 2007;460-461:77.

[132] Meng XL, ZhengYF, Wang Z, Zhao LC. Mater Lett 2000;45:128.

[133] Cui J, Chu YS, Famodu OO, Furuya Y, Hattrick-Simpers J, James RD, Ludwig A, Thienhaus S, Wuttig M, Zhang Z, Takeuchi I, Nature 2006;5:286.

[134] Tian Q, Wu J. Mat Sci and Engr A 2002;325:249.

[135] Saburi T, Wayman CM, Acta Metall 1979;27:979.

[136] Skrobanek KD. Proc of SPIE 1996;2779:499.

[137] Proft JL, Duerig TW. In: Duerig TW, Melton KN, Stöckel D, Wayman CM. editors. Butterworth-Heinemann Ltd Boston MA 1990.

[138] Cunningham B, Ashbee KHG. Acta Metallurgica 1977;25:1315

VITA

Benat Kockar, daughter of Mehmet Emin Bilcen and Nihal Bilcen and younger sister of Baran Bilcen, was born in Ankara, Turkey. She graduated from Middle East Technical University, Department of Metallurgical and Materials Engineering, in May 1998. Following graduation, she continued her studies in the same university to pursue a graduate degree. She completed her research under the guidance of Prof. Dr. Sakir Bor and received Master of Science in Metallurgical and Materials Engineering Department in May of 2001. Benat enrolled in the Mechanical Engineering Department of Texas A&M University in Fall 2003. She continued her studies at Texas A&M University as a Doctor of Philosophy candidate in the same department. She held a teaching assistantship in Fall 2003 and research assistantship in Spring 2004. She has been sponsored by Hacettepe University in Turkey for her studies in Texas A&M University for 3 years. During her study, she was an author of two journal publications and more than five conference presentations. Upon graduation she will be an Assistant Professor in the Mechanical Engineering Department at Hacettepe University in Turkey. She is married to Dr. Mustafa K. Kockar and has a son named Barkan E. Kockar.

Her permanent address is:

Mebusevleri Mahallesi

Suslu Sokak, 22/11

Ankara, TURKEY

Email: benatbilcen@yahoo.com